GeoForschungsZentrum Potsdam
STIFTUNG DES ÖFFENTLICHEN RECHTS

Scientific Technical Report

ISSN 1610-0956

'Seismic and sub-seismic deformation on different scales in the NW German Basin'

Tina Lohr

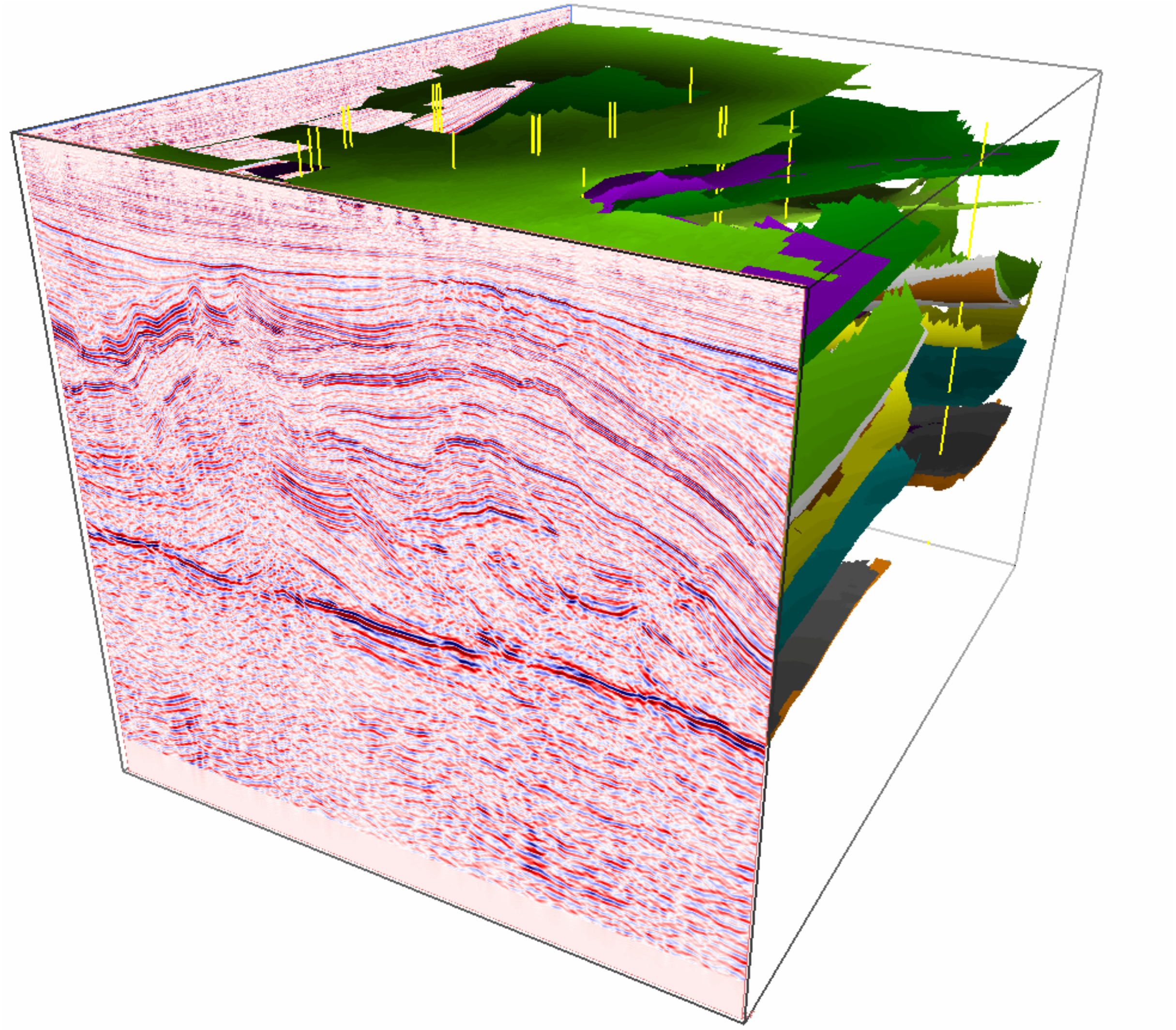

DOI: 10.2312/GFZ.b103-07087

Scientific Technical Report STR 07/08 GeoForschungsZentrum Potsdam

1. Gutachter: Prof. Dr. Onno Oncken
GeoForschungsZentrum Potsdam, Freie Universität Berlin

2. Gutachter: Prof. Dr. Charlotte M. Krawczyk
GGA-Institut Hannover, Technische Universität Berlin

Datum der Disputation: 31. Oktober 2007

DOI: 10.2312/GFZ.b103-07087

'Seismic and sub-seismic deformation on different scales in the NW German Basin'

Dissertation

zur Erlangung des akademischen Grades
doctor rerum naturalium (Dr. rer. nat.)
in der Wissenschaftsdisziplin Geologie

eingereicht im Fachbereich Geowissenschaften
der Freien Universität Berlin

von

Tina Lohr

Potsdam, Oktober 2007

DOI: 10.2312/GFZ.b103-07087

DOI: 10.2312/GFZ.b103-07087

Hiermit versichere ich, dass ich die vorliegende Arbeit ohne unzulässige Hilfe Dritter, und ohne Benutzung anderer als der angegebenen Literatur angefertigt habe. Die aus fremden Quellen direkt oder indirekt übernommenen Gedanken sind als solche kenntlich gemacht.

Potsdam, Oktober 2007

DOI: 10.2312/GFZ.b103-07087

DOI: 10.2312/GFZ.b103-07087

‘Zu wissen, was man weiß,
und zu wissen, was man nicht weiß,
das ist Wissen’

Konfuzius

DOI: 10.2312/GFZ.b103-07087

Contents

DOI: 10.2312/GFZ.b103-07087

DOI: 10.2312/GFZ.b103-07087

Chapters 2, 3, and 4 are already published or submitted in the following international scientific journals:

Chapter 2:

'Strain partitioning due to salt
- insights from interpretation of a 3D seismic data set in the NW German Basin'

T. Lohr, C.M. Krawczyk, D.C. Tanner, R. Samiee, H. Endres, H. Trappe,
O. Oncken, P.A. Kukla

Basin Research, 2007, v. 19 (4), p. 579-597

Chapter 3:

'Prediction of sub-seismic faults and fractures
- integration of 3D seismic data, 3D retro-deformation, and well data
on an example of deformation around an inverted fault'

T. Lohr, C.M. Krawczyk, D.C. Tanner, R. Samiee, H. Endres, O. Oncken, H. Trappe,
R. Bachmann, P.A. Kukla

AAPG Bulletin, accepted. Publishing expected in 2008.

Chapter 4:

'Evolution of a fault-surface from
3D attribute analysis and displacement measurements'

T. Lohr, C.M. Krawczyk, O. Oncken, D.C. Tanner

Journal of Structural Geology, under review.

DOI: 10.2312/GFZ.b103-07087

DOI: 10.2312/GFZ.b103-07087

Summary

The evolution of sedimentary basins is often strongly affected by deformation. Large-scale, subsurface deformation is typically identified by the interpretation of seismic data and evaluated by palinspastic reconstructions. However, sub-seismic small-scale deformation and the thereby generated fractures play an important role: they may accommodate a significant proportion of the total strain during basin evolution, lateral variation may cause compartmentalised deposits and reservoirs, and fracture networks may act as conduits for diagenetic fluids. These aspects depend primarily on the magnitude of deformation, the strain accumulation in space and time, and the processes that control both during basin evolution under varying kinematic constraints.

However, methodology limitations result in information gaps between large crustal-scale 2D seismic lines, high-resolution upper-crustal-scale 3D seismic data, and very small-scale 1D borehole data. To bridge these gaps in size and dimension between the different methods, and to correlate the deformation over large scale ranges, it is necessary to get the most out of the data with respect to the method's resolution, and to simulate the processes which are responsible for the next lower-scale deformation by appropriate modelling approaches.

For this purpose we analysed the orientation, distribution, and evolution of tectonic structures by using the following methods: analysis of 3D seismic data, analysis of well data, 3D kinematic modelling (retro-deformation), and analogue modelling.

A high-resolution 3D seismic data set with corresponding well data, located within the NW German Basin, was interpreted in detail. Large-scale deformation was analysed in terms of sedimentation, salt diaprism, as well as orientation, distribution, displacement, kinematic and timing of faulting. Processes like strain partitioning, as well as coupling/decoupling due to salt have been recognised, and several deformation phases from Carboniferous to Tertiary have been documented for the study area, and compared with the superimposed Central European Basin System.

On a smaller scale, 3D fault-surfaces have been studied. Displacement measurements and fault-attributes (dip, azimuth, curvature) helped not only to analyse the kinematics of these faults and the principal stress direction during Permian extension, but also to investigate fault-growth and linkage over time and over several scales down to the limits of seismic resolution.

A scale below, 3D kinematic retro-deformation of the fault's hanging wall volume helped to reveal information about orientation and density of sub-seismic strain during a special deformation period. Comparison of these medium-scale modelling results with large-scale seismic data and very small-scale well data allowed the quantification of sub-seismic strain, and to bridge the information gap between these scales, in the here investigated working area.

A final analysis integrating the timing of deformation over a broad scale range has been carried out with scaled physical sandbox models. A cohesive mixture of sand and gypsum was used for the observation of fault-growth processes, such as initiation and propagation of fractures, fault-segment-linkage, and the alternation of activity between different faults through time.

All here presented investigations from several scale ranges show a similar result: deformation is expressed as large heterogeneity in orientation, density, and timing of faults and fractures, and can have a similar pattern over a large scale range. However, this heterogeneity underlies different spatiotemporal causes dependent on processes relevant on the actual scale, and therefore complicates and questions a correlation.

DOI: 10.2312/GFZ.b103-07087

DOI: 10.2312/GFZ.b103-07087

Zusammenfassung

Die Entwicklung von Sedimentbecken ist oft sehr stark durch Deformation beeinflusst. Großskalige Deformation im Untergrund wird typischerweise mit Hilfe von seismischen Daten und palinspastischen Rekonstruktionen analysiert. Allerdings spielt kleinskalige, subseismische Deformation und die durch sie erzeugten Strukturen ebenso eine wichtige Rolle: sie können einerseits einen entscheidenden Teil der Gesamtverformung während der Beckenentwicklung akkumulieren, und andererseits tragen laterale Veränderungen zur Bildung von kleinen, abgeschlossenen Lagerstätten und Reservoiren bei. Ebenso können kleinskalige Bruchnetzwerke als Aufstiegsbahnen für Fluide genutzt werden. Dies alles ist in erster Linie abhängig von der Magnitude der Deformation, der Akkumulation von Verformung in Raum und Zeit, sowie den Prozessen, die beides während der Beckenentwicklung unter veränderlichen kinematischen Randbedingungen kontrollieren.

Methodische Grenzen führen jedoch zu Informationslücken zwischen z.B. großen krustenskaligen 2D seismischen Profilen, hochauflösenden oberkrustenskaligen 3D seismischen Datensätzen, sowie kleinskaligen 1D Bohrlochdaten. Um diese Skalen- und Dimensionslücken zu überbrücken, und die Deformation über verschiedene Skalenbereiche zu korrelieren, ist es notwendig, bis zur Auflösungsgrenze das Bestmögliche aus den vorhandenen Daten herauszuarbeiten, und anschließend die Prozesse zu simulieren, die im für die jeweiligen Methoden unzugänglichen Skalenbereich liegen.

Um dieser Aufgabe gerecht zu werden, analysierten wir die Orientierung, Verteilung und Entwicklung tektonischer Strukturen mit Hilfe folgender Methoden: Analyse eines 3D seismischen Datensatzes, Analyse von Bohrungsdaten, 3D kinematische Modellierung (Rückdeformation), sowie Analogmodellierung.

Wir interpretierten einen 3D seismischen Datensatz mit dazugehörigen Bohrungsdaten aus dem Nordwestdeutschen Becken. Großskalige Deformation wurde in Hinsicht auf Sedimentation, Salztektonik, sowie Orientierung, Verteilung, Versatz, Kinematik und Zeitlichkeit von Störungen untersucht. Dabei analysierten wir Prozesse wie Verformungspartitionierung und durch Salz bedingte Kopplung und Entkopplung von Krustenstockwerken. Wir konnten verschiedene Deformationsphasen vom Karbon bis ins Tertiär für das Arbeitsgebiet dokumentieren und mit dem übergeordneten Zentraleuropäischen Beckensystem vergleichen.

Eine Größenordnung darunter untersuchten wir Störungsflächen in 3D. Mittels Versatzanalyse und Störungsattributen (Einfallen, Streichen, Krümmung) konnten wir nicht nur die Kinematik dieser Störungen festlegen und die Spannungsrichtung während der Permischen Extension bestimmen, sondern auch Wachstum und Verlinkung von Störungen in Raum und Zeit bis hinunter zur Grenze der seismischen Auflösung analysieren.

Im darunterliegenden Skalenbereich untersuchten wir mit Hilfe 3D kinematischer Modellierung (Rückdeformation) den Hangendblock einer permischen Störung, um Informationen über Orientierung und Dichte subseismischer Verformung während eines Deformationsereignisses zu erhalten. Der Vergleich dieser mittelskaligen Modellierungsergebnisse mit den großskaligen seismischen Strukturen und den kleinskaligen Bohrungsdaten ermöglichte es uns, die subseismische Verformung zu quantifizieren und die Informationslücke zwischen den einzelnen Skalenbereichen im Untersuchungsgebiet zu schließen.

Um die Zeitlichkeit der Deformation über einen großen Skalenbereich umfassend zu betrachten, führten wir außerdem eine Untersuchung mit Hilfe von skalierten physikalischen

Sandboxmodellen durch. Wir verwendeten eine Mischung aus Sand und Gips, um Störungswachtumsprozesse wie z.B. Initiierung, Ausbreitung und Verlinkung von Störungen sowie die wechselseitige Aktivierung von Brüchen in der Zeit zu analysieren.

Zusammenfassend zeigen alle Untersuchungen aus den einzelnen Skalenbereichen ein gemeinsames Ergebnis: Deformation äußert sich in einer großen Heterogenität in Orientierung, Dichte und Zeitlichkeit von Störungen und Brüchen, und kann über einen großen Maßstab hinweg ähnliche Muster aufweisen. Allerdings unterliegen dieser Heterogenität unterschiedlichste zeitliche und räumliche Ursachen, abhängig vom jeweils betrachteten Skalenbereich, was demzufolge ihre tatsächliche Korrelation und damit Vorhersagbarkeit nicht nur erschwert, sondern auch in Frage stellt.

DOI: 10.2312/GFZ.b103-07087

1. Introduction

1.1. Overview

In this introductory chapter the objectives and motivation of the project are presented and the different working steps are described. It is not the purpose to introduce the general tectonic setting and the geology of the working area here, because this is already done in detail in the scientific publications that form parts of this thesis in the following way:

Chapter 2 ('Strain partitioning due to salt - insights from interpretation of a 3D seismic data set in the NW German Basin') deals with the general geology of the working area and its surrounding and overlying areas. It discusses the interaction and evolution of tectonic structures, sedimentary features, and salt diapirism in terms of strain and stress.

Chapter 3 ('Prediction of sub-seismic faults and fractures - integration of 3D seismic data, 3D retro-deformation, and well data on an example of deformation around an inverted fault') addresses the 3D kinematic modelling of structure analysed in detail within the studied data set. It demonstrates a combined analysis of different methods (3D seismic interpretation, coherency analysis, 3D kinematic modelling, well data analysis) over several scales, in order to correlate large-scale seismic data with small-scale well data (fractures), and to quantify and qualify sub-seismic strain.

Chapter 4 ('Evolution of a fault-surface from 3D attribute analysis and displacement measurements') concentrates on a detailed displacement and morphology analysis of one large normal fault in 3D, debating about the distribution and orientation of sub-seismic fractures, and assessing its seismic hazard.

Chapter 5 ('Analogue modelling of fault-growth processes') emphasises especially the temporal variations of strain distribution over several scales and documents fault-growth processes such as fault-propagation and segment linkage, as well as alternation of fault activity.

Chapter 6 ('Paleostress analysis from 3D seismic data – an outlook') focuses on the calculation of paleostress data on the basis of detailed 3D interpretations of Permian normal faults.

The results of these chapters are summarised and comprehensively discussed in chapter 7.

1.2. Objectives and motivation

This project is integrated in the DFG-Schwerpunktprogramm 1135 'Dynamics of sedimentary systems under varying stress regimes: The example of the Central European Basin'.

The main objective of this study is the quantification and qualification of strain over a broad scale range, including its distribution, magnitude, and accumulation history during basin evolution. These objectives are important contributions to the questions of stress transfer and deformation processes in the Southern Permian Basin.

Sedimentary basins record a variety of spatial and temporal processes, and exhibit a complex pattern of structural and deformational features and styles. There is a lack of a deeper

DOI: 10.2312/GFZ.b103-07087

understanding of how structures and the responsible deformation processes relate to each other across the range of scales from lithospheric faults to grain-scale fractures.

Within the Southern Permian Basin, one of the major problems of unravelling the post-Variscan deformational history is the localised nature of deformation, where initially small isolated grabens were gradually filled by predominantly locally-derived sediments. During the Mesozoic and Cenozoic, crustal subsidence of the intracontinental Southern Permian Basin developed, and a general depositional pattern was established (Fig. 1.1), allowing a correlation between the former sub-basins. Different geological, geophysical or integrated large-scale models are available now covering large parts of the whole Central European Basin System (e.g. Ziegler, 1990; Thybo, 1997; Scheck & Bayer, 1999; Yegorova & Starostenko, 1999; Scheck-Wenderoth & Lamarche, 2005 and references therein; McCann et al., 2006; Krawczyk et al., 2007).

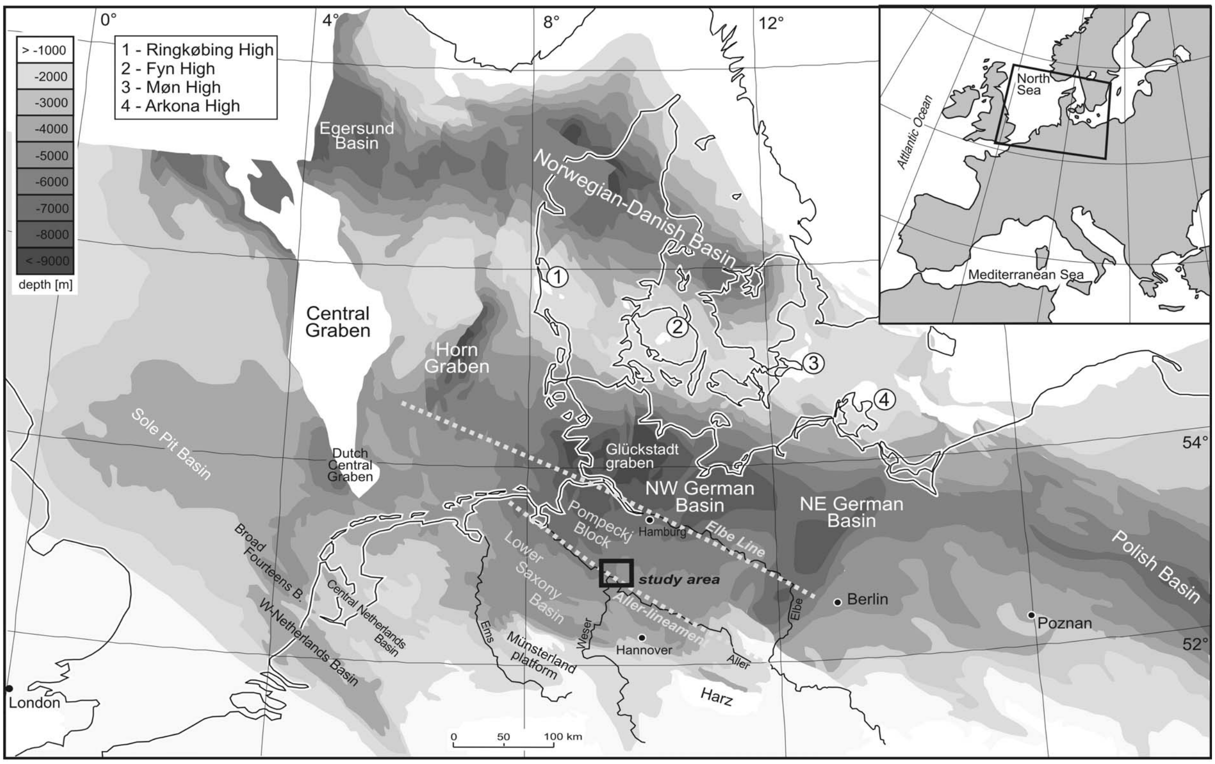

Figure 1.1: Depth map of the Southern Permian Basin and location of the study area. Modified after Kossow (2001) and the NW European Gas Atlas (Lockhorst 1998).

An order of magnitude lower, depth-sections are used as input for the setup of basin-wide structural models, but the correlation of different depth-sections is often inconsistent because of non-unified basic data. In sedimentary basins the restoration of such seismic depth-sections are used to reveal the sub-surface structures, the nature of basin-forming mechanisms, and the kinematic evolution of the area under consideration, but also to understand facies and source-reservoir relationships. In the North German Basin, the only available palinspastic reconstructions are in the NE (Kossow & Krawczyk, 2002), and forward modelling of the initial phase of basin formation was applied in combination with detailed analysis of core material (Rieke et al., 2001).

Conventional restorations typically yield minimum deformation values. However, valid results for restoration and retro-deformation based on seismic data require the consideration of sub-seismic-scale deformation, which has an important impact on basin evolution (e.g. Pickering et al., 1996; Tanner et al., subm.). Whereas the interpretation of reflection seismic data allows especially the analysis of brittle large-scale deformation, structures below the seismic resolution (hereafter referred to sub-seismic) and ductile strain components may also accommodate a significant amount of the total strain (Marrett & Allmendinger, 1991; Scholz & Cowie, 1990), reaching up to 40-50 % on both local and regional scale (Walsh et al., 1996; 1998 and references therein; Tanner et al., subm.).

The understanding of the structural inventory of the North German Basin as observed today, and especially quantitative modelling of the deformation processes and their time-dependent interactions occurring in this dynamic setting, however, require an integrated approach over a large range of scales to understand the complexity mentioned above, and to provide appropriate predictions in terms of e.g. strain distribution, fault connectivity, and fluid migration. Quantitative seismic interpretation, calibration with well data, 3D retro-deformation, and analogue modelling provide information on the strain geometry over a broad range of scales, between the mm (borehole) and 10 m (seismic) scale, and on the processes of its accumulation through geologic time.

The data set here analysed in the North German Basin (for location see Fig. 1.2) is one of the rare cases where geophysical data are available together with well data within one volume from the Quaternary down to the Carboniferous. RWE Dea AG (Hamburg) provided a high-resolution 3D reflection seismic data set together with well data, containing 14 wells with deviation data, log data, partly FMI (Formation Micro Image) and core data. For confidentiality reasons the location is not defined in more detail.

Figure 1.2: Topography of Germany and adjacent countries with location of the study area. Alpine deformation did not affect the surface topography near the study area, but it is recognised in the subsurface. Data source: http://commons.wikimedia.org/wiki/Image:Deutschland_topo.png (modified).

1.3. Working procedure

1.3.1. 3D reflection seismic interpretation

The analysed 3D reflection seismic data set was provided as a pre-stack depth migrated (PSDM) volume by RWE Dea AG, Hamburg. The volume covers an area of 22 x 17 km and reaches down to a depth of ca. 7.5 km. The grid spacing is 25 m by 25 m, and approx. 30 m vertical resolution is reached, depending on the depth in the volume.

The first working step was loading of the seismic volume into the seismic interpretation software GeoFrame/IESX (Schlumberger). Subsequently, well data were loaded together with their log information (LAS files), and corresponding deviation files needed to be integrated in order to position the bore-hole data correctly. To calibrate the well data with the seismic volume, stratigraphic markers from composite logs were imported into GeoFrame and checked for consistency throughout the volume.

After loading, numerous horizontal slices have been created from the seismic volume, which allowed a better correlation of faults and horizons not only along vertical sections (inlines, crosslines, diagonal lines, zig-zag lines), but also in map view during the subsequent interpretation process (Fig. 1.3).

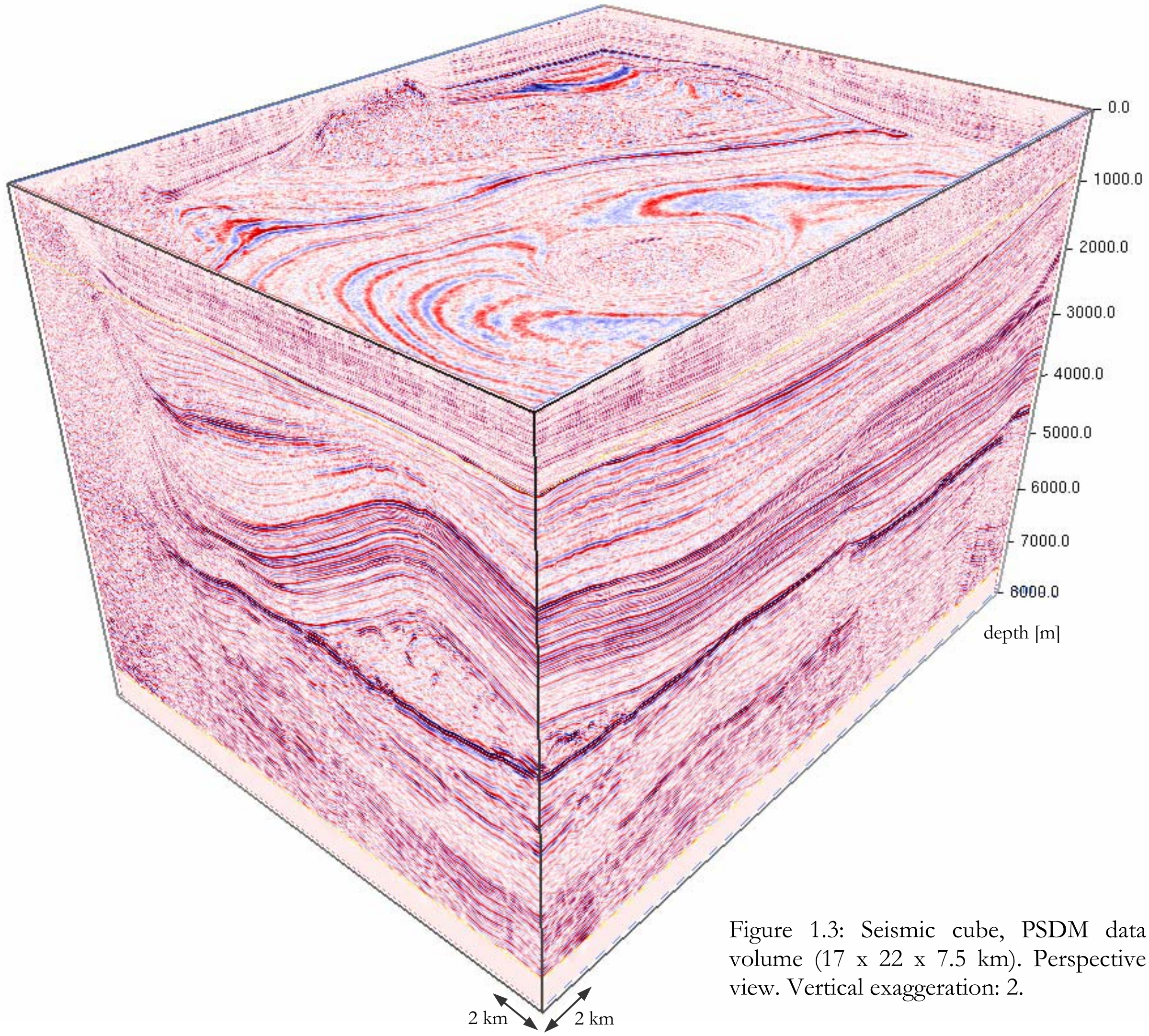

Figure 1.3: Seismic cube, PSDM data volume (17 x 22 x 7.5 km). Perspective view. Vertical exaggeration: 2.

DOI: 10.2312/GFZ.b103-07087

The next step was the interpretation of important stratigraphic horizons and good correlative seismic reflectors (Fig. 1.4) by tracing and picking of a reflector phase-consistently along its peak amplitude (Fig. 1.5). First, horizon interpretation was carried out using a coarse grid with a line spacing of 125 m (picking every fifth inline and crossline). Depending on strong faulting and quality (low-amplitude signal) of the analysed reflector, in some cases the mesh needed to be tighter by choosing a line spacing of 75 m (every third inline and crossline). After this manual interpretation (75 to 125 m grid) the non-interpreted inlines and crosslines were interpreted automatically (autotracking) resulting in a 25 m grid. Subsequently, after autotracking, the horizons were checked for accuracy, and improved manually if required. The key reflectors that have been interpreted are: Top Reflective Carboniferous, Base Rotliegend, Top A2, Top Zechstein salt, Base Jurassic, Jurassic/Cretaceous unconformity, Base Upper Cretaceous, and Base Tertiary.

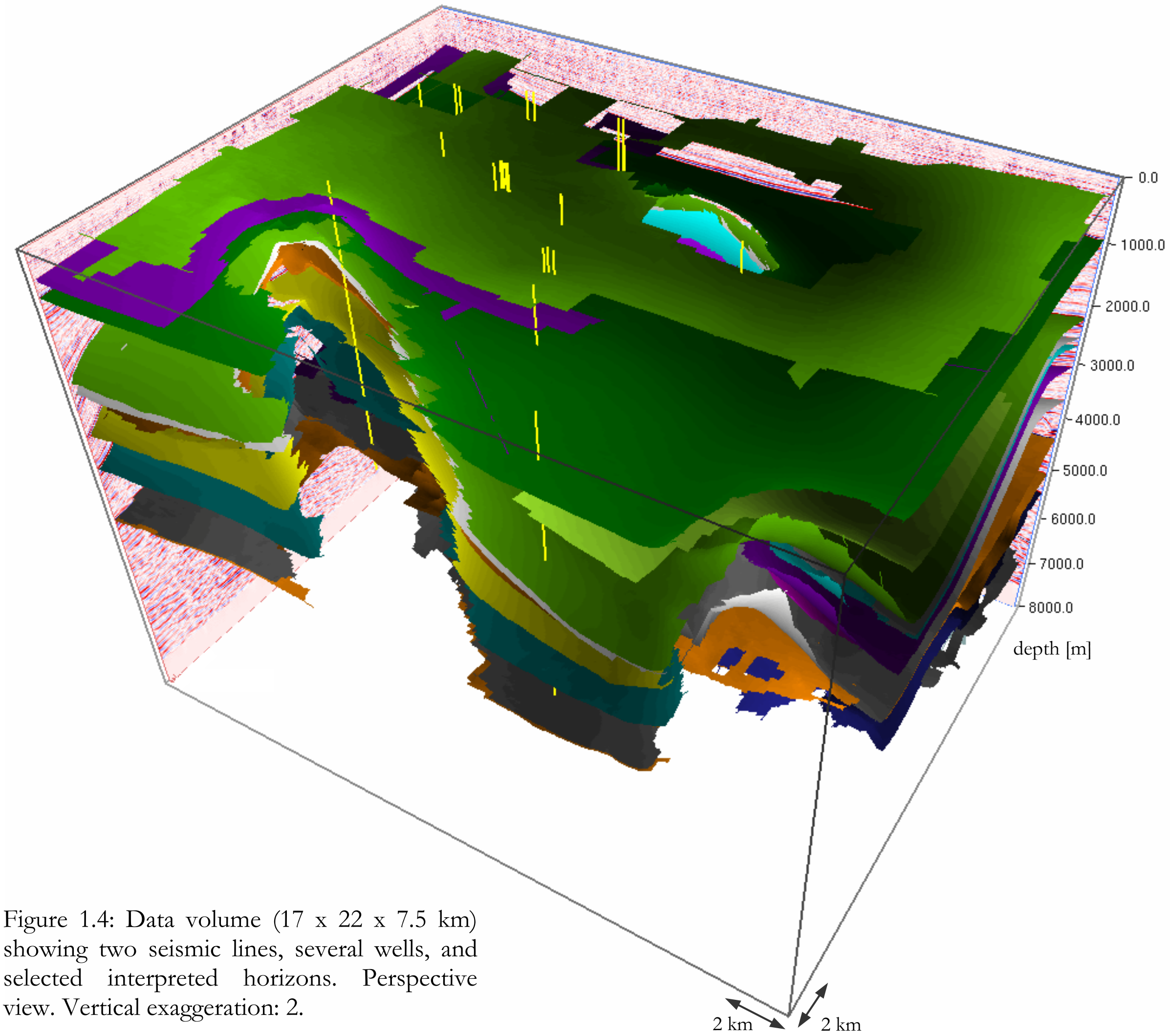

Figure 1.4: Data volume (17 x 22 x 7.5 km) showing two seismic lines, several wells, and selected interpreted horizons. Perspective view. Vertical exaggeration: 2.

After compilation of complete horizons, numerous dip-, azimuth- (Fig. 1.6), and thickness maps (Fig. 1.7), as well as horizon slices (Fig. 1.8) were created. A thickness map can be done by subtracting the depth of a horizon from that of a deeper horizon. Variations in thickness refer then to tectonic or sedimentary changes during sedimentation. Dip and azimuth maps highlight subtle changes in the dip of a horizon, direction variations, and folded or fractured areas. Horizon slices (= amplitude maps) can be created by flattening the seismic volume at an interpreted horizon. In map view, slight changes in amplitude of this horizon are highlighted, and subtle lineaments (faults or sedimentological features) can thus be identified (Figs. 1.6, 1.8).

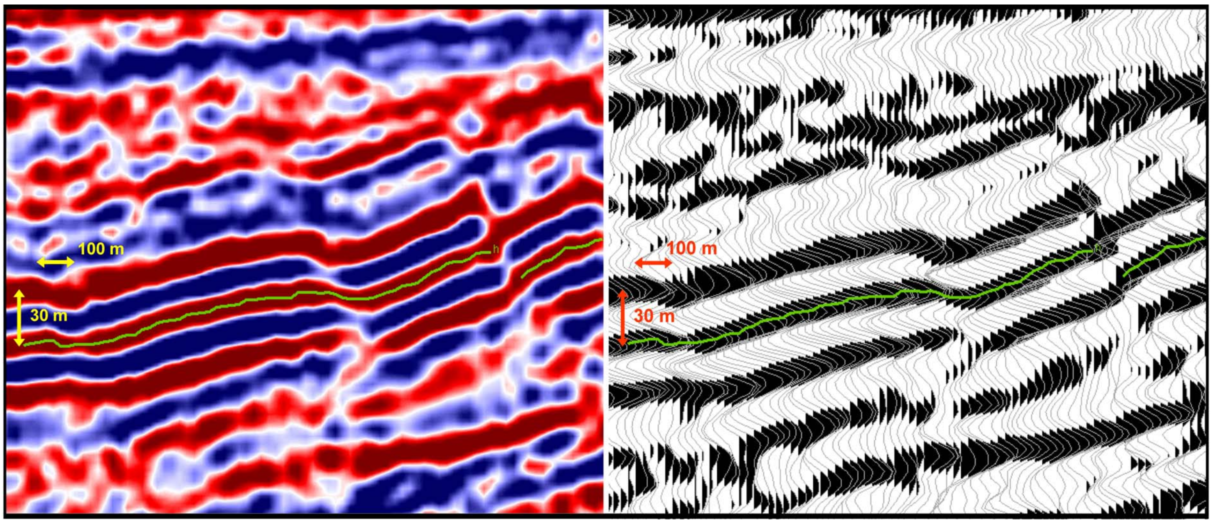

Figure 1.5: Detailed example of the seismic data in 2 km depth. Left: colour-coded seismic amplitudes demonstrating the high resolution and one interpreted reflector (green line). Right: same image but without colour-coded amplitudes. Here, all traces are visible and positive amplitudes are filled with black. See scales for resolution.

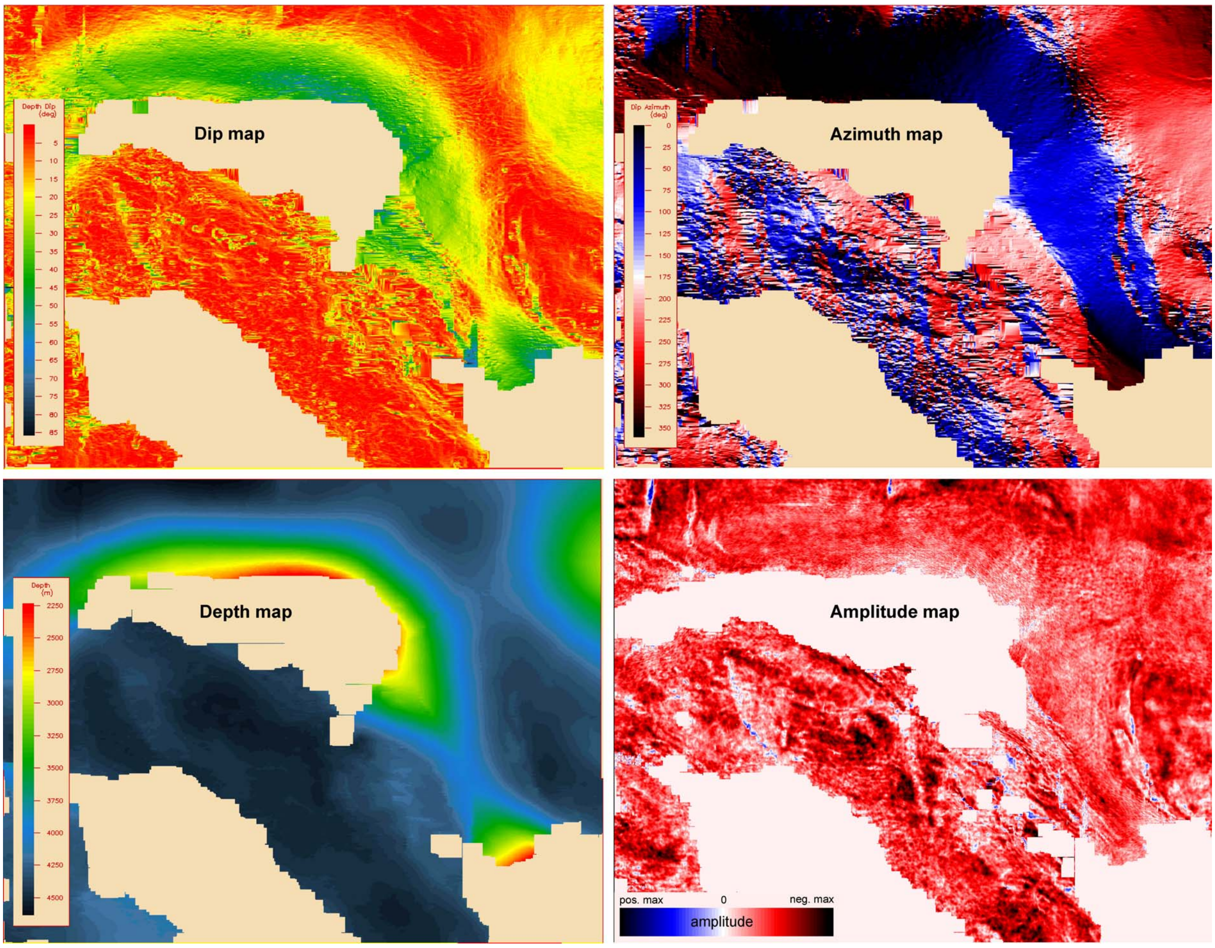

Figure 1.6: Several attribute maps of Top Zechstein salt horizon showing the detailed structured surface. Blank colours are uninterpreted areas, because here salt rose into diapirs, and the amplitudes of the reflector are too low for being suitable for interpretation. The dip map indicates the amount of dip, the azimuth map illustrates the direction to which the reflector is dipping, and the depth map shows the depth range where the horizon is located today. The amplitude map (horizon slice) shows the intensity of reflections, and can highlight tectonic features along which usually the amplitude decreases. Area size: 17 x 22 km.

DOI: 10.2312/GFZ.b103-07087

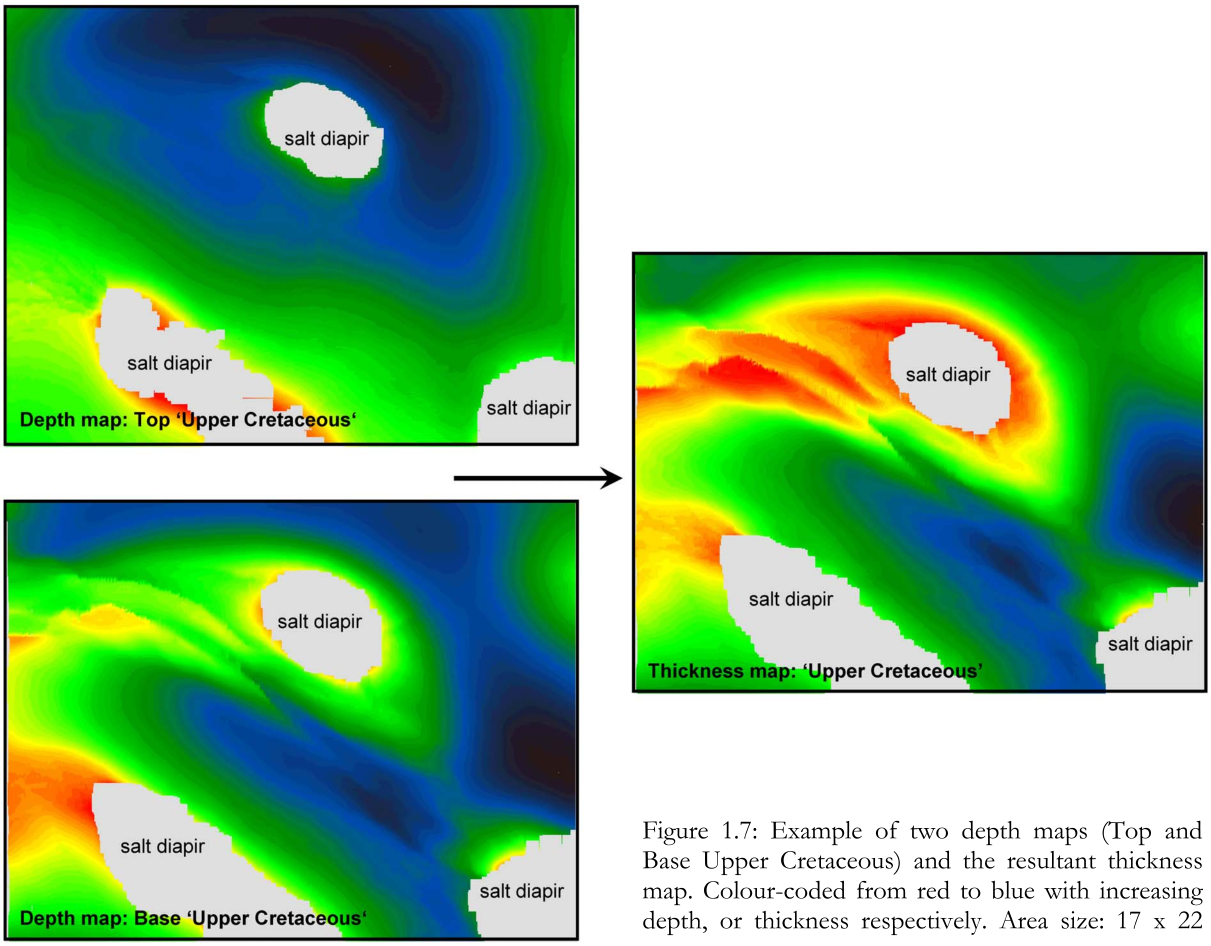

Figure 1.7: Example of two depth maps (Top and Base Upper Cretaceous) and the resultant thickness map. Colour-coded from red to blue with increasing depth, or thickness respectively. Area size: 17 x 22

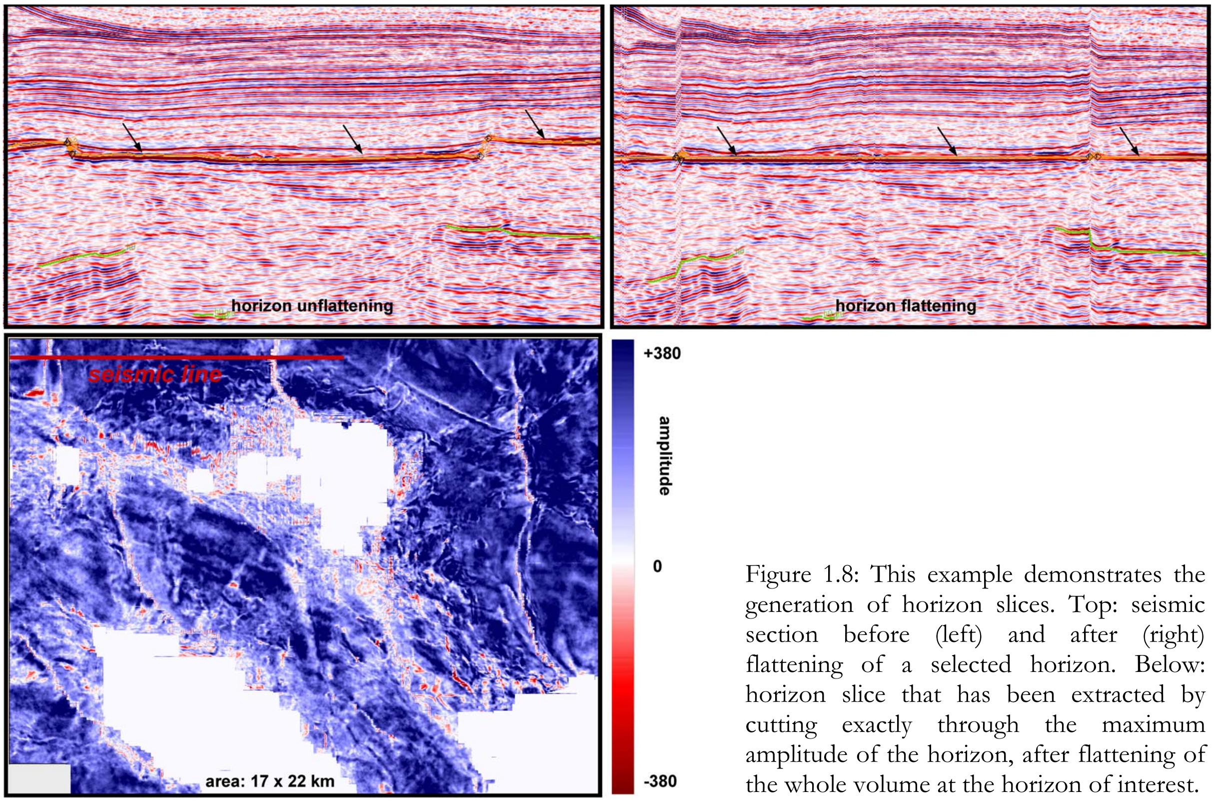

Figure 1.8: This example demonstrates the generation of horizon slices. Top: seismic section before (left) and after (right) flattening of a selected horizon. Below: horizon slice that has been extracted by cutting exactly through the maximum amplitude of the horizon, after flattening of the whole volume at the horizon of interest.

DOI: 10.2312/GFZ.b103-07087

Faults have been interpreted first in map view, using a combination of depth maps, thickness maps, dip maps, and horizon slices, to obtain an overview about the general structural style in the working area. Later, faults have been interpreted along appropriate cross-sections in detail. For modelling purposes, the major Permian faults were interpreted in 3D as detailed as possible.

3D seismic interpretation is the base for the subsequent tectonic modelling. During interpretation of the data set numerous evaluations were necessary in order to interpret the evolutionary model correctly, e.g. seismic reflections were analysed whether they represented relevant geological features or seismic artefacts, tectonic structures needed to be identified and distinguished from sedimentological features, regional unconformities needed to be evaluated in space and distinguished from local unconformities caused by salt diapirism, and the interaction of faulting and deformation overprint had to be defined for later kinematic restorations (see chapter 2).

1.3.2. Tectonic modelling

After seismic volume interpretation, surfaces have been loaded into the modelling software GoCad (GoCad Consortium) and 3Dmove (Midland Valley). GoCad was used especially for surface triangulation of horizons and faults, cutting or merging of objects, surface attribute calculations (dip, azimuth, curvature), and finally construction of tectonic models. In GoCad, the surfaces were analysed and cross-checked with the seismic data for consistency, and, if necessary, reinterpreted. Depending on the purpose and the modelling procedure, several smaller models have been created, rather than one large model of the whole study area (Fig. 1.9).

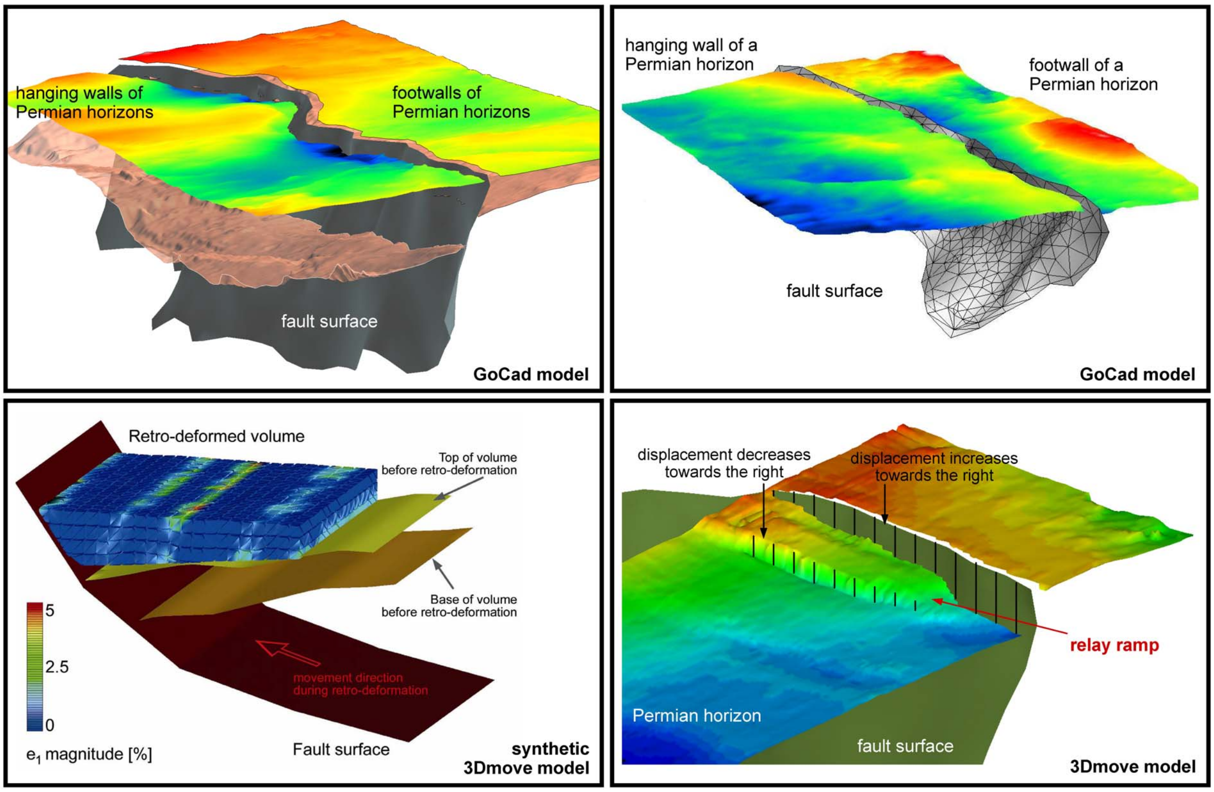

Figure 1.9: Several selected models constructed with GoCad and 3Dmove software. Horizons are colour-coded from red to blue with increasing depth. No vertical exaggeration.

After constructing the tectonic models in GoCad, several objects (surfaces, lines) were loaded into the software 3Dmove, which was then used for orientation measurements (pole-point plots of surface triangles), fault morphology analyses (definition of the kinematic vector), 3D displacement calculations (Allen maps), volume generation between surfaces, 3D restorations (retro-deformation) of natural and synthetic models, as well as strain analyses. Excel and SpheriStat software were used for the subsequent evaluation of results from kinematic, displacement, and strain analyses.

With the constructed it was possible to quantitatively assess geometrical quantities such as fault displacement, kinematic vectors and sequences, and the pattern and magnitude of deformation from seismic-scale structures. The relations between horizons and fault surfaces reveal the relative ages of single kinematic increments. 3D retro-deformation of the constructed model validated its geometric and kinematic characteristics. Furthermore, the validated model allowed the prediction of distribution and magnitude of strain within the retro-deformed volume. Model validation encompasses an incremental retro-deformation of the different deformation stages during basin evolution (see chapters 3 and 4).

1.3.3. Analogue modelling

In addition to the prediction of distribution and orientation of strain from 3D retro-deformation, scaled analogue experiments were performed, designed on the basis of the results from seismic interpretation and model building. The analogue modelling was based on a parameter analysis and mechanical properties related to the structural types comparable to the North German Basin. This analysis allowed a better understanding of distribution, accumulation, and scaling of deformation during crustal extension, and provides constraints on the temporal evolution and structural processes responsible for the patterns identified in the 3D seismic data and 3D retro-deformation models.

During analogue modelling (chapter 5), the evolution of normal faulting was studied in terms of distribution and accumulation of strain, which refers to the observation of fault-linkage, small-scale strain, and the time-dependent activation and deactivation of faults. These experiments were detected and analysed with an optical high-resolution digital camera and were subsequently processed with the PIV technology (Particle Image Velocimetry) of LAVISION software DaVis, which allows to quantify the deformation at all scales and to measure all components of the displacement-gradient tensor (chapter 5).

Before starting the appropriate experiments and constructing the suitable deformation box (see experiment study in chapter 5), parameter experiments have been carried out to test different materials (sand, cement, starch, gypsum, and mixtures among them) and their physical behaviour under extensional conditions (Fig. 1.10). We recognised that pure sand was not suitable for our purpose because its cohesion is very low and it develops no tensile fractures. However, pure starch, cement, and gypsum are characterised by a high cohesion and tensile fractures, but shear fractures developed only secondarily. By testing different material mixtures, we found that a mixture of sand and gypsum in relation 3:1 was the most suitable analogue material, as it showed steep structures, open fractures, and shear fractures. These structures represent well the upper brittle crust, and are therefore suitable for comparing the structures of our working area. Additionally, the sand-gypsum mixture has a small grain size which is necessary for a detailed observation of fault-growth processes also at a small scale.

DOI: 10.2312/GFZ.b103-07087

starch-sand: 1:2 **cement-sand: 4:1** **cement-sand: 1:1**

gypsum-sand: 1:1 **gypsum-sand: 1:2** **gypsum-sand: 1:3**

Figure 1.10: Selected preliminary extensional experiments testing different materials and showing a different faulting behaviour. All experiments have been done under the same boundary conditions. Horizontal measure is in cm; vertical extent of entire box is 12.5 cm.

DOI: 10.2312/GFZ.b103-07087

2. Strain partitioning due to salt – insights from interpretation of a 3D seismic data set in the NW German Basin

Abstract

We present results from interpretation of a 3D seismic data set, located within the NW German sedimentary basin, as part of the Southern Permian Basin. We focused on the development of faults, the timing of deformation, the amount of displacement during multiphase deformation, strain partitioning, and the interaction between salt movements and faulting. We recognised the central fault zone of the study area to be the Aller-lineament, an important NW-trending fault zone within the superimposed Central European Basin System.

From structural and sedimentological interpretations we derived the following evolution: (1) E-W extension during Permian rifting, (2) N-S extension within cover sediments, and E-W transtension affecting both basement and cover, contemporaneously during Late Triassic and Jurassic, (3) regional subsidence of the Lower Saxony Basin during Late Jurassic/Early Cretaceous, (4) N-S compression within cover sediments, and E-W transpression affecting both basement and cover, contemporaneously during Late Cretaceous/Early Tertiary inversion, (5) major subsidence and salt diapir rise during the Cenozoic.

We suggest that the heterogeneity in distribution and timing of deformation in the working area was controlled by pre-existing faults and variations in salt thickness, which led to stress perturbations and therefore local strain partitioning. We observed coupling and decoupling between pre- and post-Zechstein salt units: in decoupled areas deformation occurred only within post-salt units, whereas in coupled areas deformation occurred in both post-salt and pre-salt units, and is characterised by strike-slip faulting.

2.1. Introduction

Numerous seismic surveys carried out by the oil and gas industry provided insight into the complex structural style and sedimentary record of sedimentary basins, like the NW German Basin. Primarily, 2D reflection seismic lines and well data were used for interpretations of important subsurface structures and basin-wide deformational processes (e.g. Baldschuhn *et al.,* 1996; Brink *et al.,* 1992; von Hartmann, 2003; Kossow & Krawczyk, 2002; Maystrenko *et al.,* 2005). Rare 3D reflection seismic measurements were carried out on a much smaller scale (von Hartmann, 2003; Mohr *et al.,* 2005). 2D seismic cross-sections are subject to spatial artefacts: the reflection patterns are affected by marginal effects, the profiles do not necessarily run perpendicular to the strike direction of the structural elements, and section balancing and calculation of material loss is arguable when mobile salt structures are involved. Therefore, 3D seismics are important to clarify still unsolved aspects in the evolution of the NW German Basin: e.g. the relationship among fault systems, the relationship between faulting and sedimentation, the kinematic regime during several deformational phases, the development and timing of inversion structures, as well as the coupling or decoupling between pre- and post-salt units, and the role of salt diapirism and the interaction between faulting and salt movements.

Many of these aspects are also essential for other sedimentary basins. The NW German Basin with its complex development is a good study area in which to gain insight into these aspects. Therefore, we have investigated the structural and sedimentological aspects of the study area with

DOI: 10.2312/GFZ.b103-07087

a 3D seismic data set, to investigate the underlying processes behind the structures observed, and to compare them with the evolution of other neighbouring basins. The location of our working area within a key zone (Aller-lineament) of the Southern Permian Basin makes this study important to gain insights into the complex deformation history of this basin, and to understand more about the interaction between faulting and salt movements within sedimentary basins in general.

2.2. Tectonic setting

The NW German Basin is part of the European Southern Permian Basin (SPB), a specious epicontinental/intracontinental sedimentary basin developed on Variscan and Caledonian deformed crust. The NW-SE orientated SPB extends from the North Sea to Poland and varies in width between 300 and 600 km between Scandinavia and the Variscan Deformation Front (Fig. 2.1). It initiated in the Late Carboniferous to Permian, but subsequent multiphase deformation and salt migration over several hundred Ma affected not only the thick sedimentary cover, but also the older basement rocks, and divided the large basin in several sub-basins: Sole Pit Basin, Broad Fourteens Basin, Central Netherlands Basin, West Netherlands Basin, Central Graben, Horn Graben, NE German Basin, Polish Basin, as well as the Lower Saxony Basin, Pompeckj Block and Glückstadt Graben as part of the NW German Basin.

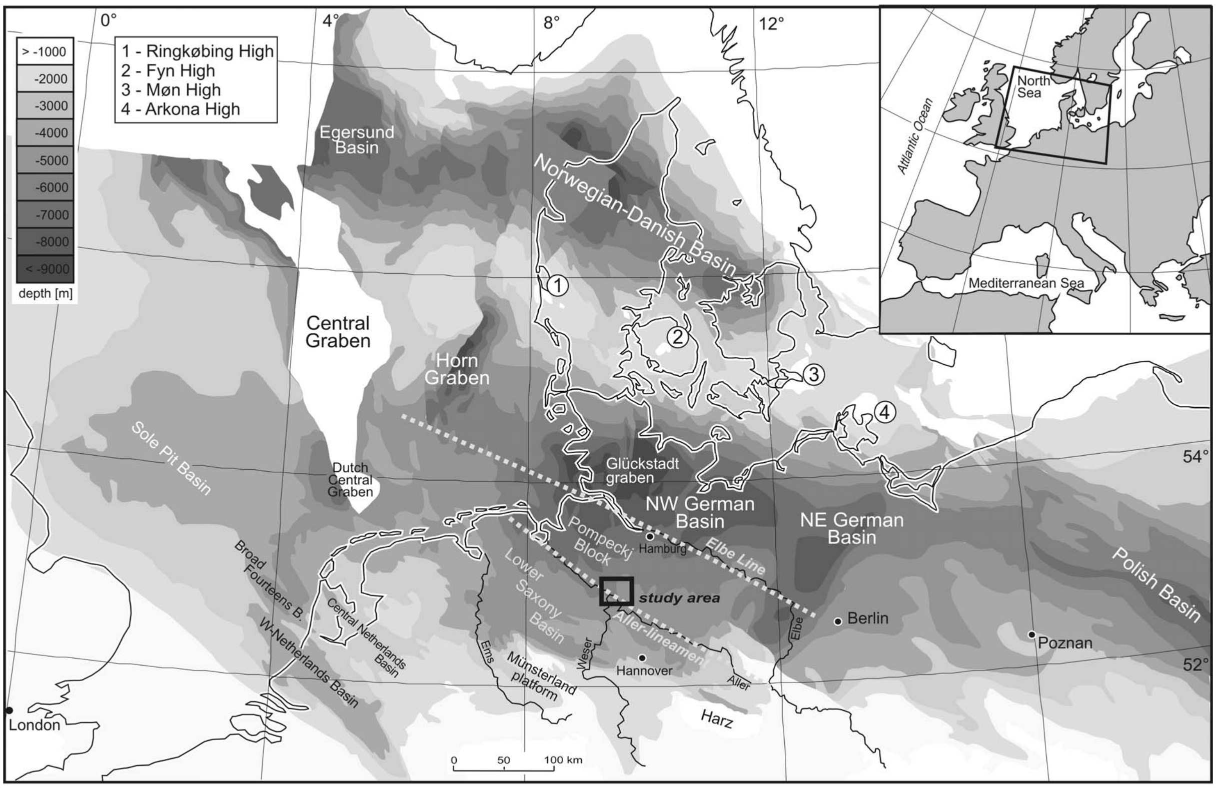

Figure 2.1: Depth map of the Southern Permian Basin and location of the study area. The NW-striking Aller-lineament forms the border between the Lower Saxony Basin in the south and the Pompeckj Block in the north, which represent two sub-areas of the larger NW German Basin. Modified after Kossow (2001) and the NW European Gas Atlas (Lockhorst 1998).

The general evolution of the Southern Permian Basin and its sub-basins is documented by e.g. Betz *et al.,* 1987; Glennie, 1998; Meissner & Bortfeld, 1990; Ziegler, 1990; Blundell *et al.,* 1992 and

DOI: 10.2312/GFZ.b103-07087

references therein; Brink *et al.,* 1992; Pharaoh, 1999 and references therein; Krawczyk *et al.,* 1999 and 2002; Scheck-Wenderoth & Lamarche, 2005 and references therein.

In Central Europe, rifting and associated volcanism in the post-Variscan phase occurred in a dextral transtensional stress regime (e.g. Arthaud & Matte, 1977; Betz *et al.,* 1987; Ziegler, 1990) and produced mainly N-S orientated normal faults and NW-trending dextral strike-slip faults during the Late Carboniferous and Permian (e.g. Kockel, 2002; Gast, 1991 and 1988; Ziegler, 1990; Betz *et al.,* 1987). After the Middle Triassic, regional E-W extension opened NNE-SSW-trending grabens (e.g. Glückstadt Graben, Rheinsberg, Gifhorn, Hamburg and Jade-Westholstein Troughs (Scheck & Bayer, 1999; Maystrenko *et al.,* 2005)). Graben systems like the Permian Lower Saxony rift system (Gast, 1988 and 1991; Ziegler, 1990) and associated basins extend northwards via the Glückstadt Graben, the Horn Graben, and the Skagerrak Graben into the Oslo Graben (Gast, 1988 and 1991; Ziegler, 1990). Subsequently, the Southern Permian Basin thermally subsided coevally with deposition of Rotliegend clastics, followed by deposition of several kilometres of sediments from the Zechstein until the Quaternary (e.g. Baldschuhn *et al.,* 1996). During the Mesozoic and Cenozoic the area was affected by different processes such as salt movement, regional and differential subsidence, Triassic/Jurassic extension, as well as Late Cretaceous/Tertiary compressional phases and thereby associated basin-wide inversion processes (e.g. Schwab *et al.,* 1982; Betz *et al.,* 1987; Baldschuhn *et al.,* 1991; Brink *et al.,* 1992; Kossow *et al.,* 2000; Kockel, 2003; de Jager, 2003; Scheck-Wenderoth & Lamarche, 2005).

Within the NW German Basin, sub-areas developed during the Mesozoic. Our working area is located at the transition of two of them: the Lower Saxony Basin (LSB) located in the south, and the Pompeckj Block (PB) located in the north (Fig. 2.1). Only a few studies have been carried out investigating the evolution of these sub-areas more closely, especially the LSB, mainly based on 2D seismic interpretations (Baldschuhn *et al.,* 1985; Betz *et al.,* 1987; Brink *et al.,* 1992; Best, 1996; Mazur & Scheck-Wenderoth, 2005) and 1D well data (Gast, 1988; Hoffmann *et al.,* 2005), but only rarely on 3D seismic data (von Hartmann, 2003; Tanner *et al.,* subm.). The deformation within the LSB and the PB is very heterogeneous, and 1D or 2D investigations very often cannot resolve complex 3D structures. Especially the orientation of structures, and the timing of extension and inversion differ spatially, and the processes behind are not clearly understood. There are no significant vertical offsets within the basement of the LSB, the crustal configuration is largely unknown, and the role of salt and basement involvement is not completely answered.

The transition zone between the two sub-areas (LSB and PB) is the so-called Aller-lineament, a prominent NW-striking feature (Fig. 2.1). The lineament is a zone separating areas (LSB, PB) of different sedimentation (Best, 1996; Betz *et al.*, 1987; Hoffmann *et al.,* 2001; Kockel, 2003; Frisch & Kockel, 2003; Scheck-Wenderoth & Lamarche, 2005), characterised by a high occurrence of Zechstein salt structures (Baldschuhn *et al.,* 1996), and both vertical and horizontal movements (Stackebrandt & Franzke, 1989; Betz *et al.*, 1987). It has been described as a deep-seated Palaeozoic fault zone, which underwent polyphase reactivation during the Mesozoic and partly Cenozoic (e.g. Gast, 1988; Hoffmann *et al.,* 1998; Frisch & Kockel, 2003). Despite several investigations, the deformation style and the precise localisation of the Aller-lineament, as well as the correlation between basement structures and Mesozoic structures is not well determined.

Although Permian rifting (expressed by N-S oriented grabens) continued during the Triassic north of the Aller-lineament, the area south of the Aller-lineament experienced nearly no deformation during that time. The separation between the LSB and the PB started in the Late Jurassic, when the PB became uplifted and the regional Jurassic/Cretaceous unconformity developed. Contemporaneously, the LSB suffered differential subsidence due to divergent dextral movements along NW-SE trending fault systems, during which reactivation of Permo-

DOI: 10.2312/GFZ.b103-07087

Carboniferous fault systems occurred (e.g. Aller-lineament) (Betz *et al.,* 1987). Inversion took place during the Late Cretaceous and was expressed predominantly as transpressive movement; but it was not synchronous in all parts of the LSB (Betz *et al.,* 1987). Especially the fault systems along the northern and southern margin of the LSB became reactivated, and the sedimentary fill was thrusted over the adjacent stable PB in the north and the Münsterland platform in the south (Betz *et al.,* 1987).

Caused by this evolution, today, in the LSB NW-striking faults dominate, whereas the PB is marked by mainly N- to NNW-striking faults. Together with the Elbe line, the Aller-lineament belongs to the NW-trending Elbe Fault System, along which a change in orientation of salt structures is observable (e.g. Jaritz, 1987; Lokhorst, 1998; Scheck *et al.,* 2003; Scheck-Wenderoth & Lamarche, 2005). North of the Elbe Fault System salt structures strike N-S, parallel to Triassic/Jurassic initiated grabens like the Glückstadt Graben, the Horn Graben, and the Central Graben (e.g. Ziegler, 1990; Lokhorst, 1998; Kockel, 2002). South of the zone salt structures strike mainly NW-SE, parallel to Jurassic/Early Cretaceous basins like the Sole Pit, the Broad Fourteens, and the LSB (e.g. Betz *et al.*, 1987; Ziegler, 1990; Lockhorst, 1998).

2.3. Data base

A pre-stack, depth-migrated, 3D reflection seismic data set and well data were provided by RWE-Dea AG, Hamburg, for this study. For interpretation, the seismic volume (17 x 22 km x 7.5 km depth) was loaded together with drill-hole information allowing a seismostratigraphic calibration (software: GeoFrame, Schlumberger). The 11 wells are located in the central part of the investigated area. The seismic data volume was interpreted, and reflections as well as picked horizons were checked for consistency. Fault surface geometries were also determined in 3D.

The seismic volume images the structures of the study area from the Carboniferous to the Quaternary. Generally, exploration drilling aims to reach the Upper Rotliegend, because it is the most exploited hydrocarbon-reservoir in the NW German Basin. Only rarely do wells penetrate Lower Rotliegend or Carboniferous rocks, and therefore these strata cannot continuously correlated across the whole area. In places, salt impaired the seismic interpretation by reducing the reflection energy underneath large salt domes, and by deforming overlying sediment reflections due to velocity pull-up. However, the overall data quality is good and enables detailed structural insights.

2.4. 3D structures

2.4.1. General stratigraphy

From correlation of well data the stratigraphy with its average thickness is summarised in Figure 2.2. Selected depth and thickness maps are shown in Figure 2.3, including the location of three seismic cross-sections (shown in Figs. 2.4, 2.5, 2.6), and the locations of wells (Fig. 2.3 c). Numerous unconformities have been recognised: within the Rotliegend, Base Zechstein, within the Buntsandstein, within the Lower and Upper Cretaceous, Base Tertiary, as well as several unconformities within the Quaternary. The major unconformities are marked in the stratigraphic overview (Fig. 2.2), but only the most important Jurassic/Cretaceous one is marked in the cross-sections (Figs. 2.5, 2.6).

The Carboniferous and Permian successions are quite similar throughout the study area (Fig. 2.2). Also the sedimentation during the Triassic is comparable, but differences in thickness exist between the northern and southern part of the area. The Jurassic/Cretaceous unconformity

DOI: 10.2312/GFZ.b103-07087

truncates strata down to the Middle Jurassic in the southern part, but even down to the Upper Triassic in the northern part (Fig. 2.2). This led to a thick Jurassic succession of on average 1000 m in the southern part, whereas in the northern part these strata are absent. The thickness of Lower Cretaceous sediments differs in a complimentary manner: the northern part contains c. 800 m thick sediments, but only 150 m thick sediments in the southern part (Fig. 2.2). Only slight differences in thickness occur in the Upper Cretaceous and the Tertiary, where the sedimentary thickness increases gently towards the north.

Rheologically-weak rocks like salt can act as detachments. In the study area such detachment levels are recognised in the Zechstein and in the Middle Keuper (Fig. 2.2). The thickness of the mechanically weak Zechstein salt plays an important role in the evolution and structural style of the whole Southern Permian Basin, and is responsible for coupling or decoupling between pre- and post-Zechstein salt units. For that reason we distinguish between basement and cover in our working area. In this paper we define the pre-Zechstein salt units (Carboniferous, Rotliegend, and Zechstein anhydrite) as basement, but the post-Zechstein salt units (Mesozoic and Cenozoic rocks) as cover. The Top A2 horizon is a strong reflector representing an anhydrite of the lowermost Zechstein (Fig. 2.2), and marks the base of the Zechstein salt. It is the deepest regionally correlative seismic horizon.

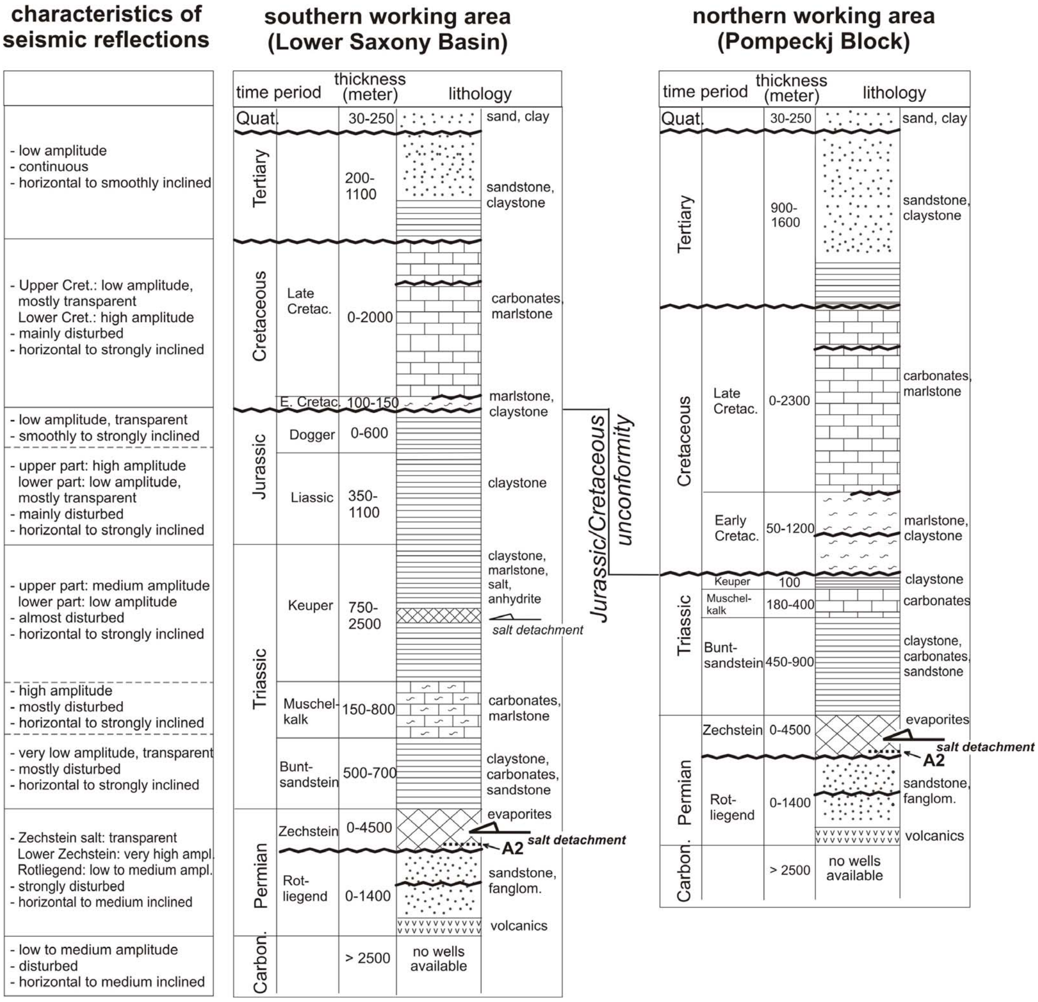

Figure 2.2: Generalised stratigraphy of the working area, separated for the Lower Saxony Basin (left) and the Pompeckj Block (right). The left column shows the general characteristics of seismic reflections. Lithology is normalised with the average thickness. Main unconformities are shown as sinuous lines.

DOI: 10.2312/GFZ.b103-07087

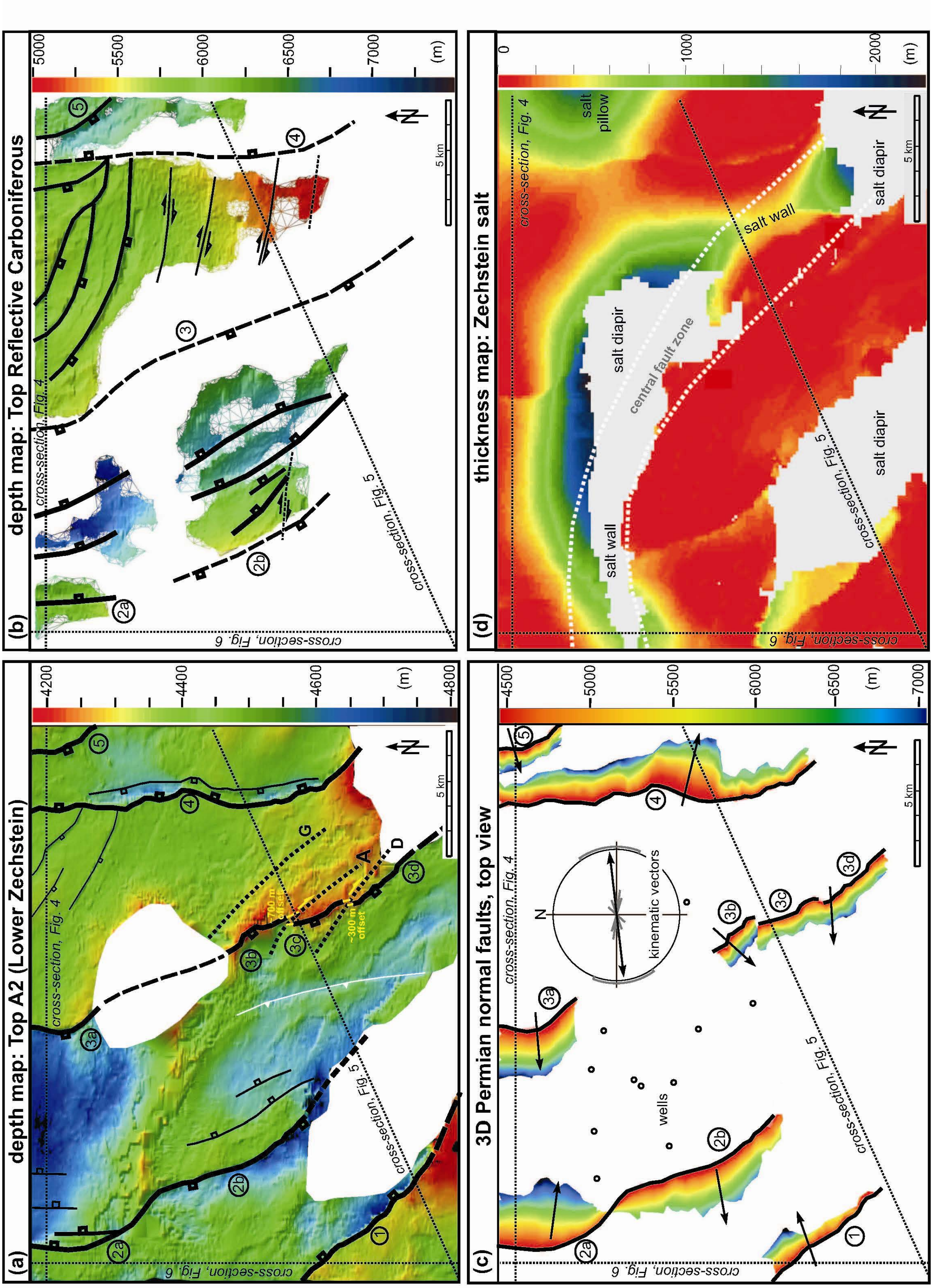

DOI: 10.2312/GFZ.b103-07087

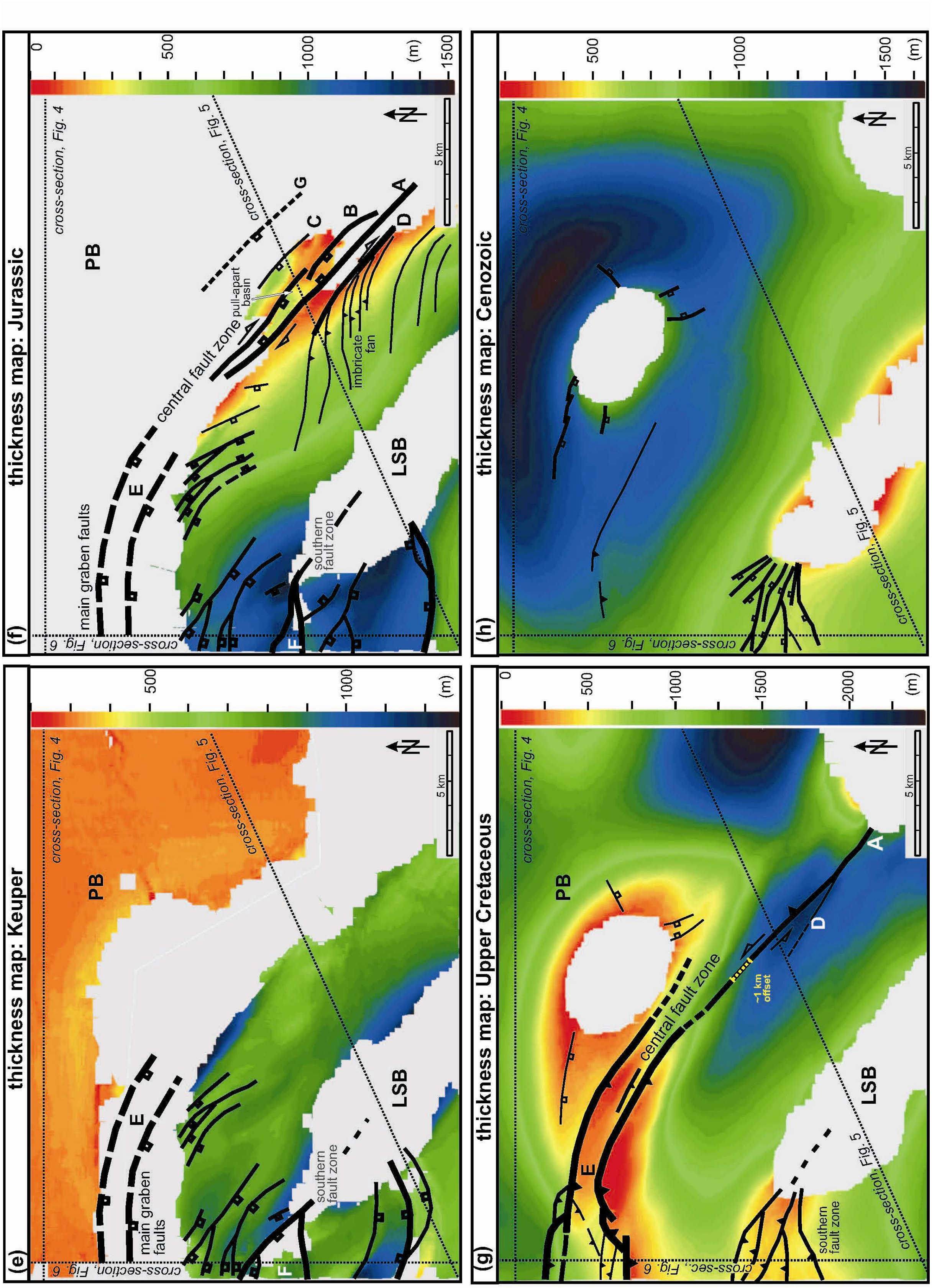

DOI: 10.2312/GFZ.b103-07087

Figure 2.3 (previous pages): Depth maps and thickness maps of selected horizons with structural interpretation. Compare structures observed on these depth and thickness maps with those in the cross-sections (Figs. 4, 5, 6). (a) Top A2 (Lower Zechstein) depth map. Dotted lines indicate the traces at depth of faults A, D, and G. (b) Top Reflective Carboniferous depth map, (c) 3D interpretation of Permian normal faults, top view, coloured by depth. The strong convolution of faults 3b, 3c, and 3d is caused by Mesozoic strike-slip faulting. Arrows indicate kinematic movement direction determined from fault morphology analysis. Insert diagram shows all kinematic vectors, thick vector is the mean, bars on the circumference of the circle indicate the range of data. (d) Zechstein salt thickness map. The area between the dotted lines represents the region, which is effected by movements along the central fault zone. (e) Keuper thickness map, (f) Jurassic thickness map, (g) Upper Cretaceous thickness map, (h) Cenozoic thickness map. Uniform grey regions are uninterpreted areas, due to lower seismic resolution caused by salt (Fig. 3a, b, d, e, f, g, h), by strong faulting (Fig. 3b, e, f), or by the absence of strata (Fig. 3b, f). The central fault zone is interpreted as the boundary between the Lower Saxony Basin (LSB) and the Pompeckj Block (PB). Circled numbers and letters mark selected faults, which are also shown in the cross-sections.

2.4.2. Carboniferous/Permian deformation

Two depth maps (Top A2 horizon, Fig. 2.3 a, Top Reflective Carboniferous horizon Fig. 2.3 b), and one cross-section (Fig. 2.4) illustrate the Carboniferous/Permian deformation. Correlation with well data identified a strong reflector directly underneath the Zechstein salt as the Top A2 horizon between 4 and 5 km depth (Figs. 2.3 a, 2.4), traceable over the whole area. Below the Rotliegend formations, the next identifiable feature is a series of strong and continuous reflections. Since well information did not reach these depths we interpret these reflections to possibly represent Carboniferous Westfalian coal layers. These "reflective Carboniferous horizons" are c. 1500 m below the Top A2 horizon (Figs. 2.3 a, b, 2.4). The well-known stage of initiation of the North German Basin in the Permian is well documented in this study area.

The oldest identifiable structures are nearly E-W trending faults in the eastern part of the study area (Fig. 2.3 b); the faults are vertical, showing no vertical displacement, but a small horizontal displacement of a few hundred metres. Therefore, we interpret these faults as strike-slip faults having right-lateral offsets. We estimate that fault activation has occurred in the Late Carboniferous and/or Early Permian.

We recognised normal faults in depth maps (Fig. 2.3 a, b) and on cross-sections (Fig. 2.4) forming a system of grabens and halfgrabens, which affected Carboniferous to Permian rocks. Normal faults show orientations from NW-SE to N-S, and dip from 50° to 70°. Structural interpretation in a seismic section (Fig. 2.4) illustrates three Rotliegend horizons R1, R2 and R3 within the graben in the NW of the study area, and shows the synsedimentary tectonic evolution of this graben. The deepest horizon R1 in approximately 6 km depth is postulated as Base Rotliegend. At the western graben flank, faulting started with normal faults which formed a half graben. The thickness of the Rotliegend sediments (R1 - R2) varies between 350 and 600 m, reaching the highest thickness in the western and central parts of the structure. In Late Rotliegend, graben subsidence changed to the eastern flank, indicated by the thickness change of the Upper Rotliegend sandstones (R3 - Top A2), and the development of an angular unconformity above the R3 horizon. The thickness of these sediments varies between 140 and 520 m, with the highest value in the eastern part of the structure.

Synsedimentary normal faulting continued during the Lower Zechstein and produced a vertical displacement of 200 to 300 m at the Top A2 horizon. The amount of extension of the graben was calculated along the Base Rotliegend horizon with 2700 m (24.5 %), and along the Top A2 horizon with 300 m (2.7 %). Activity along these normal faults during the Triassic was not observed.

DOI: 10.2312/GFZ.b103-07087

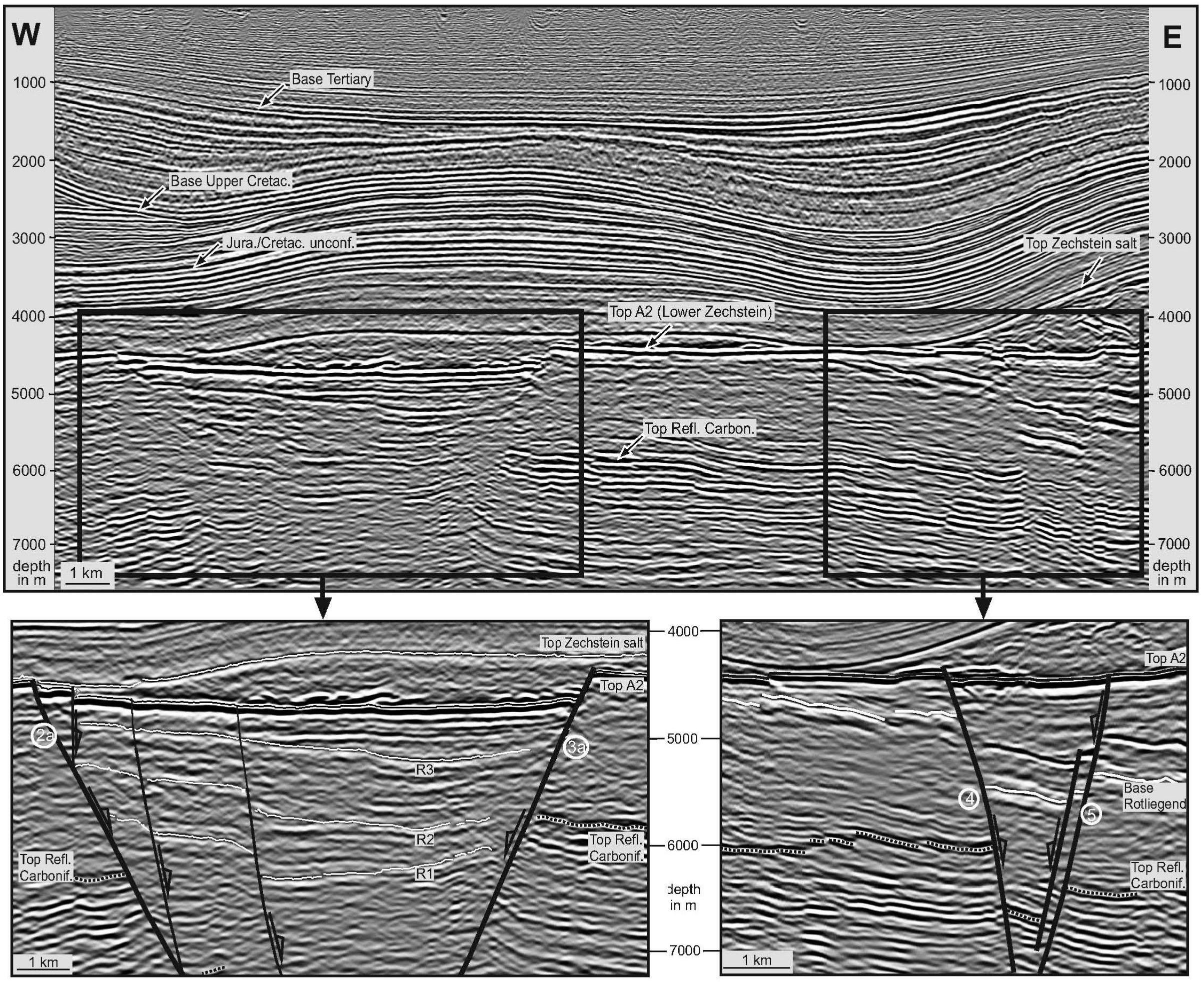

Figure 2.4: E-W oriented reflection seismic cross-section, shown as uninterpreted section (top) and with interpretations (bottom). Numbered faults as those in Fig. 3. Reflectors R1-R3 refer to Rotliegend horizons documenting Permian extension.

The synsedimentary tectonic evolution can also be observed within a smaller graben in the eastern part of the study area (Figs. 2.3 a, b, 2.4). Graben faults show a vertical displacement of 300 to 1100 m at the Base Rotliegend. Displacement at the Top A2 horizon reaches a maximum of 200 m. The amount of extension of the graben is calculated along the Base Rotliegend horizon with 250 m (14.3 %), whereas the extension along the Top A2 horizon is too small to have been measured. We assume that normal faulting probably started in the Early Permian and continued until the Late Permian.

NNW-striking normal faults have been identified in the north-eastern part of the area (Fig. 2.3 b). Because of their offsets in Carboniferous layers, we interpret them to have been initiated during Carboniferous or Early Permian. Very subtle offsets in the Top A2 horizon (Fig. 2.3 a) indicate either a continuous activity of these faults also during the Early Zechstein, or a higher compaction of Permian sediments within the hanging wall. The white coloured thrust fault at the Top A2 depth map is a Permian normal fault, which has been inverted during Late Cretaceous compression (see chapter 2.4.6).

Figure 2.3 c shows a map view of major Permian normal faults interpreted in 3D. The thick black lines represent the traces of faults on the Top A2 horizon. Coloured depth lines elucidate the undulation of the fault surfaces. The strike of these Permian graben faults, however, varies by 45°

between different faults, as well as along-strike of individual faults (Fig. 2.3 a, c, faults 2, 3, 4). Hence, the fault surfaces are strongly convoluted along strike. The undulations of fault planes result in varying dip directions of individual fault segments (in particular fault 4, Fig. 2.3 c). Therefore, we suggest that the presently-observed faults probably formed from smaller faults (c. 3 to 4 km) with varying dip, which coalesced through breached relay structures (for terminology refer to e.g. Trudgill & Cartwright, 1994; Walsh *et al.,* 2002 and references therein).

Moreover, we suggest that the slight undulation of fault surfaces reflects the orientation of the movement vector, because movement parallel to the axis of curvature should require least energy. However, the strong convolution between faults 3b, c, d (Fig. 2.3 c) was caused by Mesozoic strike-slip faulting along the central fault zone (will be explained in chapters 2.4.4. and 2.4.6.). To determine the orientation of the movement vector here, we studied the morphology of the Permian faults. The analysis of the fault topography highlights areas of similar curvature and cylindricity. These areas, if linear, were assumed to be fault corrugations. Our analysis suggests E-W to ENE-WSW directed movements (Fig. 2.3 c). Typically, as well as following fault corrugations, fault displacement is near parallel to the fault dip (i.e. dip-slip). The range of slip direction is approx. 45°, similar to the variation in fault strike (Fig. 2.3 c).

2.4.3. Zechstein salt

Zechstein evaporites cover the Carboniferous/Rotliegend grabens. The top and base of the Zechstein salt has been interpreted, and a thickness map was compiled (Fig. 2.3 d), indicating thickness variations of up to 1600 m. The top of the Zechstein salt is a single-phase continuous reflection, bounding the more transparent salt. These zones are easily detectable in the seismic image due to their high-amplitude reflections, and their almost vertical internal diffractions (e.g. Fig. 2.4). Today, the thickness of the Zechstein salt is very variable (0 to 1600 m in mapped areas, up to 4500 m at salt diapirs) due to halokinesis. The study area is characterised by several salt structures: three diapirs, two salt walls, and one salt pillow (Fig. 2.3 d). Salt rise into diapirs resulted in depletion of the salt around the diapir, which typically lead to the formation of marginal rim synclines in the sediments above. Along the margins of the diapirs, salt movement affected Mesozoic and Cenozoic sediments by upward bending (e.g. Figs. 2.5, 2.6). Diapirism started in Keuper and Jurassic (chapter 2.4.4.), but the main phase of diapirism was during the Late Cretaceous (chapter 2.4.6.), and the Cenozoic (chapter 2.4.7.).

2.4.4. Late Triassic and Jurassic deformation

Two thickness maps of Keuper (Late Triassic) and Jurassic (Fig. 2.3 e, f), and two seismic cross-sections (Figs. 2.5, 2.6) illustrate the Late Triassic to Jurassic deformation. The Keuper thickness map illustrates a strongly reduced, but constant thickness (c. 350 m) in the northern part, whereas in the southern part the thickness is much higher and shows stronger variations (500 to 1200 m) (Fig. 2.5). This southern part is characterised by E-W to NW-SE trending normal faults, which accumulated a high amount of sediments in their hanging walls during the Keuper (Figs. 2.3 e, 2.6). In section view (Fig. 2.6) we recognised normal faults bounding grabens and halfgrabens. The most prominent normal fault detached along a Middle Keuper salt layer, and soled out into the Zechstein salt. We determine this fault as main graben fault (marked with a bold line and labelled as E in Figs. 2.3 e, f, 2.6). The main graben fault proceeds into several imbricate listric normal faults, building a roll-over anticline and tilted blocks (Fig. 2.6). Minor faults in the hanging wall of the main graben fault developed primarily during the Keuper and Liassic, but in the Dogger displacement occurred predominately along the main graben fault, which led to a wedge-shaped synsedimentary accumulation of 400 m Dogger sediments on top of the roll-over. Faulting might have continued also until the Malm, or possibly until the Lower Cretaceous, but

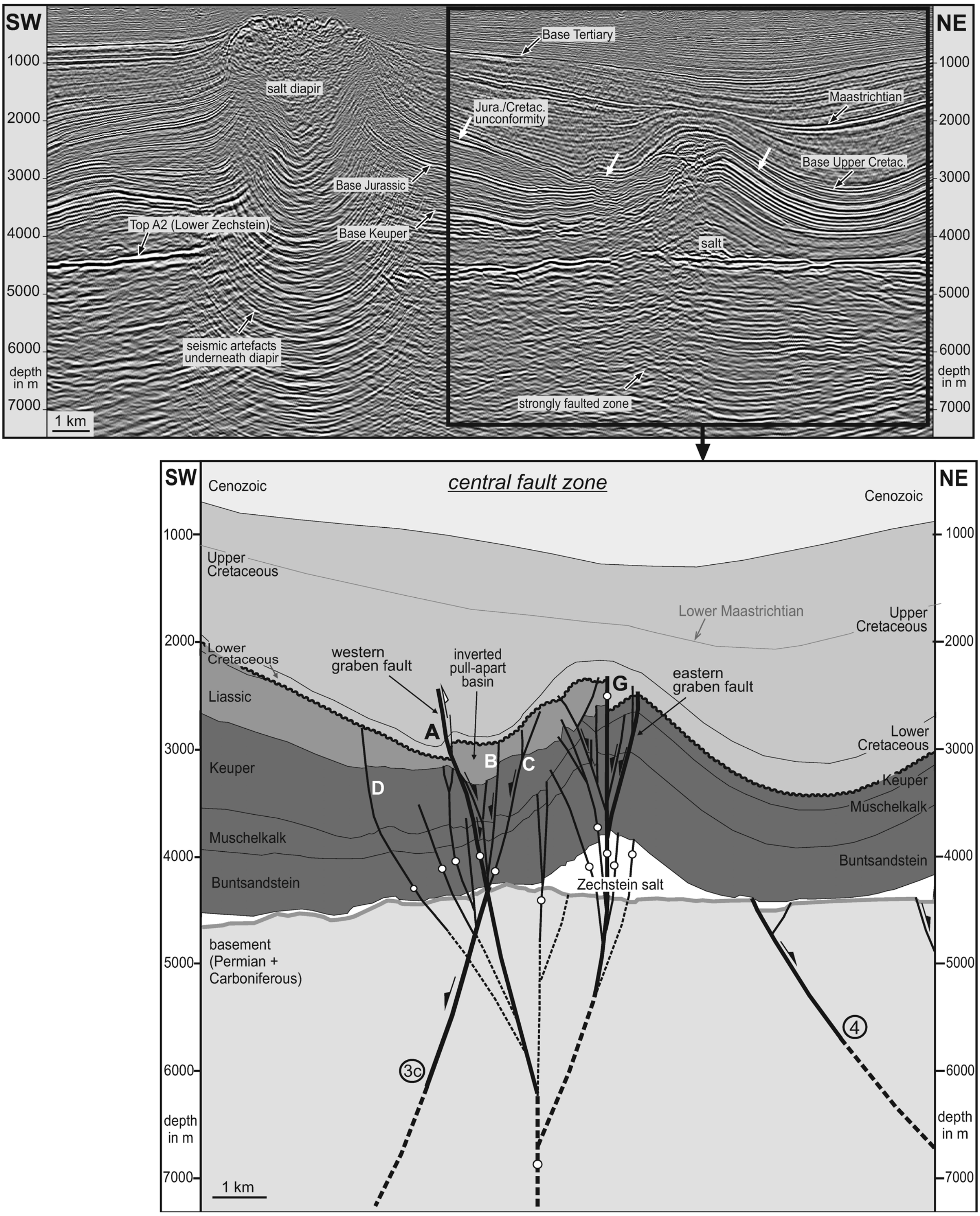

Figure 2.5: SW-NE oriented reflection seismic cross-section, shown as uninterpreted section (top) and with interpretations (bottom). Dotted faults are of uncertain location. White circles represent strike-slip faulting with undefined shear sense. Sinuous line marks the Jurassic/Cretaceous unconformity. The labelled faults A to D and G represent those in Fig. 2.3.

DOI: 10.2312/GFZ.b103-07087

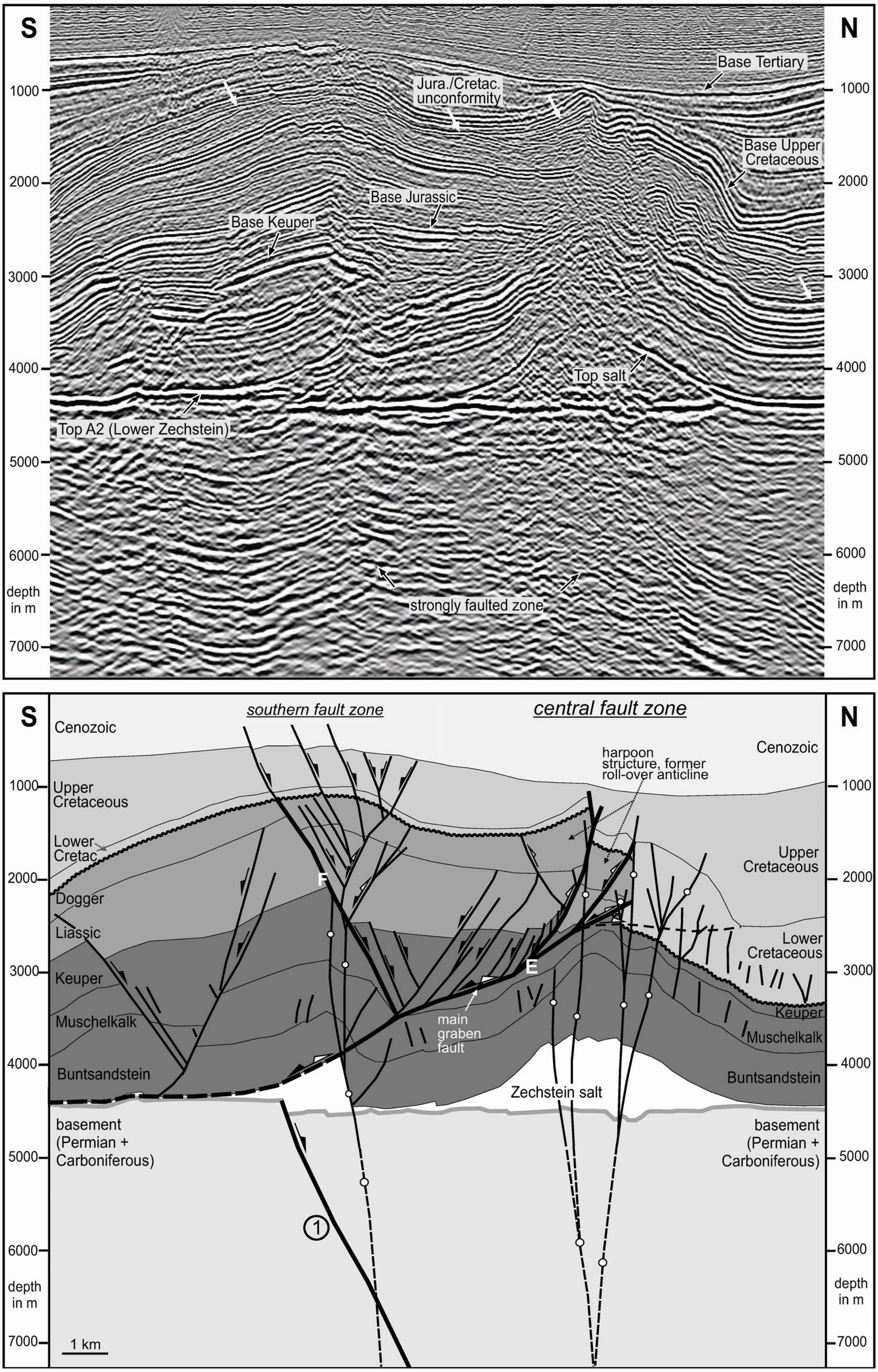

Figure 2.6: N-S oriented reflection seismic cross-section, shown as uninterpreted section (top) and with interpretations (bottom). Dotted faults are of uncertain location. White circles represent strike-slip faulting with undefined shear sense. Sinuous line marks the Jurassic/Cretaceous unconformity. The labelled faults E and F represent those in Fig. 2.3.

DOI: 10.2312/GFZ.b103-07087

this cannot be proven because these sediments are eroded. Further to the south a normal fault (marked with a bold line and labelled as F in Fig. 2.6) developed antithetically to the main graben fault, synsedimentary during the Jurassic.

Steep faults characterise the eastern part of the study area. There is an increased thickness of Jurassic sediments (Fig. 2.5), which points to extension and graben development between fault A as western graben fault, and fault G as eastern graben fault. The Jurassic fault pattern (Fig. 2.3 f) illustrates NW-trending faults, bounding a basin between fault A and B (compare with Fig. 2.5). The basin is about 8 km long, and varies in width between 500 and 1000 m. During basin formation 300 to 400 m thick Liassic sediments were accumulated. The fault pattern could be interpreted as extensional system with relays, or as pull-apart basin. In the case of an extensional system, these normal faults could be newly formed during Jurassic and root into the Zechstein salt detachment, or they could be continuations of basement faults that have been reactivated. 3D seismic interpretations suggest a continuation of the Jurassic faults into the basement (Fig. 2.5). Comparison between basement faults and the Jurassic fault pattern demonstrates a difference in strike of structures of about 20° (Fig. 2.3 a, f). By following the Jurassic basin fault A into the depth (Fig. 2.3 a, f), its trace matches with a gap between the underlying Permian normal faults 3b and 3c. We interpret this gap to be caused by horizontal movement along steep faults. For these reasons we suggest that the Jurassic basin faults are not reactivated Permian normal faults, but they crosscut these faults and have been developed as transtensional faults forming a pull-apart basin, due to strike-slip faulting in the depth. However, in areas of fault intersections there could also be a reactivation of Permian normal faults by the Jurassic faults, but we exclude a reactivation over larger areas.

South of the pull-apart basin we detected steep faults, striking E-W, and dipping 50° to 90° mainly towards south (Fig. 2.3 f). The lower thickness of Jurassic sediments in their hanging wall indicates them as thrust faults. We interpret this fault pattern as contractional imbricate fan, which bends into fault D (Fig. 2.3 f). Both, the pull-apart basin and the imbricate fan can be explained by a superimposed transtensional regime during the Jurassic. However, because of the close location to a salt diapir in the south, it is likely that this thrust pattern is also influenced by local compression of the diapir.

The major fault systems which accumulated deformation during the Triassic and Jurassic (including faults A to G, Fig. 2.3 e, f) are aligned as NW-trending fault zone. Due to the importance of this zone (described as well in the next chapters) we determine this fault zone as the "central fault zone" of the working area.

2.4.5. Late Jurassic/Early Cretaceous deformation

The Jurassic/Cretaceous unconformity (Figs. 2.5, 2.6) truncates strata down to the Dogger in the S, but also down to the Keuper in the N. This unconformity shows an angular contact between Dogger and Lower Cretaceous strata in the south, but a conformable contact between Keuper and Lower Cretaceous strata in the N. Due to the different levels of erosion, the Jurassic strata have a thickness of up to 1500 m in the south, but in the north Jurassic strata are absent. The strong and parallel reflections of Lower Cretaceous sediments describe a high thickness of 400 to 800 m in the north, and a low thickness of only 100 m in the south (Figs. 2.5, 2.6). Within the Lower Cretaceous an angular unconformity can be recognised in the northernmost part of both lines. The reason for this unconformity is not detectable, due to the limited size of the study area.

Deformation in the Upper Jurassic/Lower Cretaceous was not observed along individual faults. However, across the NW-trending central fault zone the Mesozoic sedimentary style differs strongly (see Figs. 2.3 e, f, 2.5, 2.6). The northern part of the study area is characterised by condensed Keuper sediments (constant 200 m thickness, Fig 2.3 e) and missing Jurassic sediments (Fig. 2.3 f), but an increased Lower Cretaceous sedimentation (50 to 1200 m thickness). The southern part contains 500 to 1200 m thick Keuper sediments and also Liassic and Dogger, but these Jurassic sediments thin out towards the NE (Fig. 2.3 f). Only 100 m of Lower Cretaceous are documented here.

2.4.6. Late Cretaceous deformation

The Upper Cretaceous thickness map (Fig. 2.3 g) and two seismic cross-sections (Figs. 2.5, 2.6) illustrate the Late Cretaceous deformation. The thickness map shows no differences between the northern and the southern part of the study area, but local differences because of salt diapir evolution. Areas of increased Upper Cretaceous thickness (more than 1250 m) represent salt rim synclines. Areas with reduced thickness are related to diapir growth, or to tectonic activity.

We recognised compressional faulting along the central fault zone, and along a fault zone further south (Figs. 2.3 g, 2.5, 2.6). Compressional deformation began after the Jurassic/Cretaceous erosional unconformity had developed, and led to inversion of the large graben structure (fault E in Fig. 2.6). Inversion was concentrated predominantly along the former main graben fault, which soled out into the Zechstein salt layer. However, the smaller-scale listric normal faults, which bound the tilted blocks, show almost no inversion. The reason for this preferred inversion along the main graben fault was probably due to a lower friction during gliding on the Middle Keuper salt detachment. The northernmost listric normal faults of the roll-over anticline were reactivated as several imbricate thrust faults (Fig. 2.6). The thereby produced harpoon structure incorporated a sedimentary Jurassic infill of several hundred metres (Fig. 2.6), covering an area of about 2 x 5 kilometres (Fig. 2.3 g). The vertical displacement along the imbricate thrust faults is several hundred metres, but bedding-parallel shortening along the former main graben fault is in the order of several kilometres. Correlation of tectonically controlled onlap structures with well data indicates that inversion occurred after the Coniacian and continued until the Maastrichtian, partly continuing until the Palaeocene.

In the eastern part of the working area we observed faulting along the central fault zone during the Late Cretaceous (Figs. 2.3 g, 2.5, 2.6). Reactivation is indicated by offset or bending of Upper Cretaceous reflectors, and by a reduced sedimentary thickness (Figs. 2.3 g, 2.5). We suggest that the Jurassic pull-apart basin (Fig. 2.3 f) has been uplifted, and changed into a pop-up structure during the Late Cretaceous, in which fault A was reactivated as thrust fault (Figs. 2.3 g, 2.5). Correlation with well data suggests that inversion along this fault occurred during the Santonian to Campanian. Vertical offsets vary between 100 to 200 m along strike. Due to abrupt changes in thickness of Upper Cretaceous sediments (Fig. 2.3 g), we interpret a sinistral horizontal offset along fault A of about 1 km. Dip-slip thrusting along this fault would have led to an apparent dextral offset of the isopachs, whereas the currently observable sinistral offset of 1 km is only possible with strike-slip or oblique-slip kinematics of more than 1 km. Further to the east, the area of fault G shows no evidence for faulting during Late Carboniferous (Fig. 2.5). However, the reduced thickness of Upper Cretaceous carbonates points to uplift in this area (Fig. 2.3 g). Onlap structures indicate uplift during Santonian to Maastrichtian of about 400 to 600 m along this zone. This uplift was probably caused by salt migration only, because changes in Zechstein salt thickness are in the same order (400 to 1000 m along this zone). Intense subsidence occurred during the Maastrichtian, which led to an accumulation of nearly 1000 m of sediments (Fig. 2.5).

DOI: 10.2312/GFZ.b103-07087

The reduced thickness of Upper Cretaceous sediments in the area of the southern fault zone suggests uplift during that time (Figs. 2.3 g, 2.6). This uplift might have been caused by reactivation of the Jurassic graben fault F and its branch faults (Fig. 2.6).

In the area of the central fault zone underneath the two salt walls, we observed an upward bending of seismic reflectors, which we interpret as uplift of Upper Permian horizons. The Top A2 horizon is locally uplifted 100 to 300 m above the surrounding surface (Fig. 2.3 a). This uplift could be also a seismic artefact due to velocity pull-up underneath the salt walls (Fig. 2.3 d). However, the salt walls are not thick enough (average 500 m, Fig. 2.3 d) to cause such big artefacts; and numerous wells penetrating this zone (Fig. 2.3 c) provided evidence that the position of the Upper Permian horizons is correct. Furthermore, seismic reflectors underneath this zone have been strongly destructed vertically, which we interpret as vertical faults belonging to the central fault zone (Figs. 2.5, 2.6). Therefore, we interpret this uplift to be caused by horizontal movements along the central fault zone during Late Cretaceous inversion. Here, salt might have acted as free surface, and transpression than produced positive flower structures in the rocks underneath the salt.

2.4.7. Cenozoic deformation

Mesozoic faulting was followed by Cenozoic subsidence that is indicated by a widespread cover of Tertiary and Quaternary sediments. The Base Cenozoic erosional unconformity generally levelled the deformed pre-Cenozoic succession. Cenozoic strata are characterised by horizontal continuous reflectors diverging towards the N (from 500 m to 1200 m), which indicates higher subsidence further north (Fig. 2.3 h). Local thinning and thickening of strata occurs above or around salt diapirs and is primarily related to their Cenozoic rise or withdrawal.

The Cenozoic is characterised by a general tectonic quiescence. Salt rise during the Cenozoic probably initiated normal faulting around salt diapris (Fig. 2.3 h). Additionally, in the western part of the study area we observed faulting along the central fault zone (Fig. 2.3 h), which indicates minor compressional deformation during the Palaeocene (Lower Tertiary) as continuation of Upper Cretaceous inversion. Faulting occurred also along the southern fault zone. Here, normal faulting was initiated by salt rise of a nearby located diapir (Figs. 2.3 h, 2.6), and faults of the southern fault zone have been reactivated as dip-slip normal faults.

2.5. Discussion

2.5.1. Kinematics derived from structures

The basement of the whole study area is characterised by a system of mainly N- to NW-trending Permian graben faults, whereas post-Permian deformation is marked by mainly W- to NW-trending faults covering the Permian structures. Since the Jurassic, the sedimentation and the structural style led to a differentiation of the study area into a northern and a southern domain. Mesozoic deformation was concentrated primarily within the southern domain, whereas the northern domain was almost undisturbed (Fig. 2.3 e to h). For these reasons we interpret the central fault zone to be the Aller-lineament, which is the boundary between the Pompeckj Block to the north and the Lower Saxony Basin to the south. From fault pattern of the interpreted structures we derived the following kinematics (Fig. 2.7):

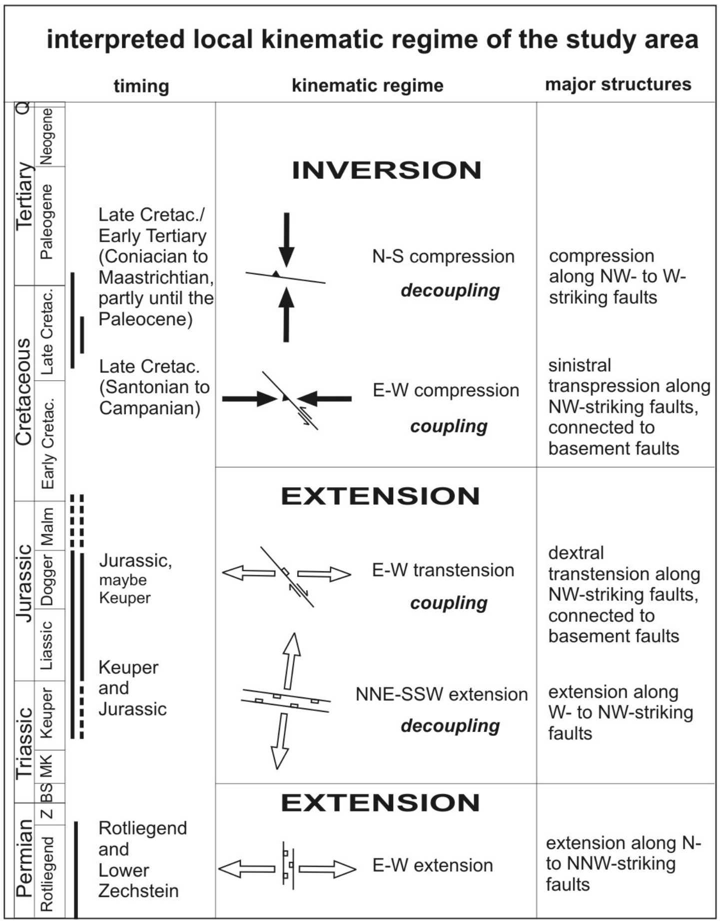

Figure 2.7: Summary of tectonic events for the study area, with major structures and derived kinematic regime. White arrows indicate horizontal extension direction; black arrows indicate horizontal compression direction. Abbreviations: Z - Zechstein, BS - Buntsandstein, MK - Muschelkalk, Q - Quaternary.

Carboniferous/Permian

Synsedimentary Permian extension produced a system of grabens and halfgrabens striking N to NW, which affected Carboniferous to Permian rocks. Rifting started probably in the Early Rotliegend and continued until the Early Zechstein. However, due to the limited depth of the wells the timing of onset of normal faulting can only be estimated. Orientation and kinematics of basement faults indicate an extensional kinematic regime during the Permian with nearly E-W horizontal extension direction (Figs. 2.3 c, 2.7). This coincides well with the overall suggested E-W extension and development of roughly N-S oriented grabens during the Latest Carboniferous to Permian (e.g. Ziegler, 1990; Betz *et al.,* 1987).

Late Triassic and Jurassic

Within the western part of the study area we interpret a NNE-SSW directed thin-skinned extension along NNW-trending normal faults during the Keuper (Upper Triassic) and Jurassic. Within the eastern part we propose a thick-skinned dextral transtension along NW-striking faults during the Jurassic, caused by horizontal E-W extension direction (Fig. 2.7). Whether transtensional movements within the basement continued also further to the west, and if they were active already during the Keuper, cannot be proven due to the occurrence of salt that hampers the resolution of the seismic data in this area. The timing of extension recognised in our working area is consistent with those of large N-S trending grabens further north, which initiated during the Triassic, like the Central Graben (Ziegler, 1990), the Horn Graben (Best *et al.,* 1983), and the Glückstadt Graben (Maystrenko *et al.,* 2005).

DOI: 10.2312/GFZ.b103-07087

We calculated the horizontal displacement in the western part of the study area during thin-skinned Triassic/Jurassic extension, and determined an extension of c. 2 km. This minimum amount was calculated by (1) the sum of extension on each normal fault (along the Top Keuper strata) of the half graben between the two fault zones, and the graben in the southern part of the sections, (2) plus the required extension to accumulate the minimum 400 m thick Dogger sediments that form the roll-over anticline. However, the calculated amount is a minimum estimate, because of unknown thicknesses of Dogger and Malm sediments before erosion, and later inversion tectonics along the main graben fault.

We also calculated horizontal displacement during strike-slip faulting. By following the trace of faults A and D (Fig. 2.3 a, f, g) down to the Top A2 horizon, a horizontal offset of a Permian normal fault (3b, c, d in Fig. 2.3 a) is documented. Here, the normal fault is truncated, caused by horizontal movements along faults A and D. The apparent dextral offset of c. 700 m along fault A is the final result of Jurassic dextral and Late Cretaceous sinistral strike-slip faulting (this will be explained in chapter 2.5.1. *Late Cretaceous*). Both offsets (700 m along Top A2 depth map, and 1000 m in the Upper Cretaceous thickness map) suggest a minimum displacement of 1700 m along fault A during Jurassic dextral strike-slip faulting. The incremental and cumulative displacement along the prevailing fault A is not the absolute deformation along the whole strike-slip zone. Several smaller faults within this zone may have accumulated an additional amount of strain by horizontal offsets. Indeed, fault A accumulates a large amount of the total displacement during strike-slip faulting, but other parts of the fault zone may accumulate displacement in the same or higher order. However, because of salt occurrence within this zone, data quality is locally worse and complicates the calculation of superimposed displacements. Nevertheless, we assume that the total horizontal displacement at this part of the central fault zone amounts to only a few kilometres.

On a regional scale Ziegler *et al.* (2001) and Ziegler & Dezes (2006) described that during the Triassic and Jurassic a multi-directional rift system with associated wrench movements developed, which led to crustal separation in Western and Central Europe. During this deformation Permo-Carboniferous fracture systems were involved partly, and some areas (e.g. Central Graben, Horn Graben, Glückstadt Graben) underwent extensive crustal extension and crustal thinning (Ziegler *et al.,* 2001; Ziegler & Dezes, 2006). The area of the later LSB participated in that deformation only to a minor amount, expressed by the small N-S oriented Emsland Trough and Weser Depression. Therefore, this region appears to be the southernmost extent of intensive Triassic extension occurred further north, and the Aller-lineament might have acted as barrier zone that calmed any deformation further south.

Late Jurassic/Early Cretaceous

The primary sedimentary features are the thinning of Keuper sediments, the lack of Jurassic sediments, and an increase in Lower Cretaceous sedimentation north of the central fault zone with respect to the south. The high accumulation of Jurassic sediments within the southern part, and the high erosion within the northern part contemporaneously, could be explained by strong subsidence of the southern part with respect to the northern part, occurred during Early Cretaceous and/or Late Jurassic.

The contrasting pattern of sedimentation and erosion during the Late Jurassic/Early Cretaceous is recognised also throughout the NW German Basin, in which it is used to distinguish between the Pompeckj Block (PB) north of the Aller-lineament, and the Lower Saxony Basin (LSB) south of the Aller-lineament (e.g. Betz *et al.,* 1987; Best, 1996; Hoffmann *et al.,* 1998; Kockel, 2003; Frisch & Kockel, 2003, Scheck-Wenderoth & Lamarche, 2005). In the study area this unconformity is documented in the north as a disconformity, whereas in the south it is a low-angle unconformity (Figs. 2.5, 2.6). Because we observed these typical sedimentation and erosion pattern in our study area, we interpret the area north of the central fault zone as Pomeckj Block, and the area south of the central fault zone as Lower Saxony Basin. The central fault zone itself is a key part of the Aller-lineament.

Comparing the LSB and PB in this study (Figs. 2.5, 2.6), the differences in sedimentation and erosion require either basement offsets, or strong salt movements to accumulate several kilometres of Jurassic sediments in the area of the LSB, and to contemporaneously erode strata down to Keuper in the PB. Extensive basin wide salt movements causing constant uplift of an area more than hundred km in diameter is rather unlikely, because salt would tend to rise inhomogenously, especially in areas with differences in sedimentary thickness, or strong faulting. Another possibility could be tectonically caused basement uplift. However, there is no evidence for significant basement offset along the Aller-lineament, neither in our study area, nor in other studies; but a tectonic uplift and later subsidence to exactly the same original level is very unlikely. However, another explanation could be a regional thermal uplift and later subsidence. Because Ziegler & Dezes (2006) suggested that during the Late Jurassic and earliest Cretaceous accelerated rifting activity occurred for example in the Central Graben of the North Sea rift, which was related to the development of shear systems at its southern termination, controlling the subsidence of trantensional basins like the Sole Pit, Broad Fourteens, West Netherlands, and Lower Saxony Basin. This transtensional concept for Jurassic/Cretaceous deformation for the LSB was also suggested by Mazur & Scheck-Wenderoth (2005) and Betz *et al.,* (1987). In the post-rift phase after the Late Jurassic/Early Cretaceous rifting, thermal subsidence of the North Sea Basin began, and affected also areas further south (Ziegler & Dezes, 2006).

Late Cretaceous

Within the western part of the working area we observed inversion along W- to NW-striking faults, which led to thin-skinned thrusting along Zechstein and Keuper salt detachments. To explain this fault pattern, we interpret a N-S compression direction. A minimum amount of 2 km inversion during N-S compression can be calculated by the displacement of the several imbricate thrust faults (Fig. 2.6). However, this amount is also a minimum estimate due to the minimum estimated amount of extension before inversion. In this western part inversion occurred from the Coniacian and continued until the Maastrichtian, partly continuing until the Palaeocene (Fig. 2.6).

Further to the east we identified faulting along NW-striking faults. Figure 2.3 g shows changes in thickness of Upper Cretaceous sediments on both sides of fault A, producing a bending of the isopachs of about 1000 m. Simple top-SW thrusting along fault A would led to an apparent dextral offset of the isopachs, whereas the currently observable sinistral offset of 1000 m is only possible with strike-slip or oblique-slip kinematics of more than 1000 m. Therefore, we suggest that along fault A occurred a minimum sinistral horizontal offset of 1 km during thick-skinned transpressional inversion tectonics, and we derive a horizontal compression direction of roughly E-W. Inversion took place during Santonian to Campanian, which is documented by onlap-structures of the Upper Cretaceous carbonates (Fig. 2.5).

At the Top A2 depth map we identified a N-S trending fault, which we interpret as a Permian normal fault that has been inverted during Late Cretaceous compression (white coloured thrust fault in Fig. 2.3 a). The timing of reactivation was determined to be Late Cretaceous because fault orientation fits to the proposed E-W compression during this time, the only compressional phase observed in the study area. However, an offset of Mesozoic horizons could not be identified, maybe due to decoupling and buffering of overlaying Zechstein salt during that time. This fault is

DOI: 10.2312/GFZ.b103-07087

the only Permian normal fault that has been later inverted; all other large normal fault remained not reactivated. The reason for this preferred reactivation could be its gentle dip, which makes it easier to reactivate than the other large and steep normal faults. Additionally, apart from the reactivation of steep strike-slip faults, we assume that basement inversion in this area might have occurred only at a small-scale that affected mainly faults and fractures below the seismic resolution. That means, that the basement underwent shortening even though in a scale below the seismic resolution, but it might be significant for calculation of shortening in crustal-scale.

The timing of inversion observed in our working area is comparable with the general inversion of the LSB identified by other studies (e.g. Betz *et al.,* 1987; Kossow & Krawczyk, 2002; Mazur & Scheck-Wenderoth, 2005), but also with other basins along the southern margin of the SPB, like the Sole Pit, Broad Fourteens, and Netherlands Basins (de Jager, 2003 and references therein). There are minor differences in the timing of inversion between the several basins, which are mainly caused by the preferred reactivation of inherited structures depending on their orientation to the regional stress field (de Jager, 2003). Differences within the LSB might be related mainly to the selective nature of 2D seismic lines, in which differences between salt-related or fault-related unconformities are not easily resolvable.

On a regional scale, Late Cretaceous inversion of the LSB is caused by roughly NW-SE convergence between the European and African plates (e.g. Ziegler, 1982, 1990; Betz *et al.,* 1987). In our study area, heterogeneous fault patterns associated with Late Cretaceous inversion indicate that deformation varied temporally from the Coniacian to the Palaeocene along strike of the central fault zone. We identified coupling (involving basement and cover) associated with E-W transpression, and decoupling (involving only cover) associated with N-S compression. We assume that the contrasting local stress fields are caused by coupling/decoupling between basement and cover, which might have led to stress partitioning of the regional NW-SE convergence regime into a E-W component and a N-S component.

Vertical uplift during Late Cretaceous inversion is demonstrated by the difference in stratigraphic depth of the Jurassic/Cretaceous unconformity between the Lower Saxony Basin (LSB) and Pompeckj Block (PB). Since the amount of extension (during Keuper/Jurassic normal faulting), and the amount of compression (during Late Cretaceous inversion) are in the same order, the amount of vertical uplift is equivalent to the thickness of Keuper and Jurassic sediments accumulated within the LSB. We calculated an uplift of 1 to 2 km of the LSB with respect to the PB in our working area. This amount of vertical movement coincides with values of other locations: e.g. Van Wijhe (1987) proposed a 2 to 2.5 km uplift of the Broad Fourteens Basin, the hanging wall of the Harz Northern Fault was uplifted more than 4 km (Kockel, 2003), Kossow & Krawczyk calculated an upthrust of 3.5 km along the Gardelegen Fault within the NE German Basin, and the uplift of the Mid-Polish trough is estimated at 2 to 2.5 km (Dadlez *et al.,* 1997).

Cenozoic

The Cenozoic is characterised by subsidence and contemporaneous salt diapir rise with normal faulting. Only in the western part of the working area we observed tectonically induced faulting (Fig. 2.3 h), which we interpret as continued Late Cretaceous N-S compression along the central fault zone throughout the Palaeocene (Lower Tertiary).

Similar to our study area, other authors (Scheck-Wenderoth & Lamarche, 2005; Mazur & Scheck-Wenderoth, 2005; Maystrenko *et al.,* 2005) also described a general increase of subsidence towards the north, in the area of the Pompeckj Block. The continuation of Alpine collisional processes during the Palaeocene involved broad lithospheric folding and faulting, but led also to

DOI: 10.2312/GFZ.b103-07087

an accelerated subsidence of the North Sea Basin throughout the Cenozoic (Ziegler, 1990; Ziegler & Dezes, 2006).

2.5.2. Deformation around the Aller-lineament

Deformation along the central fault zone, which we interpret to be a part of the Aller-lineament, indicates activity at least since the Keuper, but reactivation and inversion continued during the entire Mesozoic and partly to the Lower Tertiary. The subdivision of the NW German Basin into the Lower Saxony Basin (LSB) and the Pompeckj Block (PB) along the Aller-lineament has been recognised by a period of subsidence during Jurassic and Early Cretaceous, not only in this study area, but also in the whole LSB (e.g. Betz *et al.,* 1987; Kockel, 2003; Mazur & Scheck-Wenderoth, 2005).

In the study area, roughly NNE-SSW directed extension is inferred for the Keuper and Liassic, which led to the development of listric graben faults. The main graben fault is part of the Aller-lineament, and dips toward the south (Figs. 2.3 c, d, 2.6). The kinematic regime required for the fault patterns observed in the study area, has been recognised neither in the LSB nor in the PB on a larger scale. Instead, during this time, several N- to NNE-striking elongated grabens (e.g.: Central Graben, Horn Graben, Glückstadt Graben, Emsland Trough, Weser Depression) developed, indicating E-W extension. However, in the south-eastern prolongation of the Aller-lineament, south of the Flechtlinger High, Best (1996) recognised in several 2D seismic lines graben faults similar to those observed in our study area. He described listric normal faults dipping toward the SW, which developed during Late Triassic and Early Jurassic times. The main graben fault crops out at the surface and its lateral extension corresponds to the Aller-lineament (Best, 1996). Movement along this fault was accommodated primarily by a detachment on Zechstein salt, but subordinately also on an internal unit of Upper Buntsandstein salt (Best, 1996). The structures described by Best (1996) refer to a NE-SW-orientated horizontal extension direction during Keuper and Liassic (Early Jurassic). Due to the similarity in timing and orientation of structures in both study areas, we suggest the same deformational mechanism underlying the structures observed in this study. Because of the relative local occurrence, we propose that the extensional style at this time is typical for the area along the Aller-lineament.

Jurassic deformation produced a complex fault pattern of dip-slip and oblique-slip normal and thrust faults, as well as strike-slip faults, contemporaneously within the study area (Fig. 2.3 f). Heterogeneous fault patterns associated with Upper Cretaceous inversion indicate that deformation varied temporally from the Coniacian up to the Palaeocene over short distances, along a 24 km long part of the central fault zone (Fig. 2.3 g). Furthermore, comparing the different timing of Upper Cretaceous inversion of the study area with those of the LSB indicates that deformation of the study area varies in the same manner as in the whole LSB (e.g. Betz *et al.,* 1987; Baldschuhn *et al.,* 1991; Kockel, 2003). At the scale of the analysed data, the regional boundary conditions are obscured by local ones.

We suggest that the heterogeneity in distribution and timing of deformation along the Aller-lineament is not primarily caused by regional boundary conditions, such as the regional stress regime, but rather by local ones. One reason might be the existence and orientation of older faults, as they can act as weak zones and are therefore preferable for reactivations. Another important parameter is the variation of salt thickness through time, as it can produce detachment levels depending on the stage of salt movement. Furthermore, salt walls can also act as weak zones preferable for faulting. For these reasons we suggest that both pre-existing faults and diapirism led to stress perturbations and therefore local strain partitioning. Additionally, areas with higher salt thickness trigger a decoupling of the stress field between basement and cover.

Therefore, we explain the different stress regimes identified in our working area, with stress partitioning: During Late Cretaceous inversion, stress partitioning led to a differentiation of the regional NW-SE convergence regime into an E-W compressional component affecting primarily the basement, and a N-S compressional component affecting only the cover in our working area. The N-S extension that occurred during Triassic/Jurassic within the cover might have caused only subsequently as result of the development of accommodation space and subsequent salt rise, due to regional E-W extension and consequent transtension along the Aller-lineament. Therefore, we do not agree with Best (1996) that N-S extension initiated salt migration along the Aller-lineament. Instead, we suggest that transtensional faulting within the basement triggered salt migration, which finally initiated local N-S extension within the cover.

Furthermore, the Aller-lineament could have acted as stress concentrator which might have reduced the magnitude of Triassic/Jurassic E-W extension to continue towards the south. South of the Aller-lineament, the area of the LSB underwent only minor extension resulting in the formation of the Emsland Trough in the outer west and Weser Depression in the outer east (Betz *et al.,* 1987), but the central parts of the LSB subsided only moderately.

2.5.3. Interaction between faulting and salt movements

Salt migration started in Keuper and Jurassic, but the main phase of diapirism was during the Late Cretaceous and Cenozoic (Figs. 2.5, 2.6), which resulted in the three diapirs identified within the working area. The location of salt walls, connecting the diapirs, corresponds with zones of intense Mesozoic fault activity (Fig. 2.3 d). Uplift of Mesozoic sediments along the salt walls and the subsidence around their rims, indicates the formation of the salt walls during the Late Cretaceous, but it stopped before the Maastrichtian (Fig. 2.5). Conversely, Cenozoic subsidence led to a higher accumulation of sediments immediately above the uplifted area (Fig. 2.5), which was maybe caused by removal of salt due to the growth of surrounding diapirs (Fig. 2.3 h). In the investigated area, we observed that strike-slip tectonics along the central fault zone (during Jurassic and Late Cretaceous) involved the basement, and is therefore also associated with uplift of Upper Permian horizons. On the other hand, we recognised that during non-strike-slip tectonics (Triassic/Jurassic extension, Late Cretaceous thrusting) Zechstein salt and Middle Keuper salt acted as detachment levels in which fault systems sole out, but basement faults have not been involved during this deformation. Decoupling even led to different deformation styles in the same area, as it is shown in the western part of the central fault zone: thrusting of Mesozoic sediments (imbricate thrusts) occurred contemporaneously with oblique thrusting (positive flower structure) of Upper Permian sediments during the Late Cretaceous.

We assume that the present-day location of salt structures in the working area is not necessarily significant for assumptions of coupling or decoupling between cover and basement in former times, because it depends primarily on salt migration through time, and the deformation style. However, the timing of salt migration and faulting, and the present-day location of salt walls and fault zones, refer to an interaction between faulting and salt movement, and might be caused either by fault-induced salt migration, or by salt-induced faulting, or by a combination of both. Salt-induced faulting would produce only localised structures above the salt, but not underneath. Fault-induced salt migration would produce more elongated salt structures, directly located along the fault zones. In our working area we observed a combination of salt diapirs (development: Keuper to Cenozoic) and salt walls (development: only during Late Cretaceous). Mesozoic faulting localised not only above the salt, but also underneath the salt, involving the basement. Therefore, we assume that the fault- and salt-pattern observed in our study area have been caused by a combination of both, fault-induced salt migration, and salt-induced faulting. Salt migration and faulting initiated contemporaneously during (a) Keuper/Jurassic: transtensional faulting

DOI: 10.2312/GFZ.b103-07087

within the basement triggered salt migration, which initiated local N-S extension within the cover, and (b) Late Cretaceous: salt wall development was strongly related with deformation along the central fault zone. Salt can move easily along tectonically weak zones; at the same time faulting is much easier along salt walls (e.g. Jackson & Vendeville, 1994; Stewart & Coward, 1995; Davison *et al.,* 1996; Rowan *et al.,* 1999).

This study supplements other regional studies in the NW German Basin (e.g. Brink, 1986, 1991; Scheck *et al.,* 2003; Mazur & Scheck-Wenderoth, 2005), which also suggest that the development of salt structures seems to be closely related to strike-slip or normal faulting. By analysing regional 3D structural models, Scheck *et al.* (2003) demonstrate that major changes in salt dynamics in the North German Basin are coupled with changes in the regional stress field. Tectonic activity initiated salt movement, which led to salt rise within fault zones. Periods of tectonic quiescence are characterised by a removal of salt out of fault zones. We assume that the development of the LSB and the PB was mainly controlled by tectonic activity along the Aller-lineament, but the preferred occurrence of salt structures in this area was responsible for stress perturbations and strain partitioning. The differences in the kinematic regime between the area of the Aller-lineament and other areas of the Central European Basin System might be mainly caused by the occurrence and distribution of salt structures, the evolution of salt structures through time, as well as the scale the data have been investigated.

2.5.4. Comparison with other basins of the Southern Permian Basin

The LSB has been developed along the southern margin of the Southern Permian Basin (SPB), together with other basins like the Sole Pit, Broad Fourteens, West Netherlands, and Central Netherlands Basin. They show a similar evolution in terms of sedimentation and timing of deformation, and developed within the same superimposed regional stress field; but differences exist in the distribution and thickness of the Zechstein salt (e.g. Lockhorst, 1998; Ziegler *et al.*, 2001; de Jager, 2003; Scheck-Wenderoth & Lamarche, 2005). However, the evolution of salt plays an important role, as it strongly controls the deformation style, and defines coupling or decoupling between pre- and post-salt units, and therefore the involvement of inherited structures during later deformation.

During Late Cretaceous inversion, the Polish Basin for example showed coupling in its south-eastern part, whereas the north-western part is marked by decoupling (Lamarche *et al.,* 2002). The NE German Basin, located west of the Polish Basin, is also characterised by decoupling between pre- and post-Zechstein salt units (Scheck & Bayer, 1999; Kossow *et al.*, 2000). Hansen *et al.* (2007) studied the northern part of the NE German Basin (western Baltic Sea) and demonstrated a high salt thickness (up to 7500 m inside diapirs) and thin-skinned tectonics during Mesozoic deformation. Further west of the LSB de Jager (2003) compared basins in the western part of the SPB and illustrated that basins without Zechstein salt (e.g. southern part of the Broad Fourteens Basin, West Netherlands Basin, Sole Pit Basin) are coupled and deformed mainly by strike-slip faulting, whereas basins that contain a high salt thickness (e.g. northern part of the Broad Fourteens Basin) are decoupled and not deformed by strike-slip faulting, but show an acceleration of halokinesis and different deformation styles above and below the salt. Late Cretaceous inversion affected those basins without Zechstein salt mainly by dextral strike-slip faulting along NW-striking reactivated basement structures (de Jager, 2003 and references therein). In contrast, the LSB contains a higher salt thickness and therefore shows only a minor internal deformation during inversion, and reactivation of basement structures occurred mainly along the northern and southern basin borders (Betz *et al.,* 1987). The differences in deformation style between the several sub-basins of the SPB might be mainly caused by the occurrence and distribution of salt structures, defining coupling or decoupling between pre- and post-salt units, which subsequently trigger the reactivation of the different inherited structures.

2.6. Summary

(1) We determined the evolution of the study area, which includes E-W extension during Permian, N-S extension and E-W transtension during Late Triassic and Jurassic, regional subsidence of the Lower Saxony Basin during Late Jurassic/Early Cretaceous, E-W transpressional and N-S compressional inversion tectonics during Late Cretaceous/Early Tertiary, as well as subsidence and salt diapir rise.

(2) We interpret the central fault zone in the study area to be the Aller-lineament, the boundary between the Lower Saxony Basin (LSB) and Pompeckj Block (PB).

(3) We measured the horizontal displacement during extension and inversion within the sedimentary cover of the study area. The calculated minimum value of 2 km (during extension, and during inversion) underestimates actual deformation due to erosion of Jurassic sediments. The total horizontal displacement along the Aller-lineament, which involves both basement and cover, amounts to only a few km.

(4) The heterogeneity in distribution and timing of deformation in our study area is controlled by different reactivation of pre-existing faults depending on their orientation, and by salt distribution. These factors led to stress perturbations and therefore local strain partitioning: areas with higher salt thickness triggered a decoupling of the stress field between pre- and post-salt units. Therefore, we explain the different stress regimes between basement and cover, but also along strike of the Aller-lineament, with stress partitioning.

(5) We assume that the Lower Saxony Basin, and in particular the Aller-lineament plays a key role in that part of the Southern Permian Basin, as it might have acted as a barrier zone for extensional deformation triggered from the North Sea area in the north, and compressional deformation generated from the Alpine area in the south.

DOI: 10.2312/GFZ.b103-07087

3. Prediction of sub-seismic faults and fractures - integration of 3D seismic data, 3D retro-deformation, and well data on an example of deformation around an inverted fault

Abstract

In addition to seismically mapped fault structures, a large number of faults below the limit of seismic resolution contribute to sub-surface deformation. However, a correlation between large- and small-scale faults is difficult because of their strong variation in orientation. A workflow to analyse deformation over different scales is described here. Based on the combination of seismic interpretation, coherency analysis, geostatistical analysis, kinematic modelling, and well data analysis, we constrained the density and orientation of sub-seismic faults, and made predictions about reactivation and opening of fractures.

We interpreted faults in seismic and coherency volumes at scales between several km and a few tens of meters. 3D retro-deformation was performed on a detailed interpreted 3D structural model to simulate strain in the hanging wall at the time of faulting, at a scale below seismic resolution. The modelling results show that (1) considerable strain is observed more than 1 km away from the fault trace, and (2) deformation around the fault causes strain variations, depending on the fault morphology. This strain variation is responsible for the heterogeneous sub-seismic fracture distribution observed in wells. We linked the fracture density from well data with the modelled strain magnitude, and used the strain magnitude as a proxy for fracture density. With this method we can predict the relative density of small-scale fractures in areas without well data. Furthermore, knowing the orientation of the local strain axis we predict fault strike, and opening or reactivation of fractures during a particular deformation event.

3.1. Introduction

One of the most important questions that drives basin research is how deformation is accommodated, because it is very heterogeneous over time and space, and over a wide range of scales (e.g. Yielding et al., 1992; Gauthier and Lake, 1993; Pickering et al., 1996; Bonnet et al., 2001). Faulting plays an important role in the deformation of sedimentary basins. Large-scale sub-surface faulting is typically identified by the interpretation of 2D or 3D seismic data, whereas small-scale sub-surface faulting is identified by spatially-isolated 1D well data (e.g. McLeod et al., 2000; Meyer et al., 2002; Walsh et al., 2002; and Figure 3.1). Faulting at medium-scale (displacement between c. 30 m and a few dm) can usually neither be recognized on seismic data nor well data (e.g. Gauthier and Lake, 1993; Yielding et al., 1996). However, faulting at this medium-scale plays an important role in reservoirs: large individual reservoirs can be disrupted by faults that enhance fluid flow, or produce compartmentalized deposits due to cementation of fractures (e.g. Ferrill et al., 2000; Mauthe, 2003; Parnell et al., 2004). Displacement along faults can change the juxtaposition between sand and clay layers, for example, which can lead to clay smearing on fault surfaces and, therefore, to a reduction in fluid flow (e.g. Stewart, 2001). In contrast, fracture networks may act as conduits for diagenetic fluids, or even as reservoirs, like in the mudstones of the Bristol Channel (Cosgrove, 2001), or in the Devonian cherts of Parkland field, Canada (Packard et al., 2001). These examples show that faulting below the limit of seismic resolution (hereafter referred to as sub-seismic) can strongly control fluid flow, and therefore has a significant importance in hydrocarbon reservoirs, diagenetic ore deposits, and geothermal energy reservoirs.

DOI: 10.2312/GFZ.b103-07087

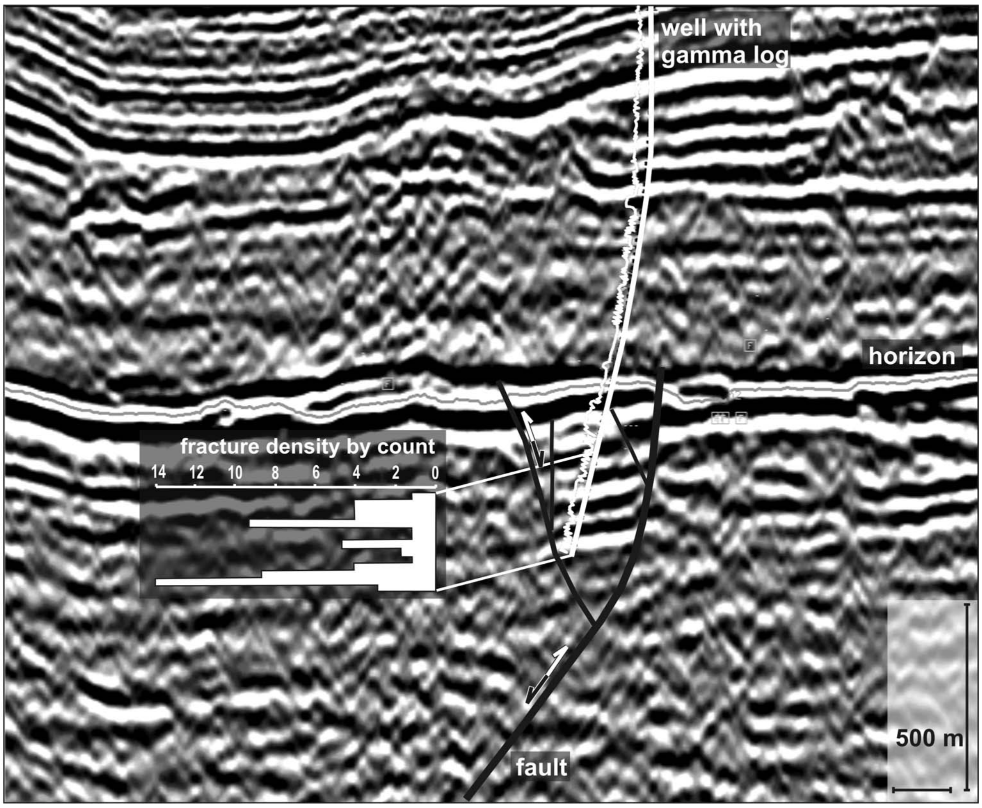

Figure 3.1: Information from seismic data set, from large-scale (seismic line with interpreted fault and horizon) to small-scale (well within hanging wall and corresponding gamma log, and fracture distribution from FMI data).

The key to understand the distribution and interaction of small- and medium-scale fractures lies in the evolution and kinematics of large-scale structures, because the dominant strain component is commonly accommodated by large-scale faults with offsets of several tens or hundreds of meters (e.g. Scholz and Cowie, 1990; Pickering et al., 1996; Ackermann and Schlische, 1997; Bonnet et al., 2001). Around these faults, smaller faults develop (for normal or inverted faults predominantly in the hanging wall, for thrust faults in both hanging wall and footwall), which accommodate minor strain with respect to the major fault. Nonetheless, the total amount of this sub-seismic strain can locally reach up to 50 % (e.g. Walsh et al., 1996; Schwarzer et al., 2003; Tanner et al., 2007, personal communication), but the precise position, orientation, or density variation of sub-seismic faults is difficult to estimate. However, knowing the 3D shape and the kinematic evolution of large-scale faults and their interaction, the surrounding fracture-network can be predicted.

The challenge is to develop a workflow that bridges the gap between large-scale 3D seismic data and small-scale 1D well data in order to make predictions about sub-seismic deformation in areas without well data (Figure 3.1). To identify the sub-seismic deformation, its magnitude and spatial distribution within 3D seismic data, and to make assumptions about fractures which were opened or reactivated during a particular deformation phase, we developed a workflow combining different methods of seismic data analyses, recently introduced by Krawczyk et al. (2006). For this purpose, we combine 3D kinematic modelling (retro-deformation) of horizons along large-scale faults, geostatistic analysis of medium-scale faults, and finally correlation of these results with small-scale fractures identified from well data. In a joint project the results discussed here are tied with the results from Trappe et al. (2007), who investigated the potential of geostatistical tools for fracture prediction.

3.2. Data base and reservoir characterisation

We analysed a pre-stack, depth-migrated 3D reflection seismic data set, provided by RWE Dea AG. The line spacing of the seismic volume is 25 m, with 25 m CDP binning and c. 30 m vertical resolution. The seismic data was interpreted with the Schlumberger software GeoFrame. Well data include information about fracture orientation from FMI data (Formation micro image), lithological information from core data and reports, as well as log data for correlation with the seismics (Figure 3.1).

Our study area is located within the NW German Basin. A detailed tectonic characterisation of the area can be found in Lohr et al. (2007). In our workflow, we concentrate on an area within a Rotliegend (Lower Permian) sandstone gas reservoir. The Permian is characterized by syn-sedimentary grabens and halfgrabens, in which well data documented mainly sandstone, but also fanglomerates and volcanic rocks. The Rotliegend sandstone reservoir is strongly fractured. These fractures cause problems in reservoir exploration and drilling prospects due to their cementation and the associated decrease in fluid flow and compartmentalization of the reservoir. Because of company confidentiality we avoid giving more detailed information of exact data location or orientation. Instead, assume that all maps, rose diagrams, and Schmidt nets shown here are orientated with North at the top.

3.3. Workflow

The suggested workflow includes several analyses of both seismic and well data on different scales (Figure 3.2). The four main parts of the workflow are presented in the four sub-chapters below.

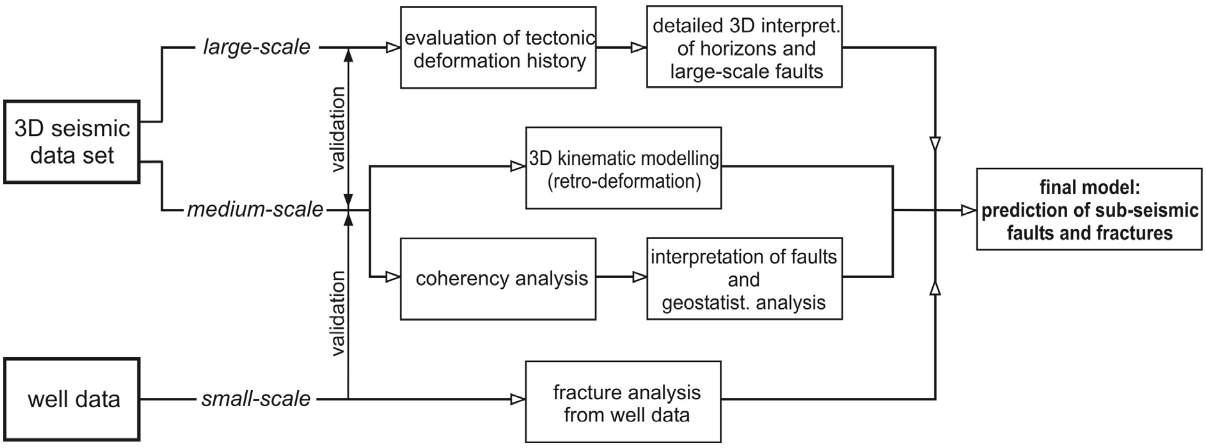

Figure 3.2: Flow diagram illustrating the developed workflow.

3.3.1 Tectonic deformation history

The first step in the workflow is the general investigation of the study area in terms of its geological evolution, and the comparison of these results with the regional evolution based on reflection seismic data. Here, the regional evolution encompasses sedimentation, faulting, and diapirism from Carboniferous to Tertiary times. On a regional scale, this is discussed in Lohr et al. (2007).

DOI: 10.2312/GFZ.b103-07087

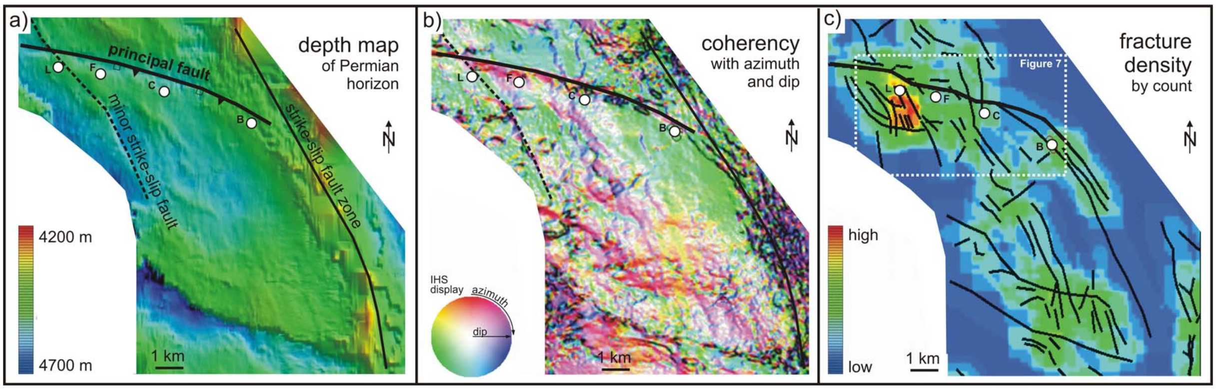

Figure 3.3: Top Rotliegend horizon in map view showing different attributes: (a) depth, (b) coherency with IHS display (intensity, hue, saturation) of dip and azimuth, and (c) interpreted faults with color-coded fracture density by count. The analyzed fault is indicated as "principal fault". The white circles label four wells (B, C, F, and L) penetrating the hanging wall.

The chosen example for the detailed study presented here consists of a 6 km long fault (principal fault in Figure 3.3) with a strongly deformed hanging wall (Figures 3.1, 3.3a). This Permian age normal fault was reactivated and inverted during the Cretaceous. Oblique to the principal fault, a strike-slip fault zone occurs (Figure 3.3a), that was initiated prior to Permian normal faulting and reactivated several times until the Tertiary (Lohr et al., 2007). Parallel to this strike-slip fault zone a subordinate strike-slip fault occurs that interacted with the principal fault (Figure 3.3a). We have chosen this example despite of the superposition of several deformation events, because here four wells have been drilled in the hanging wall of this relatively small structure, given the unique possibility to document the heterogeneous distribution of small-scale deformation.

The principal fault is slightly listric and is located at a depth between 4400 m (upper limit defined by end of deformation) and 5800 m (lower limit defined by seismic resolution). The principal fault, as well as the hanging wall and footwall were interpreted in 3D in detail (75 m grid for fault interpretation, 25 m grid for horizon interpretation). The triangulation of all surfaces was carried out using GoCad (GOCAD Consortium). The Midland Valley software 3Dmove was used to analyse the fault morphology, and to define kinematic parameters for the subsequent 3D kinematic modelling (retro-deformation).

3.3.2 Coherency analysis and geostatistical fault prediction

At a medium-scale, we analysed faults at the limit of seismic resolution using advanced coherency analysis. Two new coherency algorithms, "Structural Entropy" and "Shaded Relief" (Trappe et al., 2007), were developed to enhance subtle lineaments within 3D seismic data. The use of the advanced coherency algorithms significantly improved the quality of the attributes dip and azimuth, and therefore even subtle faults could be interpreted in detail (maximum resolution is about 9 m at that depth on horizon slices). To combine the medium-scale fault interpretation picked from the coherency volume, and the small-scale fracture analysis from well data, we performed a geostatistical fault analysis in order to test the reliability of both analyses. These methods and the interpretation results are described and discussed in Trappe et al. (2007).

Figure 3.3 shows the analysed horizon (Top Rotliegend) in map view as depth map (a), coherency map (b), and fracture density map (c) with fault pattern interpreted from (b) and seismic cross-sections. The color-coded fracture density is calculated by count. The resulting map demonstrates that fracture density is very heterogeneous, and that the highest fracture density occurs in the area close to well L (Figure 3.3).

DOI: 10.2312/GFZ.b103-07087

3.3.3 3D kinematic modelling (retro-deformation)

Figure 3.4 shows a 3D model of the analysed fault, the hanging wall, the footwall, and the position of four wells. Volumetric retro-deformation allows the backward movement of the hanging wall along the fault to a previous stage. In this manner, the hanging wall volume was retro-deformed along the 6 km long principal fault, and the resulting volumetric deformation of the hanging wall was used to predict the sub-seismic fractures occurring in this area. In our example, the inversion stage was retro-deformed by simulating extension (Figure 3.5). The calculation of hanging wall deformation during volumetric retro-deformation is based on the measurement of the translation of tetrahedrons within the hanging wall volume. This translation is strongly controlled by fault morphology. From the translation of tetrahedrons and the relative displacement of their nodes within the volume, 3Dmove calculates the strain tensor at each point of the deformed volume. Before discussing the results of volumetric deformation, we first introduce the parameters chosen for the modelling procedure, namely: the deformation algorithm, shear vector orientation, the amount of displacement, and the movement direction of the hanging wall.

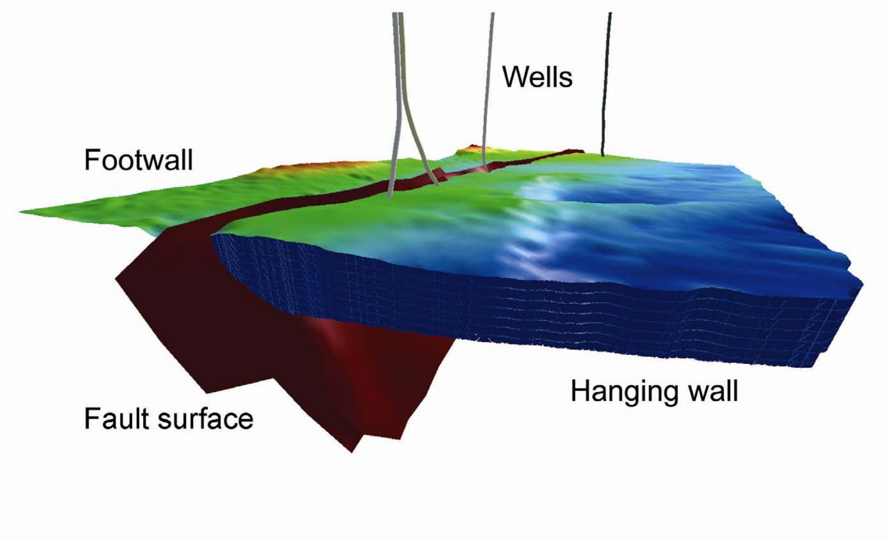

Figure 3.4: Present-day perspective view of the model illustrates the hanging wall volume, footwall, principal fault, and four wells. Hanging wall and footwall are color-coded by depth.

In 3Dmove, the "Inclined Shear" *deformation algorithm* was chosen. In contrast, other kinematic restoration algorithms in 3Dmove ("Flexural Slip" and "Fault Parallel Flow") use layer-parallel shear, suitable for simulation of contraction in fold and thrust belts. "Inclined shear" is used to model penetrative deformation resulting from movement over a fault plane, that occurs on a slip-system (within the hanging wall) oriented at an angle oblique to bedding (e.g. Gibbs, 1983; Suppe, 1983; Groshong, 1990; Withjack and Peterson, 1993). In the analysed seismic volume we observed antithetic faults within the hanging wall, which cut the bedding at an angle of c. 60°.

During retro-deformation the hanging wall moves along the fault. This movement is controlled by the *orientation of the shear vector*. An antithetic shear vector of 60° was used because of the presence of 60°-dipping antithetic faults within the seismic volume. These faults appear as discrete fault zones in the seismic volume, and can therefore be modelled as relatively stable large-scale shear zones.

The present-day observable separation of the footwall and hanging wall varies between 0 and 25 m along fault-strike. However, this amount does not represent the true displacement variation along fault-strike that occurred during inversion or extension, because of the superposition of both deformation events (Figure 3.5). For this reason, we did not incorporate this amount as a variable displacement in the deformation algorithm. Instead, we estimated from seismic data the *amount of displacement* that occurred during inversion to be about 100 m as a minimum value. The true amount of displacement cannot be measured more precisely since the amount of inversion was higher than the amount of extension, and since the analysed structure is relatively small to allow an identification of growth strata from the seismic data. However, an increase of displacement would lead to an increase of the strain magnitude, but for the modelling in this stage of the workflow only the relative magnitude of strain is important.

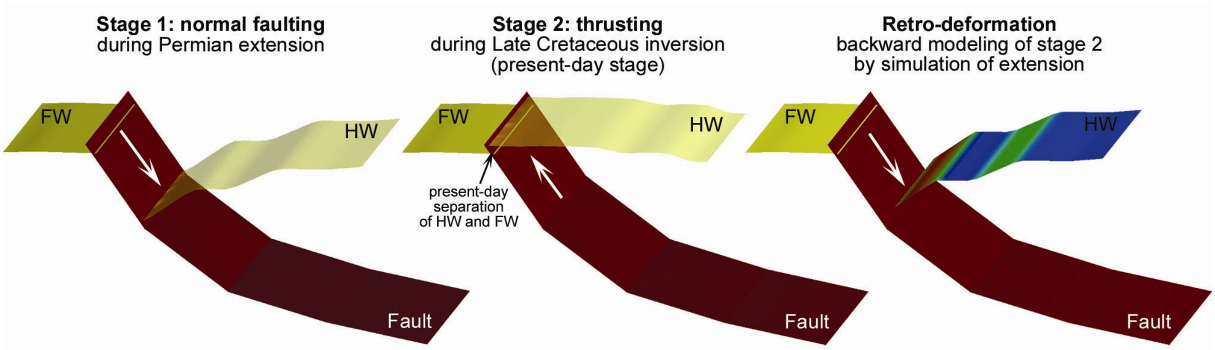

Figure 3.5: Schematic illustration of the method of retro-deformation, showing the two stages of deformation (extension, inversion). During retro-deformation the hanging wall is displaced downwards by simulation of extension. The white arrows indicate movement direction during the deformational stages. The color-coded hanging wall during retro-deformation indicates the strain of triangles (tetrahedrons in volumetric retro-deformation) within the deformed surface: red - high strain, green - medium strain, blue - low strain. FW - footwall, HW - hanging wall.

Movement direction was identified from fault morphology analysis by using attributes such as dip, azimuth, and cylindricity (Figure 3.6). These attributes highlight fault corrugations, which developed during fault-growth by segment linkage over time. The movement direction of the hanging wall is supposed to be parallel to the axis of these corrugations, which are perpendicular to fault strike in this example. Such corrugation-parallel movement requires least energy and therefore causes smallest strain within the hanging wall, rather than corrugation-oblique movement. Thus, the orientation of the fault corrugations can be used to define the movement direction on the fault (Needam et al., 1996).

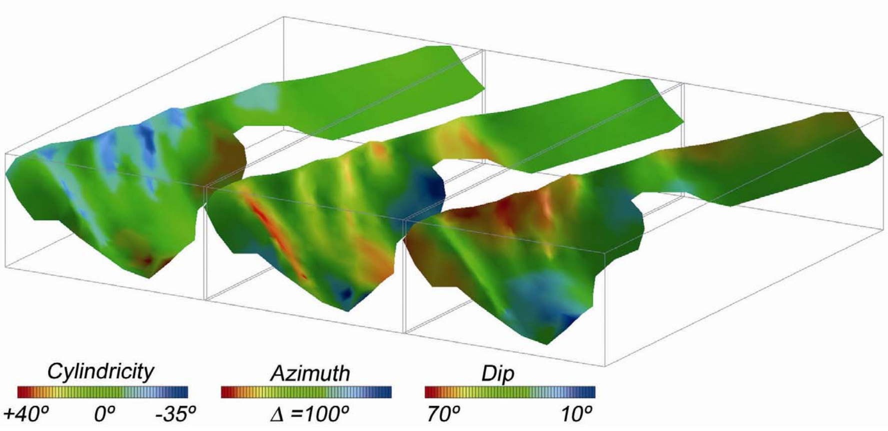

Figure 3.6: 3D view of the analyzed fault presenting three different attributes: dip, azimuth, and cylindricity. Fault length is 6 km, fault depth is max. 1.5 km. Dip and azimuth attributes show the dip and azimuth of each individual triangle of the fault-surface. Cylindrical analysis compares the orientation of the surface triangle normals with the orientation of the average cylindrical vector (parallel to surface-corrugations). A surface normal at 90° to the average cylindrical vector has a deviation attribute of zero. Deviations from this best-fit normal will have deviated attribute values above or below zero.

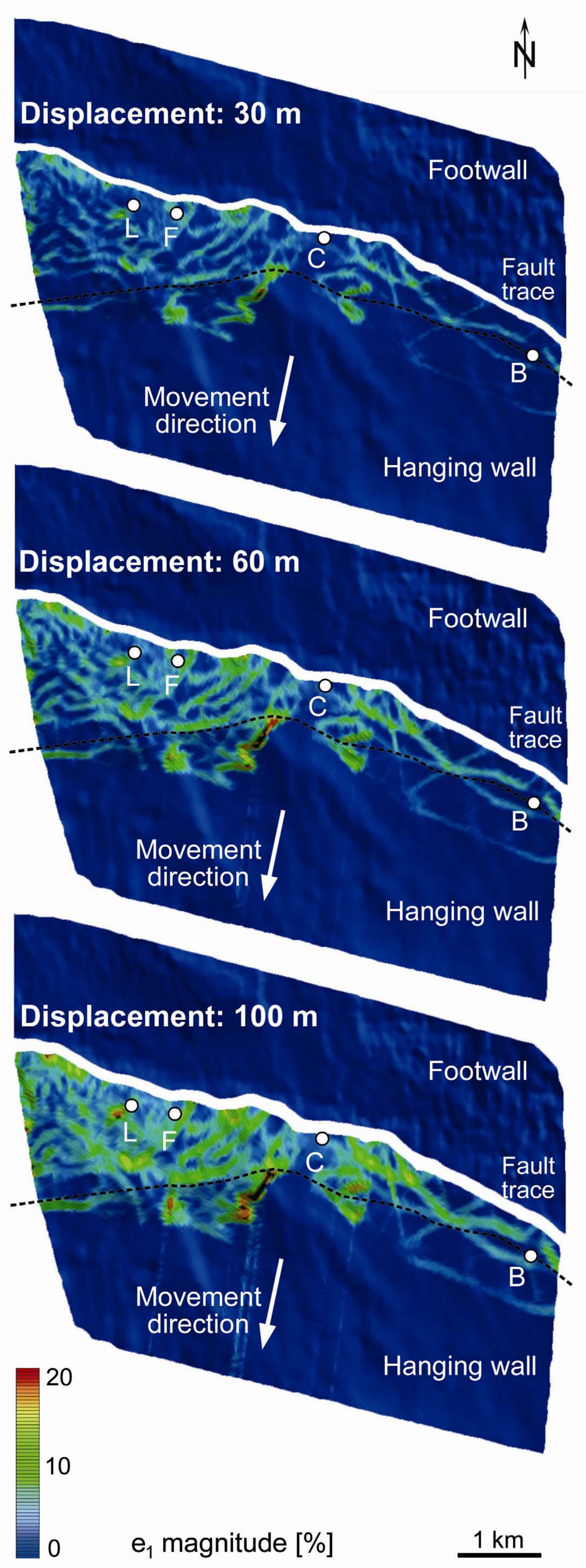

Figure 3.7: Results of 3D retro-deformation of model illustrated in Figure 4 are shown in map view after 30, 60, and 100 meter displacement. The magnitude of maximum strain (e_1) is colour-coded. Artefacts during modelling are related to the fault termination at depth. The dotted line marks the boundary between real modelling data (north) and artefacts (south).

The definition of the required input parameters (deformation algorithm, shear vector, displacement, movement direction) for the retro-deformation is well constrained by the seismic interpretation. Nevertheless, we tested the influence of slight variations of these parameters finding similar results during modelling. Larger variations in the shear vector (more than +/- 20°) and in movement direction (more than +/- 10°) led to an abnormally high deformation of the hanging wall, and to an increased number of artefacts even after a few meters of displacement. Also, the use of other deformation algorithms, such as "Flexural Slip" and "Fault Parallel Flow", induced odd strain results. The effect of the amount of displacement was relatively low, still showing plausible deformation results up to a displacement of 300 m.

For the modelling applied in this study, we choose the following parameters: the deformation algorithm "Inclined Shear", a 60° antithetic shear vector, 100 m displacement, and corrugation-parallel movement direction. Figure 3.7 shows the model in map view at different steps during retro-deformation. The colour-coded maximum magnitude of strain increases with increasing displacement and ranges from 0 % to 20 % after 100 m displacement. The strain magnitude shows a strong heterogeneous spatial distribution, in both along fault-strike and along displacement directions. The highest deformation is observed in the West, whereas less deformation occurred in the East. Hanging wall deformation affects areas in larger distances of up to 1300 m from the fault. The locations of high-strain zones are stable throughout the deformation. However, these localized zones become broader with increasing displacement. Deformation of the hanging wall is strongly controlled by fault-morphology: Zones of similar strain magnitude do not only develop parallel to fault-strike as it would be the case during deformation on a planar fault-surface, but they are also curved, following the fault corrugations (Figure 3.7). In some areas they are even nearly perpendicular to fault-strike. Furthermore, the highest strain areas are located especially close to the fault in areas of strong changes in fault-strike or fault-dip.

3.3.4 Fracture interpretation from well data

Four wells have been drilled through the hanging wall of the principal fault (Figure 3.3), allowing a deformation analysis also at the small-scale of a few cm. FMI data of these wells were measured and provided by RWE Dea AG; the orientation of fractures is shown in Figure 3.8. The fracture planes identified in the four wells represent all fractures within the approx. 250 m thick sandstone reservoir. Within the reservoir, the number of fractures increases strongly from East to West with n = 9 in well B, and n = 270 in well L. The orientation of the fracture planes differ in all wells. Well B is characterized by steeply-dipping NW-striking fractures, whereas well C shows moderate to steeply-dipping, mainly NE-striking fractures. In well F a NW-striking fracture set can be identified, with scatters of other fracture orientations. Two main sets can be recognized in well L (for well L only a rose diagram was provided): steeply-dipping NW-striking faults, and moderately dipping NE-striking faults. Unfortunately, from FMI data alone it was not possible to distinguish between open and closed fractures in these wells.

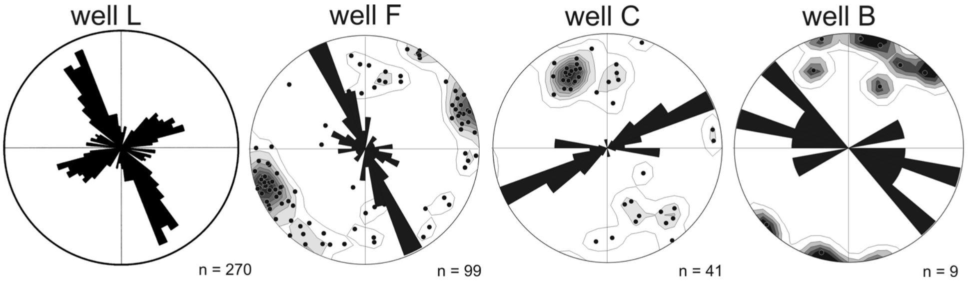

Figure 3.8: Fracture plots of FMI data, integrating both rose diagram (all wells; strike of fractures) and Schmidt net (well B, C, F; fractures planes are shown as pole points, plotted in equal-area stereonet, lower hemisphere projection). Well L: only rose-diagram is available. Number of fractures occurring within 250 m sandstone reservoir.

DOI: 10.2312/GFZ.b103-07087

3.4. Discussion

3.4.1 Interpretation of modelling results

The strain data resulting from modelling describe the complete strain tensor, yielding magnitude, dip, and azimuth of all three principal strain axes (e_1, e_2, e_3, in which $e_1 > e_2 > e_3$, Figure 3.9) at any point of the tetrahedron. From the strain eigenvector information, we extracted the orientation of the maximum strain axis (e_1) for all data and for the data near each of the four wells and plotted them on a Schmidt net (Figure 3.10).

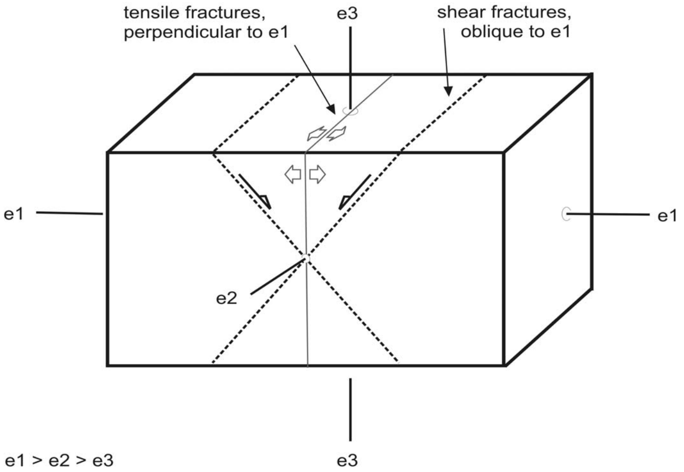

Figure 3.9: Sketch of the three strain axes ($e_1 > e_2 > e_3$) with possible orientation of tensile and shear fractures under extensional conditions, assuming isotropic rocks and non-rotational strain. Thereby, e_1 is used as an approximation for the maximum extension direction sigma 3, whereas e_3 is used as an approximation for the minimum extension direction sigma 1.

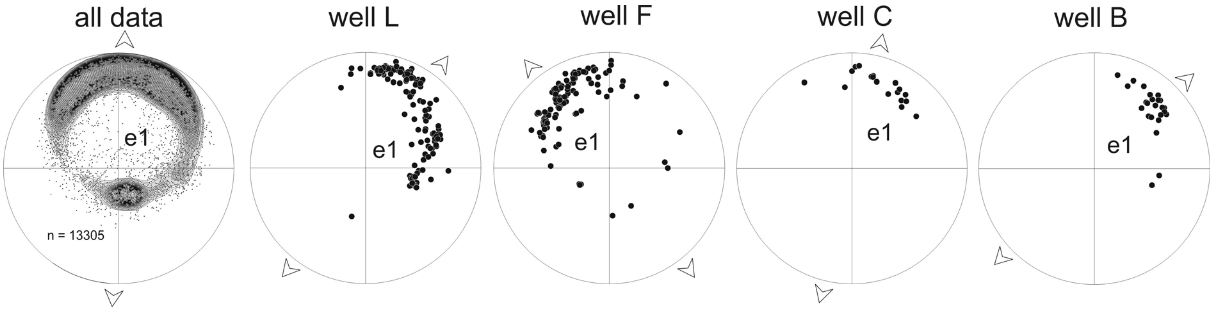

Figure 3.10: Maximum strain axis (e_1) around wells (extracted from a cylinder of about 400 m in diameter) derived from modelling shown in Figure 7. e_1 axes are shown as pole points, plotted in equal-area stereonet, lower hemisphere projection (Schmidt net). Arrows indicate the supposed max. horizontal extension direction derived from e_1 axes.

We assume that most of the strain in the study area occurs as brittle faulting. However, the real orientation of faults which developed during deformation cannot be completely reconstructed because of a lack of information about parameters influencing fracture behaviour, such as fluid pressure. The occurrence of fluids increases fluid pressure, which reduces the effective confining pressure and leads to shear or extension fractures, depending on the magnitude of differential stress (see Twiss and Moores, 1992). At small differential stresses, an increase in fluid pressure leads to extensional fractures, oriented perpendicular to e_1 (in this case e_1 represents the pole point to the fracture plane, Figure 3.9). At large differential stresses, an increase in fluid pressure leads to shear fractures of any orientation between 30° and 90° to the e_1 axis (Figure 3.9) depending on the amount of shear stress. Similar complexity may arise from fracture formation in an anisotropic rock or from reactivation of earlier fractures.

DOI: 10.2312/GFZ.b103-07087

The e_1 axis can be used as an approximation for the maximum extension direction during the modelled deformation. By knowing the orientation of the e_1 axis at any location, it is possible to predict a preferred reactivation and opening of existing fractures and faults at this location.

The e_1 axes near the wells were extracted from the whole modelled data set (extracted from a cylinder of about 400 m in diameter), and their orientation is shown in the Schmidt net (Figure 3.10). The orientation of the e_1 axes of the whole data set is also given. The majority of the summarized axes plunges towards the N, with a variation from NW to NE, equivalent to fracture planes striking parallel to the principal fault plane. This variation is caused by local differences in strike due to the undulation of the fault surface. Another smaller cluster of e1 axes shows the same strike of fractures, but dips in the opposite direction, and therefore may represent the conjugate part of the main fracture set. The orientation of the axes varies strongly between the wells. Wells B, C, and L are characterized by mainly NE plunging e1 axes, whereas the e1 axes of well F plunge towards the NW. For the modelled deformation the maximum horizontal extension direction was N-S, but local extension varies around 90°, from NW-SE to NE-SW (Figure 3.10). Since retro-deformation is the reverse of forward-deformation, the local maximum horizontal extension direction for retro-deformation is equivalent to the local maximum horizontal compression direction for forward-deformation.

3.4.2 Comparison between coherency, modelling, and well data

The comparison of FMI, modelling, and coherency data is shown in Figure 3.11. Here, fractures from FMI data are compared with faults from the interpretation of coherency data and fault zones (corresponding to high-strain areas) derived from tectonic modelling. The rose diagrams of each well show the strike of all fractures identified from FMI data, as well as the local maximum horizontal compression direction estimated from the orientation of the modelled e1 axes (c.f. Figure 3.10). Of all fracture data shown in Figure 3.10, the red- and blue-coloured once are those that correspond in orientation to faults or fault zones that have been identified from coherency analysis and modelling respectively. Both those predicted fault patterns match in some parts, especially in areas where they are sub-parallel to the principal fault (Figure 3.11); however in most other areas the fault patterns do not match. This is mainly caused by the different scales the faults have been interpreted/modelled, and the different methods that have been used. While fault interpretation occupies all deformation events in the coherency data, the tectonic modelling considers only one deformation event.

Around *well L* the NW-striking fractures seen in the rose-diagram have been recognized by coherency analysis, whereas the NE-striking fractures have been recognized by modelling (Figure 3.11). The NE-striking fractures are oriented nearly parallel to the proposed maximum horizontal compression direction, and are therefore appropriate to have opened during inversion.

The NW-striking fractures around *well F* have been identified with coherency analysis, but the NE-striking fractures identified from modelling are only of minor presence in the well data. The local compression direction is parallel to the NW-striking fractures, so that these have possibly opened during inversion.

The strike of fractures in *well C* is mainly NE, but these fractures could be recognized neither by coherency analysis nor by modelling. However, a minor WNW-striking fracture set observable in well C has been recognized by modelling. Another fracture set recognized by coherency analysis could not be confirmed by the well data. The proposed orientation of compression direction during inversion is about 50° to the strike of fractures, and therefore does not refer to a likely opening of existing fractures.

DOI: 10.2312/GFZ.b103-07087

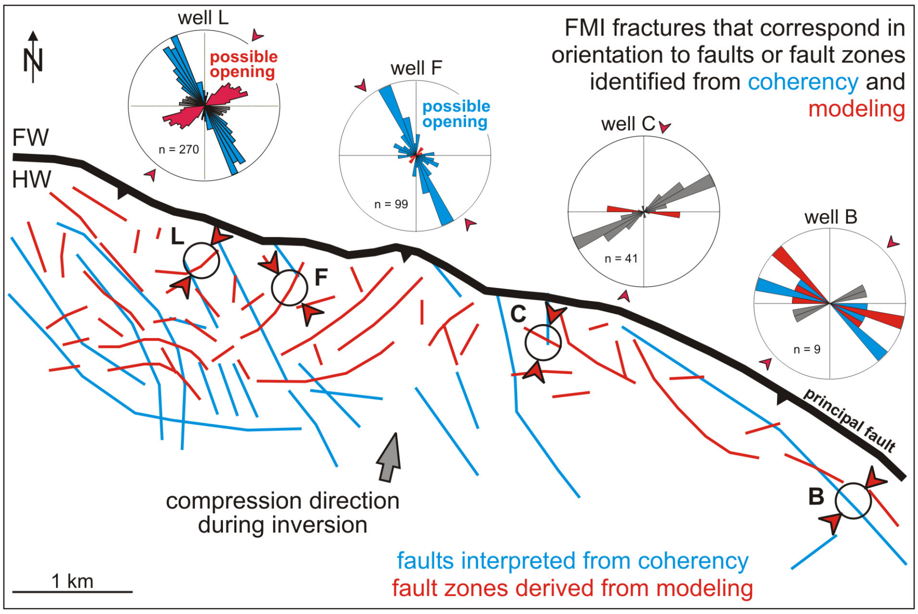

Figure 3.11: Map shows the principal fault with hanging wall deformation: red-colored structures are fault zones corresponding to high-strain areas that have been derived from modelling (Fig. 3.7); blue-coloured structures are faults that have been interpreted by coherency analysis (Fig. 3.3). Fracture plots show all FMI data of the four wells. In colour are fractures that have been identified also by modelling (red) or coherency analysis (blue). Small red arrows around plots and in the strain map around well locations demonstrate the local stress deviations derived from modelling, whereas the large grey arrow marks the superimposed maximum horizontal compression direction active during inversion. FW - footwall, HW - hanging wall.

Around *well B*, we detected NW-striking faults by both coherency analysis and modelling. This orientation corresponds to fractures detected in well data. A NE-striking fracture set can be noticed only in well data; however, this fracture set consists of only two fractures and is thus underrepresented. The orientation of the NE-striking fracture set in well B is not appropriate to have opened during inversion, as it has an angle of about 70° to the maximum horizontal compression direction (Figure 3.11).

Most of the fracture orientations measured in the analysed wells have been identified either with coherency analysis (wells L, F) or modelling (wells L, F, C), or with both (well B). Well C is the only well, in which the major fracture set could not be recognized with any of the two methods (Figure 3.11). In general, the faults that have been identified by modelling are those, which belong to the inversion event. Faults that have been identified by coherency are those, which belong to any of the three deformation events (extension, inversion, strike-slip faulting). Since the majority of former extensional faults have been reactivated during inversion, we distinguish only between dip-slip faulting (extension and inversion) and strike-slip faulting.

We interpret the fractures observed around well B to belong to the extension/inversion deformation. The fractures observed around wells L and F belong to the extension/inversion deformation when they were recognized by modelling (NE-striking structures), and to the strike-slip deformation when recognized by coherency analysis (NW-striking structures). In this area (wells F, L) the extension/inversion event has not been detected by coherency interpretation, possibly because the strike-slip faults are dominant and superimpose the others. In the FMI data, the predicted NE-striking extension/inversion structures are underrepresented, which is caused by either the incomplete detection of these fractures by the FMI method, or by an inaccuracy in modelling (e.g. incorrect fault surface interpretation due to superposition of strike-slip faults in

DOI: 10.2312/GFZ.b103-07087

this area). A possible explanation for the missing detection of NE-striking faults around well C by coherency analysis and modelling may be that these structures have probably initiated during extension, but have not been reactivated during inversion. Alternatively, they are below the resolution of coherency analysis.

Deformation during inversion along the principal fault can lead to reactivation and re-opening of pre-existing faults (normal faults, strike-slip faults), especially in areas where the orientation of the local stress field is suitable (Figure 3.11). The here proposed opening of fractures (in wells L and F) refers only to the modelled deformation event (inversion). Due to the subsequent influence of strike-slip faulting, the predicted opening of fractures is not necessarily a present-day prediction. The example studied here is complicated because of the superposition of two different fault patterns during three deformation events, which led to an accumulation of fracture density in the area of the wells F and especially L, because here strike-slip faulting is most prominent.

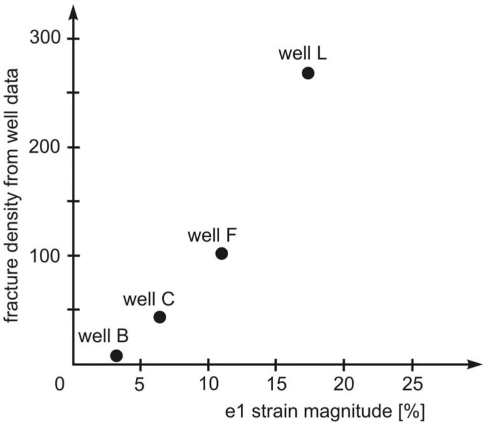

Figure 3.12: Diagram showing the fracture density of well data against e_1 strain magnitude derived from modelling. For discussion see text.

With respect to the modelled deformation it is possible to estimate the fracture density in the study area. By assuming that the fracture density increases with increasing strain magnitude, we can link the fracture density from FMI data with the strain magnitude from modelling for the same area, and use the strain magnitude as a proxy for fracture density at any given region within the modelled area. The diagram (Figure 3.12) shows the fracture density of all wells plotted against the maximum strain magnitude. The relation between both parameters demonstrates a positive trend, but a quantitative correlation cannot be done, because the fracture development also depends on material parameters such as rheology, porosity, fluids, or anisotropy, and on their spatial variation. Additionally, due to the influence of strike-slip faulting in the area of well F, and especially well L, the fracture density is slightly increased because it was not included in the modelling. However, even with these limiting parameters, there is a positive trend between fracture density and strain magnitude, which can therefore be used as a first qualitative estimation for fracture density within the study area.

3.4.3 Applications

Our results show strain variations along the principal fault, because strain is related to the fault shape. When moving along the fault, the hanging wall undergo penetrative deformation caused by the fault morphology, which results in local strain variations. Local maximum strain axes differ by as much as 90°. The strike variations of secondary faults are the result of these strain variations, which are caused by stress perturbations around the principal fault. These variations do not need to be explained by other tectonic events or reactivated older structures. Strain variations are important when using data such as kinematic indicators and fracture orientation

DOI: 10.2312/GFZ.b103-07087

from field data, to estimate the regional stress field. These local data can differ strongly, and therefore do not necessarily represent the superimposed regional stress field.

With the proposed workflow, combining different methods at different scales (see also Krawczyk et al., 2006), we are able to estimate the fracture density and orientation in future prospects, and to make assumptions about fractures, which have been opened or reactivated during a particular deformation event. By knowing the position of high-strain zones predicted by modelling, it is also possible to assess fault connectivity and fluid flow. These qualitative strategies result in an improved evaluation of the reservoir quality. However, this workflow is particularly appropriate for reservoirs which are fracture-controlled, and where the fractures need to be identified, either in case of open fracture networks, which enhance fluid flow, or when cemented fractures reduce fluid circulation.

The workflow does not consider heterogeneous sedimentology or variable diagenetic processes, as it is the case in many reservoirs. These parameters need to be considered in the future as they interact with each other and play an important role for reservoir characterization. Other limitations of this study are given by the multiphase tectonic history, including extension, inversion, and in addition strike-slip faulting, which complicates the modelling results. Modelling of a structure which underwent only one deformation event would result in a more precise comparison of the fault pattern between coherency and modelling data, and less ambiguous results in terms of density and orientation of fractures, as well as in opening/closure predictions. However, the advantage of having four wells along a relatively small structure makes the working area useful for this kind of analysis. Therefore, we suggest that the workflow introduced here is a helpful tool for understanding sub-seismic deformation. It can be used as an additional reservoir modelling tool for the prediction of small-scale faults and fractures (in particular their orientation, density, and connectivity), which is important for identifying compartmentalisation and fracture networks, and finally contribute to improving fluid flow simulations and well placement.

3.5. Conclusions

The heterogeneous fracture pattern observed in well data cannot be explained by large-scale seismic interpretations alone. Resolution and identification of small-scale fractures and faults is possible and feasible with the combined method of detailed coherency analysis and 3D retro-deformation. To get the most information out of the seismic data, we compared the modelling results with detailed fault interpretations on attribute data from coherency horizon slices, and with fracture orientations from well data. Despite the modelling limitations in terms of spatial variation of sedimentological features, rheological parameters, and variable diagenetic processes, the comparison of modelling and coherency results with well data reveal a correlation, and provide an explanation for the disparate fracture pattern by comparing well data and seismic data directly.

The modelling is based on a clear definition of a major large-scale fault in 3D and the temporal and kinematic understanding of its deformation. Our results demonstrate that deformation around a fault causes strain variations depending on the fault morphology. Strain variations around a larger fault result in differences in fracture orientation at a smaller scale. The angle between the regional and the local strain axis can differ up to 90°. The identification of strain variations over several scales helps to predict the orientation and relative density of fractures in areas without well data, and to assess opening or reactivation of fractures during deformation.

Our results show that these methods (3D retro-deformation, coherency analysis) integrated in the suggested workflow, are a powerful tool that bridges the gap between large-scale 3D seismic data and small-scale 1D well data for prediction of sub-seismic deformation.

4. Evolution of a fault-surface from 3D attribute analysis and displacement measurements

Abstract

A large fault-surface evolves by the growth and coalescence of numerous segments through time, which results in a strong undulation of the principal fault-surface on different scales. We interpreted a strongly segmented, approx. 13 km long fault in detail using 3D seismic data, and studied the fault-morphology in terms of fault-linkage, using attributes such as curvature, azimuth, and dip. Displacement profiles of two horizons have been measured in order to analyse the slip-throw-heave relation, and to quantify their variation and their dependence on the fault-morphology. The displacement profiles are triangular to half-elliptical in shape, rather than elliptical. This is clearly visible in slip but less in heave or throw. Our results illustrate that throw or heave may not be representative for displacement measurements along a fault, because segmented and strongly undulated faults show a strong variation in slip, throw, and heave. Additionally, the often-used heave or throw values lead to a smoothing of the displacement curves, and cannot show triangular-shaped curves due to the under-representation of slip. Morphological analyses and slip distribution of large-scale faults is important for a better understanding of the heterogeneous distribution of earthquake data, and to improve seismic hazard assessments.

4.1. Introduction

Faults grow most effectively by the coalescence of several smaller faults, whereas tip propagation is of only minor importance (e.g. Peacock and Sanderson, 1991; Willemse, 1997; Cartwright at al., 1995). Due to this coalescence of numerous segments through time, a fault's shape can strongly undulate, and the stress perturbations during fault interaction and increasing displacement result in a heterogeneous distribution of fractures at a smaller scale. Large-scale active faults are zones of potential seismicity; and together with their small-scale fracture network they can act as fluid conduits or barriers. The 3D fault-shape, the linkage of a fault with other faults, and the distribution of slip on its surface are important for defining the positions of juxtaposed beds that control, for example, connectivity and permeability across faults. Consequently, for the characterisation of reservoirs, the analysis of fluid transport, the precise placement of wells, as well as for estimating the potential of earthquake generation, it is very important to have detailed information about the 3D shape of large-scale faults in the subsurface.

Undulation of a fault surface results in differences between the vertical component (throw), and the horizontal component (heave) of the displacement, with respect to slip, the real displacement on the fault. Data used for investigation of fault geometry and fault statistics are often 2D (field data, remote sensing, seismic lines). Even when 3D data are available, faults are often studied in 2D only (horizon interpretation or cross-sections of 3D seismic data). However, the shape of an isolated normal fault is more complex as shown in previous papers (e.g. Walsh and Watterson, 1989; Nicol et al., 1996; Needham et al., 1996; Walsh et al., 1999).

In carrying out fault analysis, fault growth evolution is generally inferred from the geometrical characteristics of differently sized faults in the same population, rather than from kinematic analyses of individual faults. Many authors use throw or heave as approximation for slip, to analyse fault-populations in terms of fault-propagation through time, length vs. displacement relationship, or displacement vs. cumulative frequency (e.g. McLeod et al., 2000; Meyer et al., 2002; Walsh et al., 2002; Nicol et al., 2005). Using throw or heave can be an approximation to slip in case of homogeneous lithology, low fault-segmentation, and smooth fault-surfaces. Calculation of throw and heave is also less time-consuming with respect to slip, especially for investigation of large faults, or fault-populations. However, as individual fault surfaces can undulate strongly, such simplified analyses might not always represent exact fault characteristics, which become more important for economic applications.

The high complexity of fault-growth in time and space requires a detailed analysis in 3D. On the basis of 3D seismic data we studied a c. 13 km long synsedimentary fault in detail, and analysed the fault-morphology and displacement distribution along the fault. We illustrate that the displacement pattern is very heterogeneous, which results in different shaped displacement curves (triangular, half-elliptical, or elliptical), depending on slip, throw, or heave. Additionally, throw or heave values may not be representative for the real kinematic displacement (slip) along the fault because of their strong variation due to fault segmentation.

4.2. Data Base and Methods

The study area is located in the NW German Basin, as part of the intracontinental Southern Permian Basin. In Central Europe, rifting and associated volcanism in the Permian occurred in a dextral transtensional stress regime (e.g. Ziegler, 1990) and produced mainly N-S striking normal faults, but also NW-trending dextral strike-slip faults (e.g. Betz et al., 1987; Ziegler, 1990; Kockel, 2002). This deformation event is well documented in our working area, expressed by grabens and halfgrabens containing Permian growth-strata (Lohr et al., 2007). Sandstone, fanglomerates, and volcanic rocks have been identified by well data.

We analysed a pre-stack depth-migrated 3D reflection seismic data set, provided by RWE Dea AG, Hamburg. The line spacing of the seismic volume is 25 m, with c. 30 m vertical resolution for the depth of the analysed fault. We concentrated our analysis on the detailed interpretation of one synsedimentary normal fault (c. 13 km length) and two horizons (h2 - Top Rotliegend, h1 - Base Rotliegend) (Fig. 4.1). The fault interpretation is based on detailed picking of every third seismic line (75 m interval) perpendicular to fault-strike, numerous lines oblique to fault-strike, and horizontal correlations on depth slices.

We interpreted the seismic data with the Schlumberger software GeoFrame. Triangulation of surfaces and fault attribute analyses were carried out with the software package GoCad (GOCAD Consortium). The Midland Valley software 3Dmove was used for displacement measurements.

After interpretation of the seismic data in terms of horizons and faults, we created a 3D fault-surface by using the GoCad triangulation method (homogeneous triangles, Fig. 4.2). Subsequently, we analysed the fault-topography by using the attributes dip, azimuth, and curvature. The real dip and azimuth are calculated from each triangle of the fault-surface. The Gaussian curvature at a given point is the product of the two principal maximum and minimum curvatures. By flattening the 3D triangular grid, positive curvature is defined by a gap forming between flattened triangles of a dome, whereas negative curvature is defined by an overlap forming between flattened triangles of a saddle or basin. Surfaces with a high Gaussian curvature like domes or saddles are non cylindrical, whereas cylindrical surfaces like elongated folds have a Gaussian curvature of zero (Lisle, 1994).

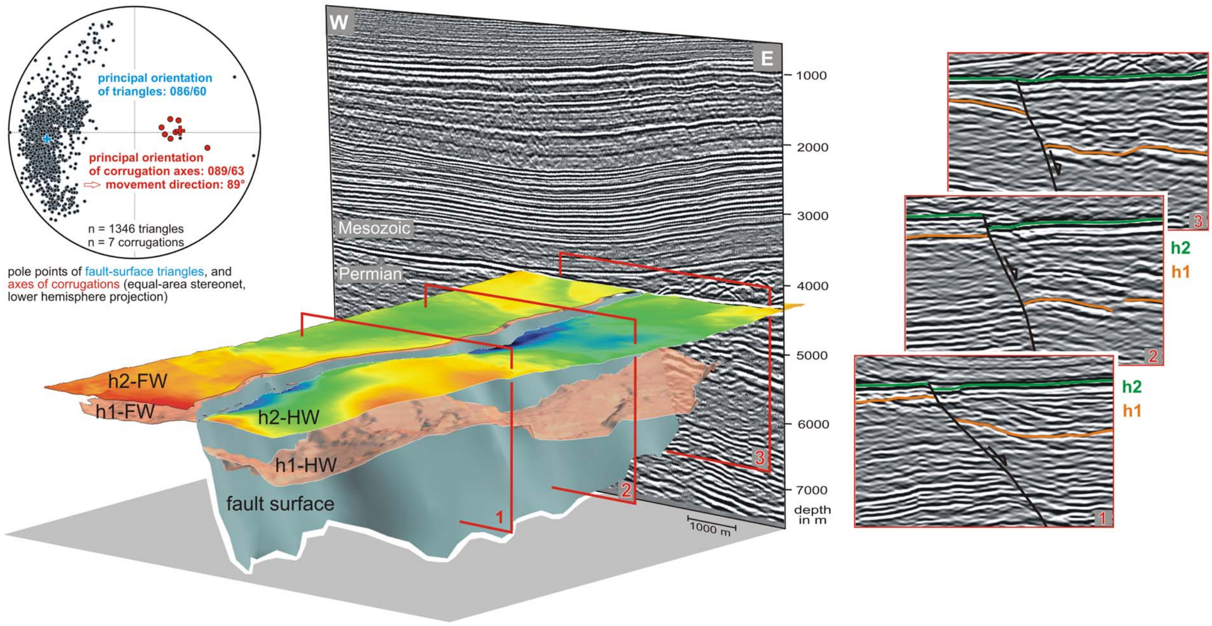

Figure 4.1: 3D view showing the structural model with the analysed fault, two horizons (h2 is Top Rotliegend, h1 is Base Rotliegend), and several seismic sections. FW = footwall, HW = hanging wall. H2 horizon is colour-coded with depth, from red to blue. View towards the NW. No vertical exaggeration. Left: Equal-area stereonet plot of poles, demonstrating the variation in dip and azimuth of each fault-triangle, and showing the axes of corrugations.

The attributes dip, azimuth, and curvature can highlight corrugations on the fault-surface. These attributes vary independently from the sections on which the fault has been interpreted, and are therefore a real feature rather than an artefact of the interpretation. These fault-corrugations are assumed to result from segment linkage (e.g. Walsh et al, 1999; McLeod et al., 2000; Mansfield and Cartwright, 2001; Marchal et al., 2003); they also indicate the movement direction as parallel to the axis of the corrugations, because this movement should require least energy and therefore smallest strain (Needham et al., 1996). Such corrugations have been observed also in the field (e.g. Wright and Turner, 2006; Sagy et al., 2007), and can be interpreted as fault-segments and fault-segment linkage zones. Striation measurements on these corrugations evidenced that corrugations are parallel to fault slip (Hancock and Barka, 1987). These corrugations observed in the field might be comparable to those observed in seismic data.

Thus, we used the here observed corrugations to define the movement direction on the fault. For the subsequent displacement measurements we calculated the amount of slip, heave and throw between the fault-surface and two Permian horizons: We mapped in detail the positions of the hanging wall and footwall cut-offs on the fault-surface (by directly "snapping" in the seismic interpretation software), defined the movement direction on the fault from the fault-corrugations (average movement direction is 89°, Fig. 4.1), and subsequently measured the displacements using the 3Dmove module "Allen Mapper". For this purpose, a vertical plane trending parallel to the movement direction was shifted step by step along the fault, rasterising the fault in numerous cross-sections (180 at h1, 250 at h2) and measuring the three displacement components.

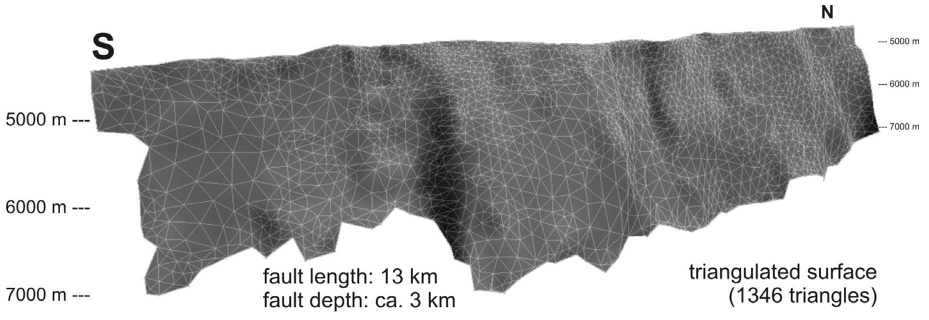

Figure 4.2: 3D view of the analysed fault-surface. View toward the NW. No vertical exaggeration.

4.3. Fault analysis

The studied fault strikes N-S and dips toward the east (Fig. 4.1). The fault is accessible almost in its complete extent in the seismic data set. The northern bound is limited by the margins of the seismic volume, whereas the southern bound is limited in interpretation by an overlaying Zechstein salt diapir. The fault is picked in a depth from 4200 m down to 7500 m (Fig. 4.2); the minimum value is defined by the blind upper fault tip because of the end of deformation, and the maximum value is given by the depth limit of the seismic volume (Fig. 4.1). The southernmost part of the investigated fault has been affected by later faulting. These areas were not involved in our analysis.

We studied the fault-morphology (Fig. 4.2) in two different ways: fault attribute analyses (dip, azimuth, curvature) highlight fault-corrugations in 3D at a larger scale of several kilometres. In contrast, displacement measurements can emphasise fault-corrugations only in 2D, but on a smaller scale of a few 100 metres to several kilometres. The results of both methods are appropriate to analyse the fault-morphology over a larger scale spectrum.

4.3.1. Large-scale fault analysis

Analysing the fault-morphology in 3D, we observed an undulation of the whole fault (Fig. 4.1, 4.2), expressed already by differences in orientation of the numerous fault-surface triangles.

The *dip* and *azimuth* maps and their histograms illustrate these differences (Fig. 4.3). The fault-dip varies between 35° and 80°. The average dip is 60°, but there are two main clusters with an average dip of 42° and 65° respectively. The average azimuth is 86°, but it varies between 40° and 165°. Comparing the dip and azimuth histograms (Fig. 4.3) with the dip-azimuth pole plot (Fig. 4.4) it is possible to assign fault regions to clusters of the pole plot. Density contour lines highlight several clusters (1 to 4), which correspond to several dip or azimuth clusters in the histogram, and to several regions in the fault attribute maps: cluster 1 corresponds to the majority of high-dip areas in the north and the south, cluster 2 is the low-dip area in the middle of the fault (overlap zone), cluster 3 represents the southernmost parts of both second-order faults (explained in chapter 4.3.2.), and cluster 4 is related to a possible transfer zone (explained in chapter 4.4.1.)

The Gaussian *curvature* was calculated for the whole fault surface. The undulation of the fault surface is not homogenous in both directions, but it is elongated sub-parallel to fault-dip, and the fault can therefore be described as a cylindrical surface. For that reason we used the minimum Gaussian curvature since it highlights well the corrugations on this surface (Fig. 4.3). Areas of positive curvature are convex to the hanging-wall, and represent areas where fault-linkage

DOI: 10.2312/GFZ.b103-07087

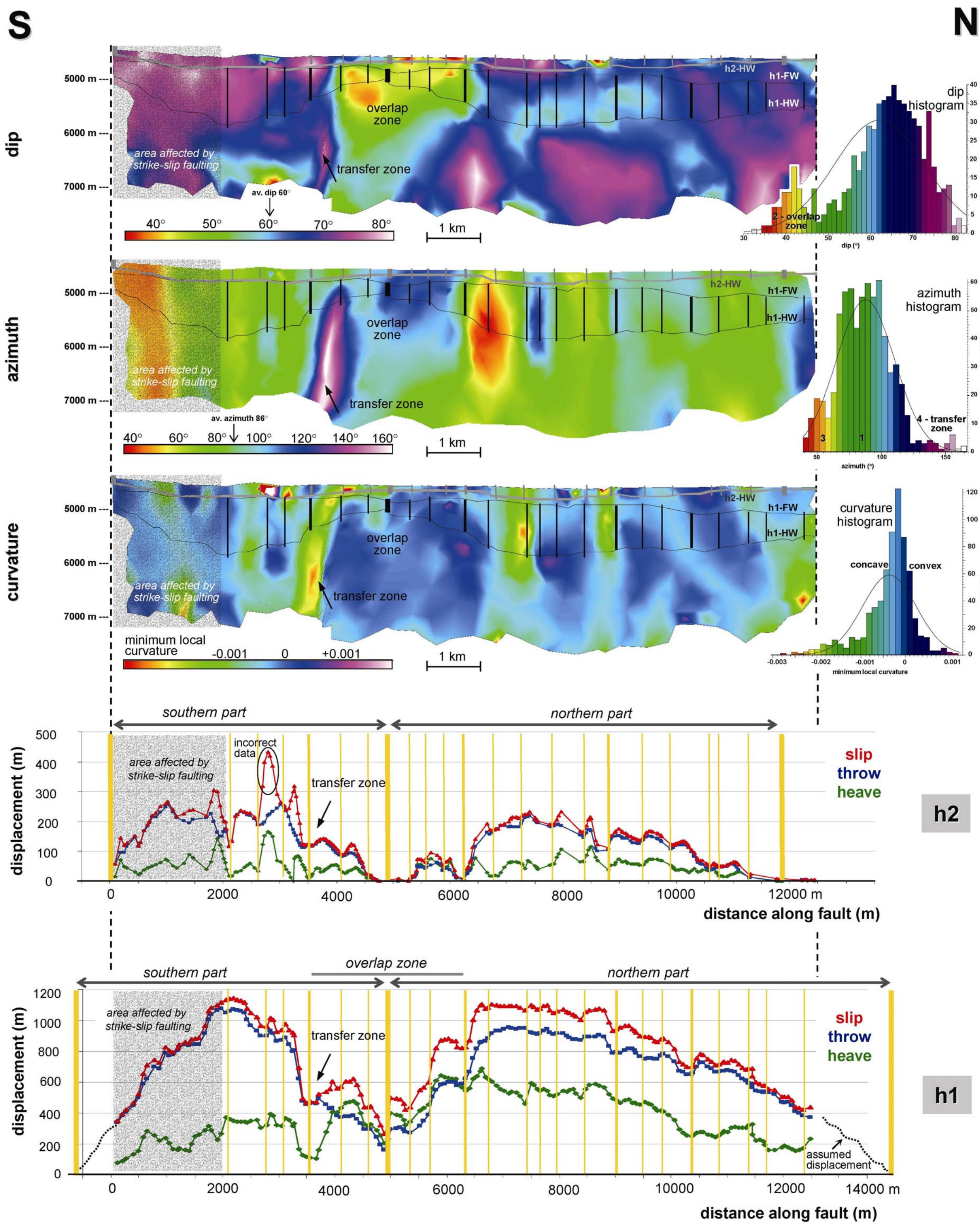

Figure 4.3: Top: Fault surface as colour-coded attribute maps showing dip, azimuth, and curvature, with corresponding histograms. View towards the fault-surface. Horizontal undulated lines are hanging wall and footwall cut-off of h1 (black lines, h1-HW and h1-FW), and hanging wall cut-off of h2 (grey line, h2-HW). Straight vertical lines between the cut-offs represent segment boundaries interpreted from the diagrams below. Numbers in histograms are related to the several clusters in Figure 4.4.
Below: Displacement-distance diagrams of the two Permian horizons (h1 - Base Rotliegend, h2 - Top Rotliegend) showing their separation along fault. Coloured lines indicate slip, throw, and heave. Variations of these lines reflect different fault-segments, which have been linked during fault-propagation, and finally produced one large fault-surface. Vertical yellow lines in the diagrams are fault-segment boundaries. Segments between thinner lines are smaller and older, whereas segments between thicker lines are larger and younger segments, which developed from linkage of the smaller ones. According to this subdivision four generations of fault-growth are identified.

occurred. Areas of negative curvature are concave to the hanging-wall, and represent the fault-segments itself (Fig. 4.3). In the histogram the average minimum local curvature is shifted to more negative values, which means that concave areas, and thus fault-segments, are overrepresented with respect to the convex ones (fault-linkage areas). That is reasonable as fault-segments are usually larger than zones of fault-linkage. The high curvature areas are not continuously visible along fault-depth. Comparing both, dip and curvature map, indicates that areas of high negative curvature are represented by higher dip, with respect to their surroundings, and that corrugations become narrower or die out towards the depth; some of them even at the same depth level of about 6000 m (Fig. 4.3).

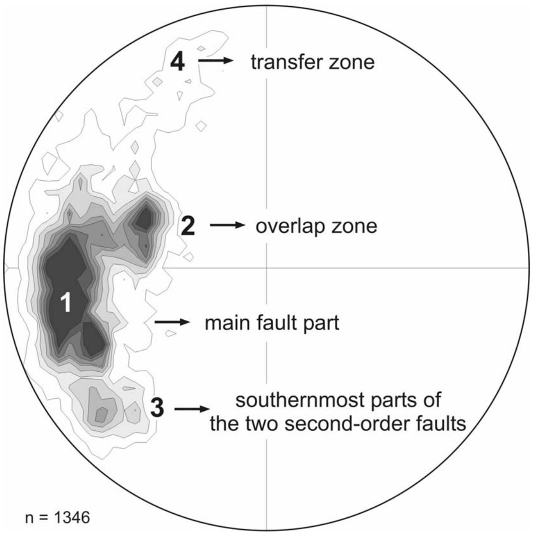

Figure 4.4: Equal-area stereonet plot with contour lines shows the distribution in orientation of fault-surface triangles derived from pole point plot in Figure 4.1. The four identified clusters have been correlated with areas on the fault-surface (compare with Figure 4.3).

Subordinate to these vertical corrugations we also note horizontal corrugations (Fig. 4.3, e.g. at ca. 5000 m depth level between 7000 and 10000 m distance along the fault). The hanging wall and footwall cut-off lines often match with areas of strong changes in dip or curvature, e.g.: the large horizontal corrugation visible as a low-dip area within the northern part of the fault is located between the hanging wall and footwall cut-offs of horizon h1; the hanging wall cut-off of this horizon often limits areas of high negative curvature at depth (Fig. 4.3, e.g. at 3600, 7400, 8900 m distance along the fault). The uppermost part of the fault surface (the area between hanging wall and footwall of horizon h2) is characterised by several small areas of changes in dip and curvature. This implies higher fault roughness in this upper part compared to deeper areas.

4.3.2. Small-scale fault analysis

For a more detailed investigation of fault-corrugations we measured the displacement of two horizons (h1 - Base Rotliegend, h2 - Top Rotliegend) along the fault. We analysed the amount of throw (vertical component of displacement), heave (horizontal component of displacement), as well as slip (real displacement) along the fault. The results are shown in the displacement-distance diagrams (Fig. 4.3) that illustrate the displacement-variation parallel to fault-strike. Profiles of both horizons are asymmetric, triangular to elliptical, convex-shaped curves. The displacement varies between 0 and 1200 m in h1, and between 0 and 300 m in h2. The curves show several sub-units with local minima and maxima, which point to different segments, that merged during fault growth. Maxima represent the core of the fault-segments because maximum displacement occurred close to the centre of the segments, whereas minima represent areas where fault-segments are linked because displacement is tapering off at the edges. Minima are also characterised by abrupt changes in displacement. Their positions are similar in the throw, heave,

DOI: 10.2312/GFZ.b103-07087

and slip curves, but the amounts of displacement are different between these curves, which results in a different slip-throw-heave relationship of each segment. Based on the distribution of minima and maxima, we identified four generations or orders of segments on both horizons (Fig. 4.3). These are younger with increasing fault-length, because of progressive fault-growth by segment linkage.

Fourth-order:	more than 23 small-scale segments (200 - 700 m length)
Third-order:	at least 6 medium-scale segments (1.5 - 3 km length)
Second-order:	2 large-scale segments (5 - 9 km length)
First-order:	1 large-scale final fault (c. 13 km length)

Vertical yellow lines in the diagrams separate these segments. Segments between thinner lines are smaller and older, whereas segments between thicker lines are larger and younger segments. The first-order fault has a length of approx. 15 km at horizon h1, and 12 km at horizon h2. The two second-order faults are well visible on the present-day morphology of the h2 hanging wall (Fig. 4.1). Here, the depth map shows two areas of increased depths (blue coloured), which indicate maximum subsidence and displacement along horizon h2 (fault-controlled depocentres). The area between both second-order faults appears as overlap zone, bounded by a transfer zone to the south (Figs. 4.2, 4.3). Third-order faults are in the scale of a few kilometres, and the numerous fourth-order faults with several hundred metres length are the smallest segments that could be identified by this method.

Areas of segment linkage identified from the displacement-distance diagrams match with areas of strong differences in dip, azimuth, or curvature, identified from fault-morphology analysis (Fig. 4.3). In the dip map the vertical lines often separate horizontal neighbours of varying dip. The colour bar of the azimuth map highlights especially areas which strike oblique to the major fault, so that green coloured areas represent mainly fault-segments. In the curvature map, most of the fault-segments are directly visually enhanced by the negative curvature values presented in red, yellow and green colours. Nearly all segment boundaries from the diagrams have been identified also on one or more fault attribute maps. However, a few fourth-order segments could not be correlated with fault attribute maps. This might be because the displacement-distance diagrams can identify fault-segments on a much smaller scale. In general, the fault-surface roughness seems to change with depth. The upper part of the fault-surface between the hanging wall and footwall of h2 is characterised by a higher amount of small fault segments with respect to the area of h1. In h1 small segments can only be identified in the displacement-distance diagram in such detail, but rarely on the attribute maps.

The fault-morphology, especially the changes in dip, controls the slip-to-throw ratio. We calculated this ratio for the oldest horizon h1 (Fig. 4.5). Here, the slip-to-throw ratio varies along fault-strike between 1 and 1.8. The curve is strongly undulated and describes mainly concave shapes, which are separated by local maxima. These local maxima can be correlated in most cases with zones of segment linkage derived from the displacement-distance diagram (Fig. 4.3). The highest slip-to-throw ratio occurs within the large overlap zone, in which the second-order fault segments are linked. The reason for this correlation is that fault-segment boundaries have typically lower fault-dip and smaller displacement with respect to the segment centre, which results in a higher slip-to-throw ratio.

Figure 4.6 shows the amount of throw and heave with respect to slip of all data pairs along both horizons. Comparing the three curves indicates that they are not sub-parallel as it would be the case on a planar fault-surface. Instead, throw and heave strongly undulate in comparison to slip. In some cases, heave is even higher than throw. This occurs when the fault-dip is locally below

DOI: 10.2312/GFZ.b103-07087

45°, as it is the case in the area of the overlap zone (see dip map in Fig. 4.3). The higher the differences between throw and heave, the steeper the fault is. The heterogeneity in the displacement curves are mainly caused by fault-segmentation and the related undulation of the fault-surface. Additionally, the slip curve in this diagram (Fig. 4.6) is not a continuous line, but it is marked by steps of some tens of metres. These steps divide the curve into groups of similar slip, but the relation between throw and heave often varies.

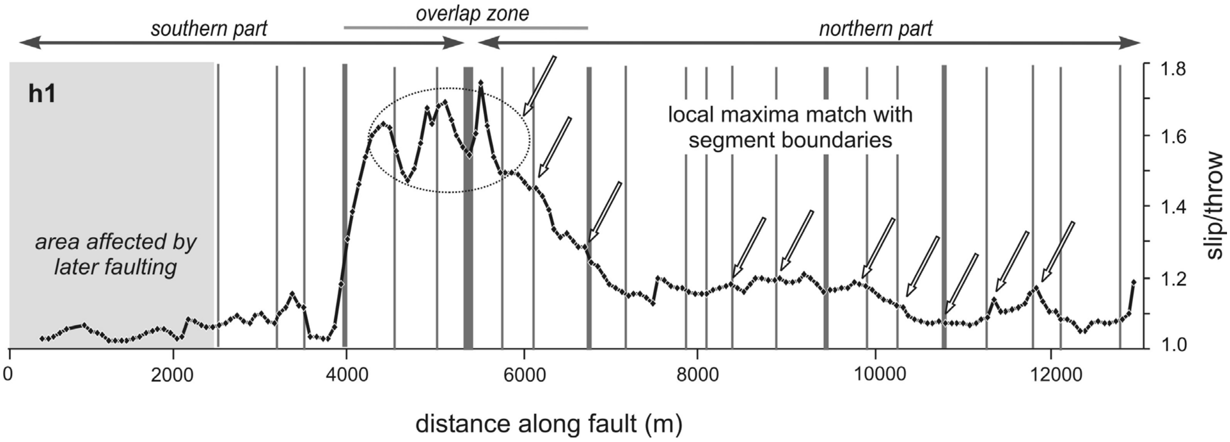

Figure 4.5: Slip/throw ratio of horizon h1. Vertical lines are segment boundaries derived from the displacement-distance diagram in Figure 4.3. In general, high ratios point to segments boundaries, whereas low ratios indicate fault segments. Here, arrows mark such maxima that correlate with segment boundaries.

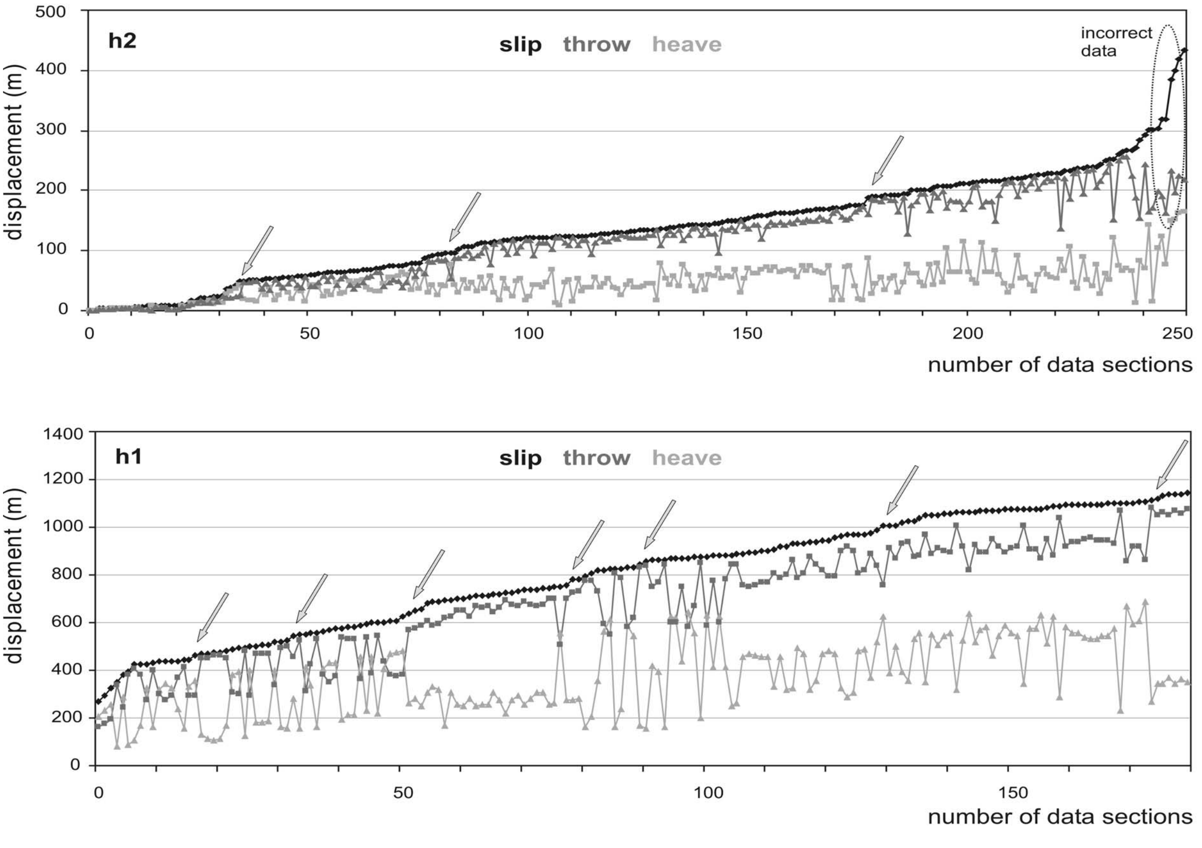

Figure 4.6: Variation of throw and heave with respect to slip. Data pairs of both horizons are ordered by slip. Steps in curve represent groups of segments with similar displacement pattern.

DOI: 10.2312/GFZ.b103-07087

4.4. Discussion

4.4.1. Fault corrugations and displacement calculations

With the here used methods of 3D fault interpretation and subsequent attribute analysis and displacement measurements, we identified corrugations as former segments on a present-day large fault-surface, over a scale range from a few hundred metres to several kilometres. The consistency in interpretation results over that range of scales and demonstrates the validity of the two methods. We assume that the here analysed fault formed from smaller faults, which coalesced during fault-propagation in the Permian.

On a km-scale attribute analysis of the fault-surface highlights undulations or corrugations, which we interpret to represent former fault-segments and fault-linkage. Areas of negative curvature, which are concave to the hanging-wall, are interpreted as fault-segments. Areas of positive curvature, which are convex to the hanging-wall, are interpreted as breached relay zones where fault-linkage occurred. One example of negative curvature even highlights a possible transfer zone, which might indicate a breached relay ramp (Fig. 4.3). The fault-corrugations identified by attribute analyses are sub-parallel to fault dip, and are assumed to be aligned parallel to slip direction (also Needham et al., 1996).

By displacement analysis on a scale of a few hundred metres to several kilometres we identified four orders of segments illustrating different fault generations, getting younger with increasing fault-length. Each segment has its own slip-throw-heave relationship, which is mainly caused by differences in fault-strike and -dip, along both fault-strike and fault-depth (compare displacement-distance diagrams with fault attribute maps in Fig. 4.3). Differences along strike are caused by lateral coalescence of several segments (see also Needham et al., 1996; Marchal et al., 2003), whereas differences towards depth might be caused by vertical coalescence of several segments (Mansfield and Cartwright, 2001; Marchal et al., 2003), or by lithological inhomogeneities (Crider and Peacock, 2004), or a combination of both.

Our analyses show that the fault-surface topography evolves with increasing slip. Since we observed a variable fault-roughness associated with the horizon cut-offs rather than with depth, we assume that this roughness is related to displacement, rather than lithological inhomogeneities, or even interpretation uncertainties due to lower resolution at depth. In the here analysed scale the fault smoothes with increasing displacement. Therefore, we assume that coalescence of several segments leads first to an increase in fault-roughness, whereas during maturation the fault-surface becomes smoother. From outcrop data Sagy et al. (2007) also implied that mature fault-surfaces are smoother at small scales, and that slip correlates with fault-roughness.

The curves of the second-order, and partly the third-order segments are characterised by an asymmetric shape. The overlapping fault-tips have steeper displacement gradients than the corresponding distal tips (Fig. 4.3). This asymmetric fault-growth is caused by different fault-length propagation at both sides of the fault. During length propagation, the overlapping tips are hampered, but the free ends of the faults do propagate normally, as well as the growth in displacement is the same. This distortion of the displacement profile is typically observed in fault interactions (e.g. Peacock and Sanderson, 1991; Scholz, 2002).

The asymmetry in displacement-distribution of the smaller segments is caused by a higher displacement in the centre of the superimposed fault. The positions of displacement maxima are similar in both horizons, and the positions of third- and fourth-order segment boundaries are mainly coincident. However, the first-order fault boundaries do not match, because the fault-length is smaller at the younger horizon h2 (12 km), than at the older horizon h1 (15 km) (Fig. 4.3). That indicates that in this observable deformation stage, the fault propagated only in displacement, but no tip propagation at the free ends of the fault has occurred.

4.4.2. Implications for fracture prediction, scaling, and seismic hazard assessment

The variable displacement along fault-strike caused by segment linkage, and the variable slip/throw/heave relations caused by differences in segment orientation, can result in heterogeneous deflections of horizons close to the fault, and should therefore have an influence on different fault drag geometries along the fault (reverse or normal drag). Barnett et al. (1987) suggested that different drags result from a local decrease or increase in displacement in fault-dip direction, and also Grasemann et al. (2005) argued that the sense of fault drag is mainly a function of the angle between the horizon and the fault plane, and therefore of the variation in fault-dip.

Care should be taken when calculating the length vs. displacement relationships, displacement vs. cumulative frequency relationships, or displacement through time, especially for a predictive purpose. An ideal self-similar growth is rarely observed; there is a lot of scatter in displacement-length correlation plots, which is caused by the process of segment linkage (Cartwright et al., 1996; Mansfield and Cartwright, 2001), and maybe also due to the use of throw and heave values rather that slip. Because of strong differences in slip, throw, and heave of mature, high-undulating faults, it is necessary to use slip values as they represent the real displacement. Otherwise, the use of heave and throw values lead to underestimation of the real fault-displacement. To work out the precise effects, it would be necessary to calculate the length vs. displacement relationship over time for all segments of one fault. However, in a segmented fault, the original lengths and displacements of the several segments are difficult to reconstruct, because they are underrepresented due to linkage. The present-day observable fault-lengths and fault-displacements in the displacement-distance diagram are slightly smaller than in reality, because they are related to a certain horizon that may not indicate the beginning of deformation. The solution would be to interpret for each segment that horizon which documents the beginning of faulting. However, in our example there is a lack of continuous and datable horizons for doing such detailed interpretations. Furthermore, the here analysed fault is not large enough for documenting a statistically relevant number of fault-segments. For these reasons, it was not possible to demonstrate specific implications on e.g. displacement-length scaling law between length vs. slip, length vs. throw, and length vs. heave in the here introduced example.

According to the inhomogeneous fault-roughness, the rocks around the fault should show an inhomogeneous strain field with high fracture concentration in areas of strong fault undulations (high curvature) (Lisle, 1994). Fault zones of high curvature are affected by higher deformation, and are therefore characterised by a higher fracture density. Hence, a large segmented fault shows a variable fracture density along both fault-strike and fault-depth. From fault analysis on the here studied scale, it might be possible to make qualitative predictions about fracture density around the major fault also on a much smaller scale, e.g. below the seismic resolution down to a few metres or even well data scale. This finally helps to localise strongly fractured zones, which is important for analyses of fluid migration and for reservoir characterisation.

Our analyses show triangular- to half-elliptical-shaped displacement profiles, clearly visible in slip, but rather in heave or throw. A triangular shape of displacement profiles is considered typical for long-term slip profiles derived from multiple rupture-surfaces from earthquake processes (e.g. Nicol et al., 1996; Manighetti et al., 2001, Manzocchi et al., 2006). However, this triangular shape from seismological analyses has not been shown by analyses from seismic data; instead, in these studies fault-growth is typically characterised by an elliptical to half-elliptical displacement curve (e.g. Meyer et al., 2002; Nicol et al., 2005; Bull et al., 2006). A reason for this discrepancy could be that fault-growth evolution has generally been inferred from the geometrical characteristics of faults of different size in the same population, rather than from kinematic analysis of an individual fault. Displacement profiles of one single mature fault change continuously through time due to segment linkage. Neighbouring faults act as barriers and hamper tip propagation, which results in a higher displacement gradient and necessarily a more triangular curve. However, the often used heave or throw values generate only an elliptical to half-elliptical shape due to under-representation of slip by constant fault-length, as it is illustrated in our displacement profiles (Fig. 4.3). Additionally, the use of only 2D seismic profiles, instead of a complete 3D interpretation, lowers the sampling rate significantly, which results in (1) a smoothing of the displacement curves, (2) an incomplete identification of fault segments, and (3) a nearly impossible recognition of a potential triangular-shaped curve. In the latter case, a triangular curve can only be identified in 2D interpretations by chosen the exact position of maximum displacement, and in addition numerous profiles around to prove the displacement gradient towards the fault tip. With this method, a triangular curve can only be identified by chance.

Analyses of the morphology of large faults are important for improvement of seismic hazard assessments. From seismological data, inhomogeneities on large-scale fault-surfaces are known as asperities. These asperities are described as areas of higher resistance against the general motion, caused by structural heterogeneities or varying material properties (Sobiesiak, 2005). During rupturing of asperities, these areas are characterised by an increased seismicity and higher slip values. Fault-morphology analyses could help to identify areas with high earthquake potential of seismic active faults, and to elucidate better the rupture process along the surface. However, for testing the comparability of the fault-surface roughness with the seismological potential, it is necessary to apply both analyses, 3D seismic and seismological data, on one single large-scale fault in very detail. If areas of increased slip correlate in both methods, and areas of segment linkage correlate with asperities, than the here introduced fault-morphology and displacement analysis from 3D seismic data will be an important contribution for the improvement of seismic hazard assessment.

4.5. Conclusions

(1) In this study we demonstrate fault-analysis of a c. 13 km long segmented fault, derived from detailed interpretation of a high-resolution 3D seismic data set. Here, we present for the first time the evolution of fault-segmentation on a single normal fault, with the combined methods of morphology analysis (dip, azimuth, and curvature attributes) and displacement measurements. We identified four orders of segments on two horizons getting younger with increasing fault-length, over several scales from 200 m to 15000 m fault length.

(2) Fault attribute maps (dip, azimuth, curvature) and displacement diagrams emphasise changes in fault-strike and fault-dip of the fault-surface. Our analysis shows a strong variation in slip, throw, and heave, especially in areas where fault-segments are linked. The difference in the amount of displacement increases with undulation along fault-strike and fault-dip. Consequently, throw and heave should not be used as approximation of slip, and are not representative for fault-analysis (e.g. fault-propagation through time, length vs. displacement relationship, displacement vs. cumulative frequency) of large segmented faults. Otherwise, high amounts of slip will be under-represented.

DOI: 10.2312/GFZ.b103-07087

(3) Fault-morphology analyses of large-scale faults can be important for improvement of seismic hazard assessments, as the fault-roughness is possibly associated with the heterogeneous distribution of earthquake data.

(4) The here presented slip profiles are characterised by a triangular to half-elliptical shape, rather than being elliptical. We assume that the use of 2D profiles instead of 3D data, and the use of heave and throw instead of slip, leads to an incomplete identification of fault-segments, and therefore results not only in a smoothing of the curves, but also in a change from triangular to (half-) elliptical displacement curves. Hence, the high complexity of fault-growth in time and space requires a detailed analysis in 3D.

DOI: 10.2312/GFZ.b103-07087

5. Analogue modelling of fault-growth processes

5.1. Introduction

Within the upper brittle crust, sandstone is a widely distributed rock in many sedimentary basins. The large sedimentary Permian Basin in Central Europe, for example, is characterised by a high occurrence of sandstones, but also by volcanic rocks, siltstones, mudstones, evaporates, conglomerates, and carbonate, deposited during Permian times (e.g. McCann, 1998; Glennie, 1998). We analysed a 3D seismic data set with corresponding well data located in the centre of the Southern Permian Basin. From drill-cores and composite logs we identified Permian sandstones, interbedded with conglomerates, volcanic rocks, and rarely mudstones.

Normal faults developed in these brittle rocks during Permian extension. In the seismic data we measured an average fault-dip of 60°, which steepens towards the former surface. Detailed analyses near these large-scale faults indicate a strong fracturing of the hanging walls. This fracturing is very heterogeneously distributed and occurs predominantly at a scale below seismic resolution. Deformation on a wide scale range, between seismic-scale and borehole-scale, is evident as seismic and sub-seismic deformation which occurred during several deformational events, observed today in their final stage. However, also the timing of fracturing within one deformational event is important, in order to evaluate the detailed spatial strain evolution, and subsequently to characterise reservoirs. Deformation is variable over time, and can lead to an opening of fractures when they are active, or to a cementation and therefore closure of fractures when they are inactive. Hence, it is important to study the timing of deformation in order to understand the evolution of small-scale fracturing related to large-scale faults, and to improve predictions in terms of fracture connectivity and fluid circulation depending on different deformation increments.

In this study we present scaled 2D physical models based on extensional deformation of a cohesive mixture of sand and gypsum. We studied the detailed evolution of normal faults in a graben above a rigid basement, in order to evaluate its deformation in time and space over a wide scale range. The material properties and the apparatus setup allow a scaling of the laboratory experiments with respect to the natural prototypes in the North German Basin. The structural evolution and displacement field was analysed by digital photography and Particle Image Velocimetry (PIV).

5.2. Scaling of the sandbox model

For a scaled model which simulates the uppermost part of the brittle crust exhibiting steep structures, open fractures, and shear fractures in very detail, the used analogue material requires a small grain size, and a significant cohesion, and appropriate tensile strength.

In preliminary parameter studies we investigated the behaviour of different materials such as sand, cement, starch, gypsum, and mixtures among them. Pure sand is not suitable for our purpose because its cohesion is too low and it develops no tensile fractures. Pure starch, cement, and gypsum are characterised by a high cohesion and tensile fractures, but shear fractures developed only secondarily. The most suitable analogue material is a mixture of sand and gypsum in relation 3 to 1.

DOI: 10.2312/GFZ.b103-07087

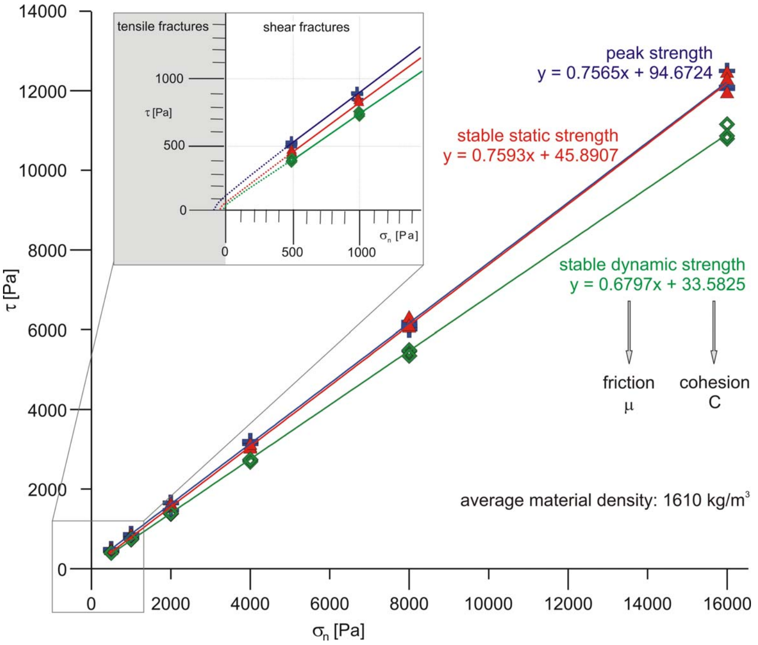

Figure 5.1: Measured stress-diagram showing the normal stress σ_n against shear stress τ of the used sand(3)-gypsum(1) material. Enlarged area shows assumed continuation of the curve, indicating the occurrence of tensile fractures.

The used sand is a Quaternary, glacial, almost pure quartz sand with a grain size below 0.63 mm, whereas the gypsum is a very fine-grained powder. The mechanical properties of the sand(3)-gypsum(1) mixture were measured in shear tests with a ring-shear tester (Schulze 1994). Its density varies between $\rho = 1511$ kg/m^3 and $\rho = 1639$ kg/m^3 depending on the normal stress, but the average value is $\rho = 1610$ kg/m^3. We measured the strength of the material in three different cycles: the peak internal strength during fault initiation, the stable static strength during fault reactivation, and the stable dynamic strength during further ongoing deformation. Friction (μ) and cohesion (C) were then calculated with $\mu = 0.76$ and C = 94.67 Pa for peak strength, $\mu = 0.76$ and C = 45.89 Pa for stable static strength, and $\mu = 0.68$ and C = 33.58 Pa for stable dynamic strength (Fig. 5.1).

The Rotliegend sandstone in our study area is a fine-grained, homogeneous, brownish, eolian-dune sandstone with well visible sedimentary bedding and numerous thin fractures (deformation bands), which are mainly cemented by quartz (Fig. 5.2). The density of this sandstone is $\rho = 2640$ kg/m^3, which was measured and provided by RWE Dea. Cohesion and friction was not measured, but typical rock parameters for this sandstone indicate a friction of approximately $\mu = 0.6$, and a cohesion between C = 20 - 50 MPa. However, since the rocks in our study area are strongly fractured, the cohesion can be much lower than these average values, and we would rather assume a cohesion of C = 5 - 20 MPa.

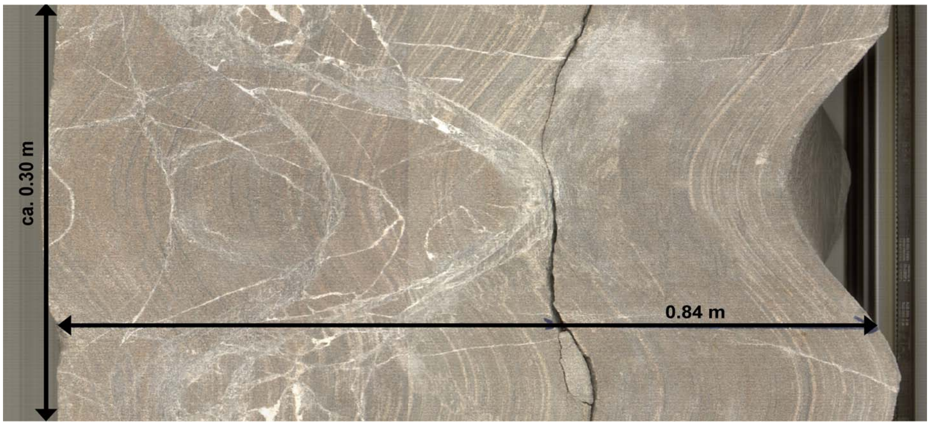

Figure 5.2: Unwrapped scan of a typical drill core of the study area, representing Rotliegend dune sandstone with sedimentary bedding (brownish) and quartz-filled fractures (whitish).

DOI: 10.2312/GFZ.b103-07087

The geometric scaling factor was calculated after Ramberg (1981):

$$\mathbf{S = (C_n\rho_m)/\ (C_m\rho_n)}, \qquad [1]$$

where **S** is the scaling factor, **C** the cohesion, and **ρ** the density. The index **m** indicates the material of the analogue model, and the index **n** represents parameters from natural rocks. With

C_n = 5 - 20 MPa
ρ_n = 2640 kg/m^3
C_m = 33.58 - 94.67 Pa
ρ_m = 1610 kg/m^3 ,

S lies in the range between 10^4 and 10^5 depending especially on the strength of the rock type. That means for the length scaling of our model, that 1 cm corresponds to 100 to 1000 m in nature.

5.3. Model setup

The modelling box (Fig. 5.3) is 60 cm in length, 20 cm in width, and is equipped with a rigid base that dips at 60°. The left rigid base is fixed to avoid shearing and subsequent bending of the analogue material due to friction along the glass walls. The middle and right rigid base are movable. A motor is moving the middle rigid base down, which sits on top of a ball-bearing to allow both vertical and horizontal movements following the shape of the 60° dipping base. The rigid base to the right is following passively the movement of the middle base. We focused our observations on the left part (green rectangle in Fig. 5.3).

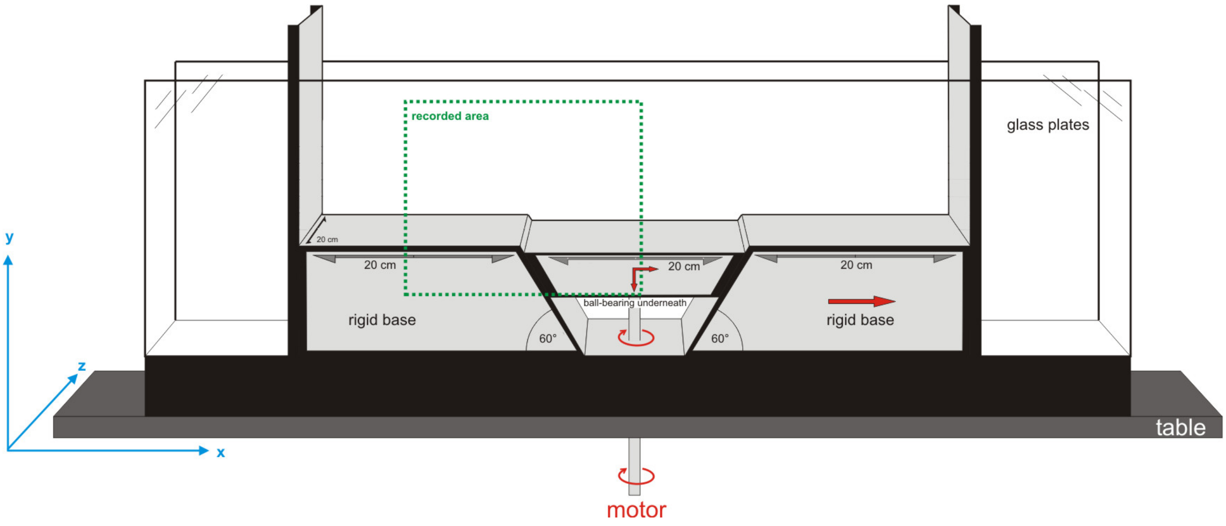

Figure 5.3: Sketch of the extensional deformation box. Red arrows indicate moveable elements.

The model simulates an unfaulted cover on top of a rigid basement with faults dipping 60°. The left rigid base simulates the footwall, whereas the middle rigid base represents the hanging wall. Influence by friction along the glass plates was avoided by fixing the footwall, so that only the hanging wall was moved relative to the footwall. The sand-gypsum mixture was sieved homogeneously up to a height of 9 cm (corresponds to 900 to 9000 m in nature). Very thin layers of dark sand were added regularly in 1.5 cm steps for a better visualisation, but they did not affect significantly the faulting behaviour.

DOI: 10.2312/GFZ.b103-07087

The experiments were monitored and analysed with a high-resolution digital camera and corresponding PIV technology (Particle Image Velocimetry). PIV is an optical technique to observe movements and flows by calculating the displacement field of grains, and allows the calculation of strain and rotation within the material. During the experiment a sequence of images was recorded, and the LAVISION software DaVis calculates the 2D vector field by comparing the pattern of grains of neighbouring images.

Seven experiments have been done with the same experimental setup and material parameters for statistically relevant repetitions. All experiments have been performed with a final vertical displacement of ca. 2.5 cm, during which ca. 630 images have been taken.

We carried out the experiment with the following parameters:

Optical resolution: 9 pixel/mm (2000 x 2000 pixels for the recorded area)
→ Resolvable scale: 1 mm to 9 cm (corresponds to 10 m to 9000 m in nature)
Vertical displacement rate: 0.16 mm/s
One camera, recording time: 4 pictures/s
→ 1 picture every 0.04 mm vertical displacement

The low velocity, the high sampling rate, and the high optical resolution allowed a high spatial and temporal resolution during deformation of the analogue material.

5.3. Results

All experiments are reproducible since they show similar structural elements and evolution. The results of the processed experiment shown here comprise only the very beginning of deformation, as it is that part where fault-growth processes were initialised. Therefore, the area of the deformation experiment which has been recorded is much larger than the one which has been finally processed with the PIV technology for this purpose (Fig. 5.4).

At the beginning of deformation, we observed vertical fractures in the upper part of the material, which open perpendicularly to the surface (tensile fractures). The lower part of the material is characterised by very small and short-living tensile fractures oblique to the surface, which connect rapidly to build shear fractures (zoomed area of Fig. 5.4). In the processed image, the colour-code illustrates the rotational strain, in particular the rotation of particles around the z-axis, and indicates a clockwise rotation (synthetic faulting) with green, yellow, and red colours, and an anticlockwise rotation (antithetic faulting) with blue and purple colours, depending on the relative magnitude of rotation. Zero rotation (inactive areas) is shown in black.

Several processed images are shown in Figure 5.5, which comprises 36 stages extracted from the initial deformation part of one representative experiment. Here, only every third image is shown, but also the images in between have been analysed. As it is documented in image 1 of Figure 5.5, the PIV technology also allows measuring the initial re-organisation of grains as small-scale deformation prior to failure. In image 1, the whole area is affected by subtle deformation, but deformation localises first in the lower part (fault [1a]). Afterwards, deformation is focused in the upper part (fault [1b]), whereas deformation in the lower part becomes more and more diffuse (images 2 to 5), propagates towards to right (images 4 to 7), and localises as vertical fault [2a] growing upwards (images 7 to 12). The previous initiated faults [1a] and [1b] are now inactive, and the vertical faults [2a] and [2b] are active (image 12). Both faults [2a] and [2b] show a higher strain magnitude than the part in between them (blue arrow in images 12 to 16).

DOI: 10.2312/GFZ.b103-07087

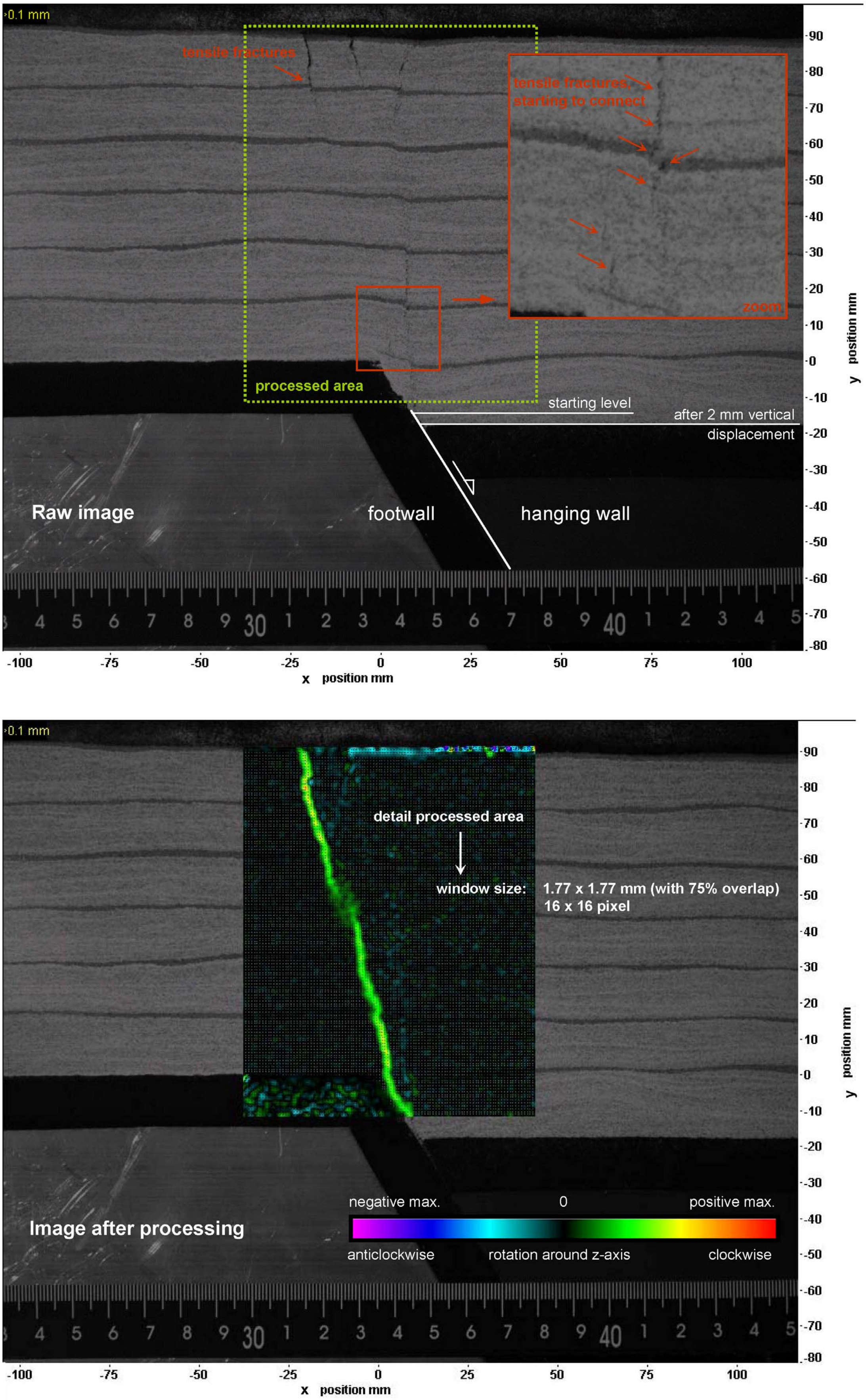

Figure 5.4: Image of the extensional deformation experiment before (top, illustrating the fracture system) and after processing (bottom, documenting active faults).

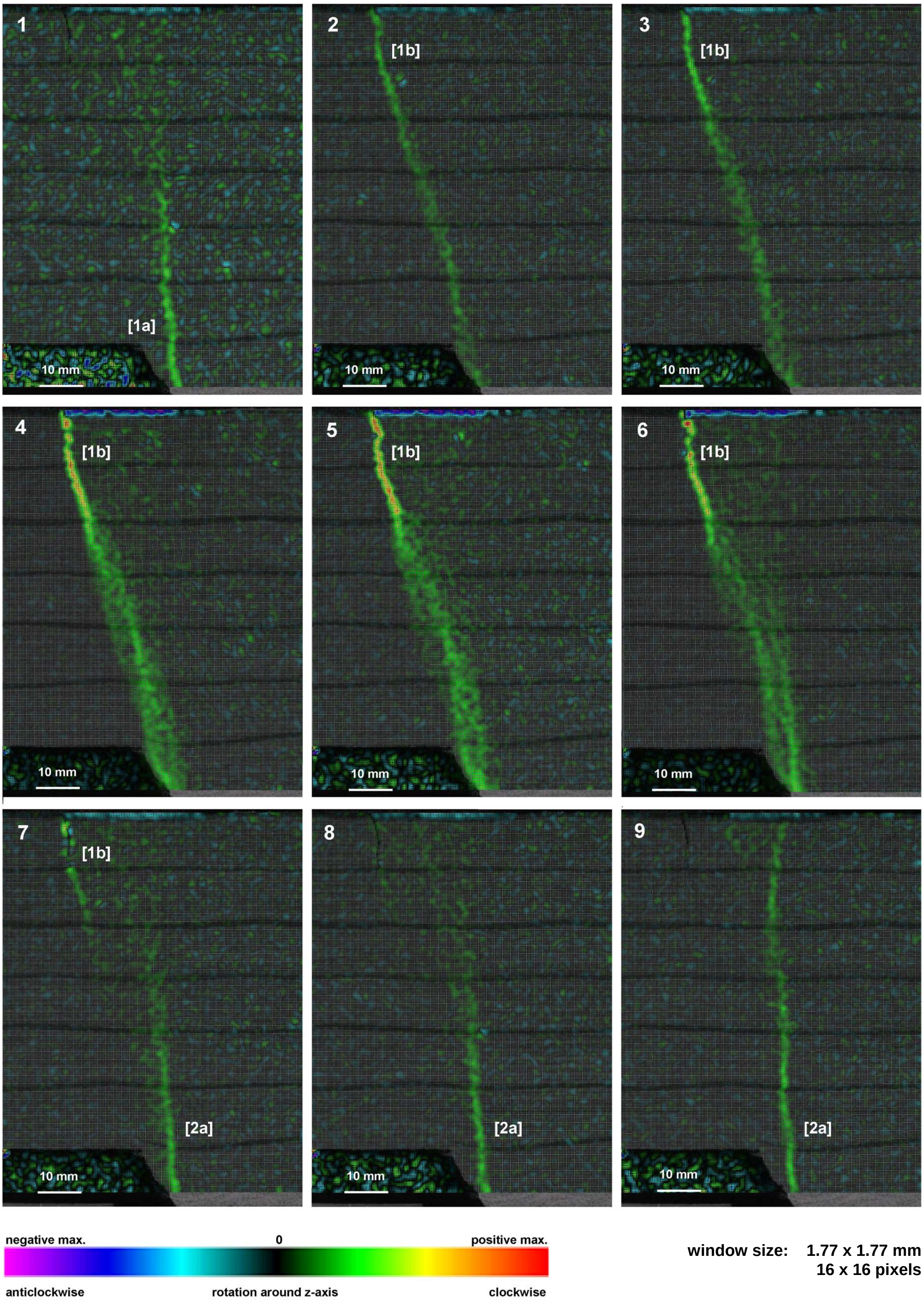

Figure 5.5: Sequence of processed images (profile view) documenting fault-growth processes during extensional deformation.

DOI: 10.2312/GFZ.b103-07087

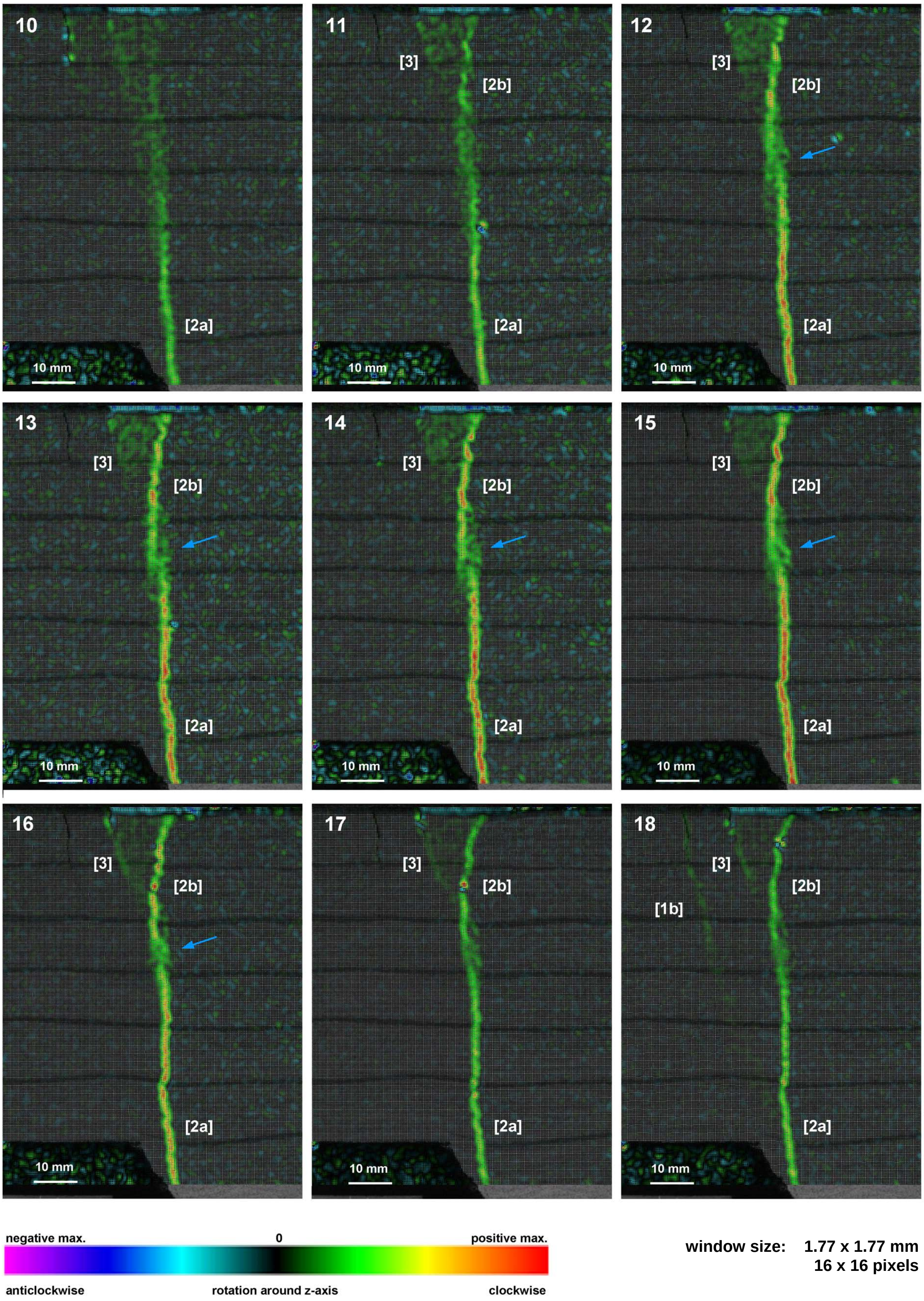

Figure 5.5, continued. Blue arrow marks a low strain zone separating two faults in vertical.

DOI: 10.2312/GFZ.b103-07087

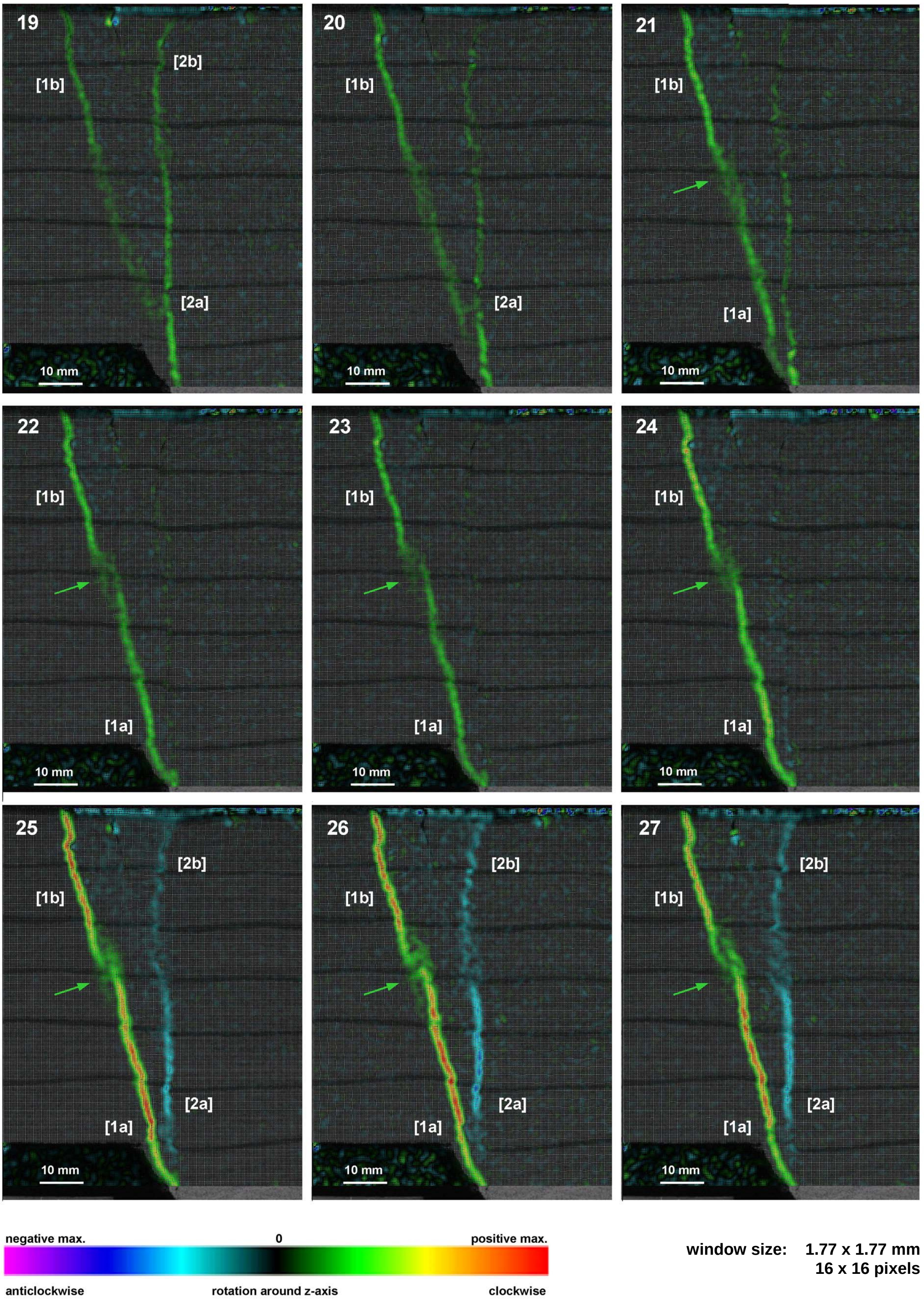

Figure 5.5, continued. Green arrow marks a low strain zone separating two faults in vertical.

DOI: 10.2312/GFZ.b103-07087

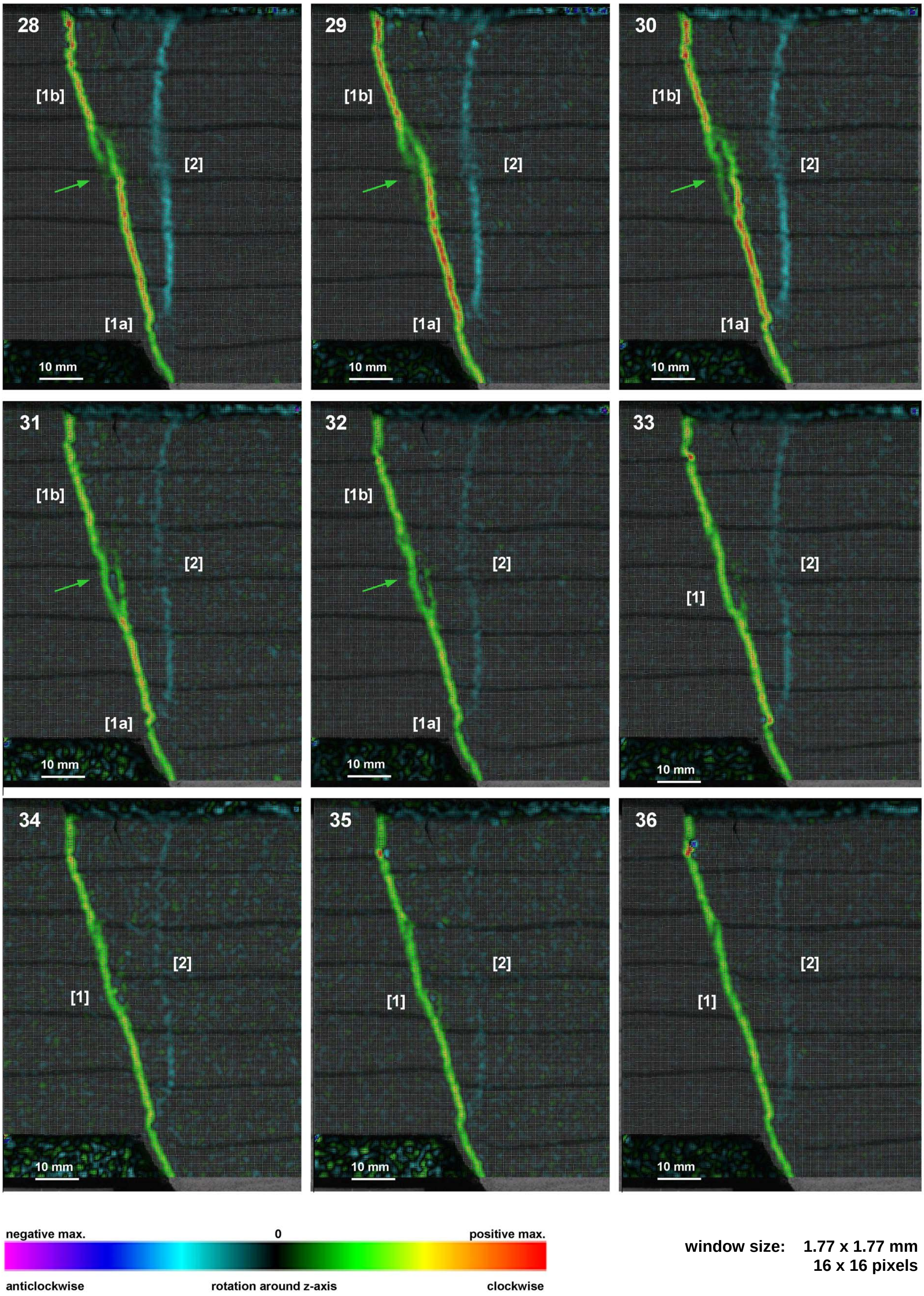

Figure 5.5, continued. Blue arrow marks a low strain zone separating two faults in vertical.

DOI: 10.2312/GFZ.b103-07087

With increasing deformation, another tensile fracture [3] becomes active close to the surface, antithetic to fault [2b] (image 11), and prolonged until fault [1b] becomes active again and accommodates deformation further left (image 18). Image 18 shows that both faults [1b] and [3] are active. For the following period of images 20 to 36, deformation concentrates again on faults [1a] and [1b]. These faults are characterised by a heterogeneous deformation along dip, since they show a high deformation magnitude, but they are connected by a diffuse and low-magnitude deformation zone (green arrow in images 21 to 32).

The activity of faults [2a] and [2b] started to decrease from image 18 (when faults [1a] and [1b] became active again) until it was completely inactive in image 23. However, these faults started to be active again, but in the opposite movement direction (images 24 to 36). In the first stages this deformation occurred as small-scale strain affecting the whole hanging wall (images 25 to 27). Later it localised into a through-going fault [2] (image 28), and activity decreased further (images 34 to 36).

5.3. Discussion

With these analogue experiments we detected extensional deformation with a very high resolution in space and time. Hence, we were able to observe the initiation of faults and the alternation of active deformation between them. The observed structures in the analogue experiments are comparable with the structures recognised in our 3D seismic data set. We also interpret that the fault-growth processes derived from the analogue modelling might be similar to those which underlie the seismic structures of the study area.

Both faults [1a] and [1b] initiate at the very beginning of deformation in images 1 and 2 (Fig. 5.5). During ongoing deformation both parts started to link (green arrow in images 21 to 32), and finally grew as one connected fault with the same strain magnitude (images 33 to 36). The linkage area is a zone where deformation is accommodated in a wide and diffuse area showing a lower strain magnitude with respect to both fault-parts, prior to linkage. In this area, the tip of both fault-parts converge, and are steeper than the centre of both fault-parts (Fig. 5.6), as it is typical for tip-propagation of cracks observed in natural rock deformation experiments (Fig. 5.6). The same process might have occurred a few seconds before along fault [2], where both parts [2a] and [2b] have been linked (blue arrow in images 12 to 16). Linkage of fault-segments results in changes in fault-dip (e.g. image 36 in Fig. 5.5). This could later still be recognisable as undulation of the whole fault-surface, as suggested by seismic data.

The activity between the two main faults [1] and [2] alternates over time. Deformation initiates first in fault [1], propagates then to fault [2], afterwards it moves back to fault [1], and then again to fault [2]. During that alternation, deformation propagates through the material and affects the area between both faults pervasively on a small-scale.

A re-organisation of the analogue material grains is recorded within the hanging wall prior to localisation of deformation and initiation of faults. This grain re-organisation can be interpreted as small-scale deformation, and is comparable with the sub-seismic deformation typically identified in bore-hole data. As observed in the analogue modelling, deformation is concentrated on two main faults only, but small-scale deformation is affecting a much wider area. Additionally, small-scale deformation seems to differ not only spatially from large-scale deformation, but also temporally, as it occurs usually within the hanging wall prior to fault-localisation (Fig. 5.5). That means for the process of alternation of fault-activity, that small-scale deformation alternates correspondingly through time.

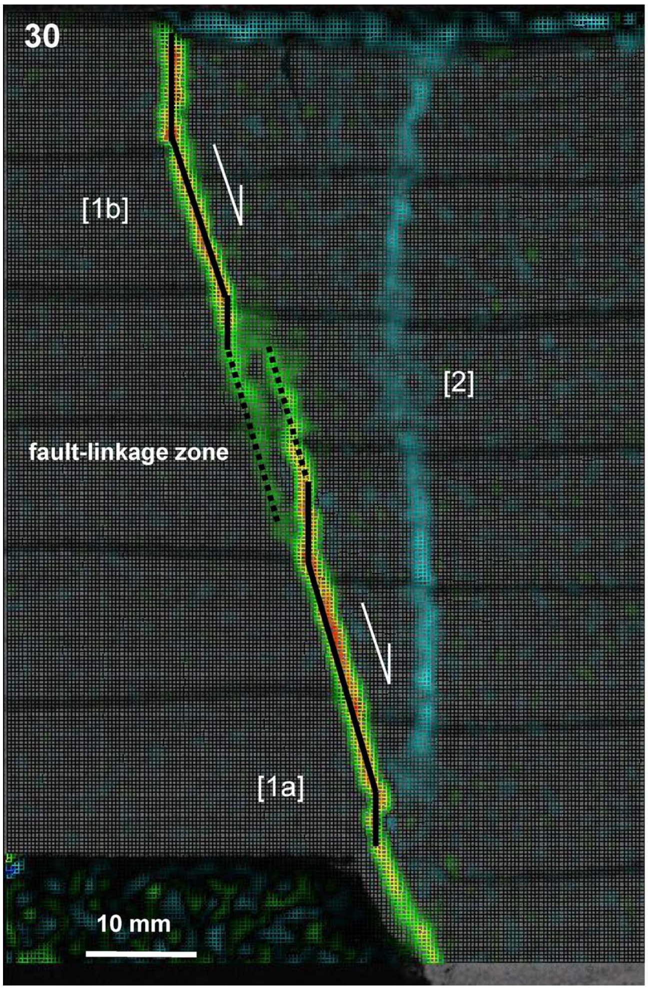

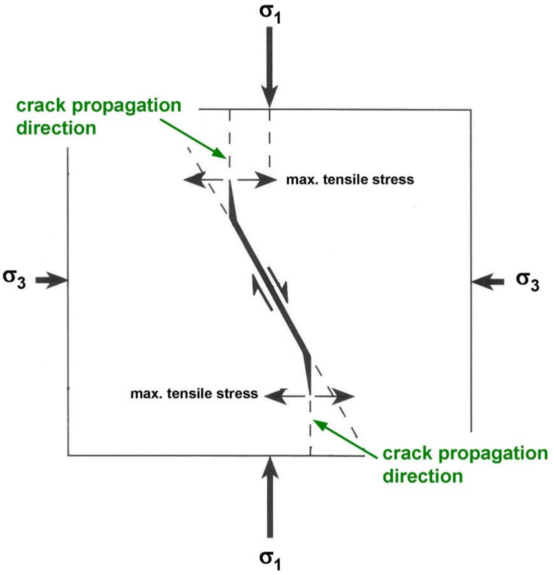

Figure 5.6: Detailed view of image 30 (left) illustrating convergence and linkage of two fault-segments by tip-propagation, as it is typically observed in deformation experiments under confining pressure (right sketch, modified after Twiss & Moores, 1992).

As one possible outlook of this study, we plan to quantify this small-scale deformation with respect to the large-scale deformation that occurred on main faults, by evaluating both the effectively deformed area and the strain magnitude. These parameters will be measured over time, set in reference to the total amount of strain, and subsequently compared with the results of chapter 3. As far as observable already in the experiments, we assume that the small-scale, and therefore sub-seismic deformation, makes a significant contribution to the total strain. The results of these analyses can help to provide better estimations for palinspastic reconstructions, and for characterisations of fractured reservoirs.

5.4. Conclusion

The extensional deformation described here with physical analogue models occurred during a time interval of 25 seconds and a vertical displacement of 4 mm (represents 40 to 400 m in nature). The short time window and the low displacement allowed us to observe significant deformation processes such as small-scale deformation, initiation of tensile and shear fractures, fault-propagation, vertical linkage of fault-segments, and alternation of fault activity between different faults.

By understanding fault-growth processes in analogue materials, it may be possible to predict areas of high small-scale strain such as fault-linkage zones or areas of pervasive deformation between

DOI: 10.2312/GFZ.b103-07087

large faults within the model. This can then be compared with the natural example and can help to estimate the sub-surface fracture density.

6. Paleostress analysis from 3D seismic data – an outlook

6.1. Introduction

Undulation of fault-surfaces is a commonly observed feature in 3D seismic data. The corrugations thereby identified on the fault-surfaces are assumed to result from the linkage of numerous smaller fault-segments through time (e.g. Walsh et al, 1999; McLeod et al., 2000; Mansfield and Cartwright, 2001; Marchal et al., 2003). Such undulating fault-surfaces have also been observed in the field, including features such as ribs, saddles, and depressions, which occur over a range of several scales (e.g. Wright and Turner, 2006; Sagy et al., 2007). Striation measurements on field-observed corrugations indicated that corrugations are parallel to fault slip (Hancock and Barka, 1987). Therefore, these corrugations observed in the field might be comparable to those observed in seismic data. Needham et al. (1996) suggested that fault-corrugations observed in the seismic data can indicate a movement direction parallel to the axis of corrugations because this movement direction will require least energy and therefore smallest strain.

In this study numerous normal fault-surfaces are interpreted from the 3D seismic data and their undulations are analysed in 3D. The axes of corrugations are then used as movement directions. The paleostress direction during Permian extension is finally derived.

6.2. Data base and methods

For this study we analysed a pre-stack depth-migrated 3D reflection seismic data set, provided by RWE Dea AG, Hamburg. Well data documented sandstone, conglomerates, and volcanic rocks, which were deposited synsedimentarily during the Permian. The seismic volume has a high resolution with a grid spacing of 25 m by 25 m, and approx. 30 m vertical resolution for the depth of the analysed faults. Detailed 3D fault interpretation is based on seismic picking of every third seismic line (75 m interval) perpendicular to fault-strike, numerous lines oblique to fault-strike, and horizontal correlations on depth slices. The seismic volume was interpreted with the Schlumberger software GeoFrame/IESX, and triangulation of fault-surfaces was carried out with the software package GoCad (GOCAD Consortium).

Ten normal faults have been analysed by applying the attribute curvature. Gaussian curvature at a given point is the product of the two principal maximum and minimum curvatures. By flattening the 3D triangular grid, positive curvature is defined by a gap forming between flattened triangles of a dome, whereas negative curvature is defined by an overlap forming between flattened triangles of a saddle or basin. Surfaces with a high Gaussian curvature like domes or saddles are non-cylindrical, whereas cylindrical surfaces like elongated folds and corrugations have a Gaussian curvature of zero (Lisle, 1994). For that reason the minimum or maximum Gaussian curvature can be used because it highlights well convex and concave areas on cylindrical surfaces.

6.3. Results

All Permian normal faults show a strong undulation of their surfaces because they developed as a result of propagation and coalescence of several small fault-segments through time, as demonstrated in chapter 4. Figure 6.1 shows all fault-surfaces colour-coded with depth and curvature. The general orientation of the faults is illustrated with the depth colour-code, whereas corrugations are well visible with the curvature attribute, changing from blue to red. The spacing between the here analysed corrugations is between 500 m and 2000 m.

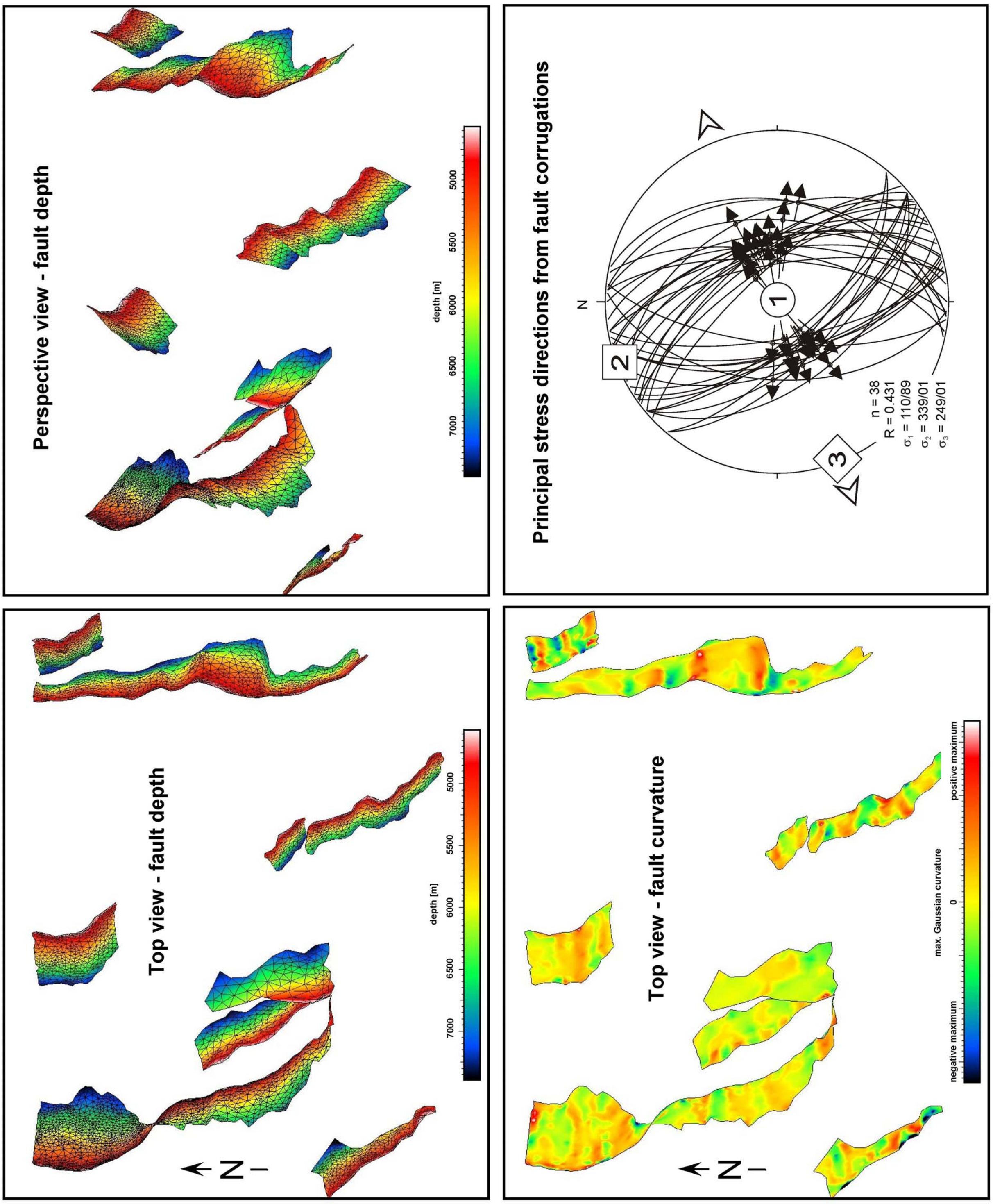

Figure 6.1: Permian normal faults in perspective and map view, coloured by depth (showing fault-orientations) and curvature (highlighting fault-corrugations). Area size: 17 x 22 km. Fault-corrugations axes are used as kinematic vectors, from which paleostress data have been derived. The plane-lineation-movement sense data and the principal stress directions are plotted in a Schmidt net, lower hemisphere, equal area projection. Used method is NDA, numerical dynamic analysis.

DOI: 10.2312/GFZ.b103-07087

For paleostress analysis, the azimuth and dip of all triangles from each corrugation was measured, and the average value refers to the orientation of the corrugations axis, which was used as fault-surface azimuth/dip, and equally as bearing/plunge of the 'striae'. The sense of slip of the hanging wall was derived from the seismic data. Principal stress directions were calculated by using numerical dynamic analysis (Spang, 1972), and the associated computer program NDA (Sperner & Ratschbacher, 1994). Numerous corrugations ($n = 38$) have been measured for paleostress analysis (Fig. 6.1). The analysed data show a WSW-ENE directed extension during Permian times. From the plane-lineation-movement sense data, the NDA software calculates R, the ratio of the principal stress differences, with $R = (\sigma_2 - \sigma_3)/ (\sigma_1 - \sigma_3)$. In this data set $R = 0.431$ (Fig. 6.1), which refers to plain strain extensional deformation.

6.4. Discussion

The here described method of paleostress direction analysis from 3D fault-corrugation interpretation is presented for the first time. Estimates about the information content of subsurface data as related to a past stress regime have been derived usually from the strike of tectonic structure, interpreted from 2D or 3D seismic data. These measurements are not precise, since they represent only the orientation of faults but no indicators of movement direction on the fault-surfaces. The method suggested here is particularly useful in areas which are not assessable by field campaigns, and where paleostress data from subsurface strata need to be carried out.

The inferred WSW-ENE Permian extension direction fits the overall E-W extension direction proposed for the Southern Permian Basin region very well (e.g. Betz et al., 1997; Ziegler, 1990). However, in the published literature reliable paleostress data do not exist for the Permian within the North German Basin. Permian strata are usually not directly assessable due to its position in great depths between 3 and 9 km. Only in a few areas (e.g. Harz Mountains, Flechtlingen High) Permian strata have been exposed on the surface, but they are either strongly overprinted by exhumation processes, or relevant measurable Permian fault-surfaces are missing. 2D seismic lines, which are numerous available for studying subsurface Permian structures, are subject to spatial artefacts and are therefore not suited for 3D paleostress measurements. However, depth-migrated 3D seismic data sets are rarely available in the North German Basin, but they are the only data which allow paleostress analyses of faulted strata in the subsurface.

In this study we present for the first time stress data derived from 3D seismic data for subsurface Permian strata within the North German Basin, and it is therefore an important contribution not only methodologically, but also for paleostress analysis within the Southern Permian Basin.

DOI: 10.2312/GFZ.b103-07087

7. Final conclusions

After a general introduction in **chapter 1**, the results discussed in chapters 2 to 6 encompass basic questions about sub-seismic structures and deformational processes and their relation to large-scale structures.

In **chapter 2** we present results from interpretation of a 3D seismic data set, located within the NW German sedimentary basin. We focused on the development of faults, the timing of deformation, the amount of displacement during multiphase deformation, strain partitioning, and the interaction between salt movement and faulting. We recognised the central fault zone of the study area to be the Aller-lineament, an important NW-trending fault zone within the superimposed Central European Basin System. From structural and sedimentological interpretations we derived the following evolution: (1) E-W extension during Permian rifting, (2) N-S extension within cover sediments, and E-W transtension affecting both basement and cover, contemporaneously during Late Triassic and Jurassic, (3) regional subsidence of the Lower Saxony Basin during Late Jurassic/Early Cretaceous, (4) N-S compression within cover sediments, and E-W transpression affecting both basement and cover, contemporaneously during Late Cretaceous/Early Tertiary inversion, (5) major subsidence and salt diapir rise during the Cenozoic. We suggest that the heterogeneity in distribution and timing of deformation in the working area was controlled by pre-existing faults and variations in salt thickness, which led to stress perturbations and therefore local strain partitioning. We observed coupling and decoupling between pre- and post-Zechstein salt units: in decoupled areas deformation occurred only within post-salt units, whereas in coupled areas deformation occurred in both post-salt and pre-salt units and is characterised by strike-slip faulting.

In **chapter 3** 3D retro-deformation was performed on a detailed interpreted 3D structural model to simulate strain in the hanging wall at the time of faulting, at a scale below the seismic resolution. The modelling is based on a clear definition of a 6 km long fault in 3D, and the temporal and kinematic understanding of its deformation. The results show that (1) considerable strain ranging in magnitude between 0% and 20% is observed more than 1 km away from the fault trace, and (2) deformation around the fault causes strain variations, depending on the fault morphology. The angle between the regional and the local strain axis can differ up to 90°. This strain variation is responsible for the heterogeneous sub-seismic fracture distribution observed in wells. We linked the fracture density from well data with the modelled strain magnitude, and used the strain magnitude as a proxy for fracture density. With this method we can predict the relative density of small-scale fractures in areas without well data. Furthermore, knowing the orientation of the local strain axis we predict fault strike, and opening or reactivation of fractures during a particular deformation event. The here suggested workflow is a helpful tool for the prediction of small-scale faults and fractures, which is subsequently important for identifying compartmentalisation and fracture networks, and for improvement of fluid flow simulations and well placement.

In **chapter 4** we demonstrate a fault-analysis of a ca. 13 km long segmented fault, derived from detailed interpretation of a high-resolution 3D seismic data set. Here, we present the evolution of fault-segmentation on one single normal fault, with the combined methods of morphology analysis (dip, azimuth, and curvature attributes) and displacement measurements. We identified four orders of segments on two horizons getting younger with increasing fault-length, over several scales from 200 m to 15000 m fault length. Fault attribute maps (dip, azimuth, curvature) and displacement diagrams emphasise changes on the fault-surface. Our analysis shows a strong variation in slip, throw, and heave, especially in areas where fault-segments are linked. The difference in the amount of displacement increases with undulation along fault-strike and fault-dip. Consequently, throw and heave should not be used as approximations for slip, and are not representative for fault-analysis (e.g. fault-propagation through time, length vs. displacement relationship, displacement vs. cumulative frequency) of large segmented faults. Otherwise, high amounts of slip will be under-represented.

Fault-morphology analyses of large-scale faults can be important for improvement of seismic hazard assessments, as the fault-roughness is possibly associated with the heterogeneous distribution of earthquakes. The here presented slip profiles are characterised by a triangular to half-elliptical shape, rather than being elliptical as proposed in previous studies from 2D seismic data. We assume that the use of 2D profiles instead of 3D data, and the use of heave and throw instead of slip, leads to an incomplete identification of fault-segments, and therefore results not only in a smoothing of the curves, but also in a change from triangular to (half-) elliptical displacement curves. Hence, the high complexity of fault-growth in time and space requires a detailed analysis in 3D.

In **chapter 5** we simulate extensional deformation with scaled physical analogue models using a cohesive mixture of sand and gypsum. The observed structures in the analogue experiments are comparable with the structures recognised in the 3D seismic data set. Also, the fault-growth processes derived from the analogue modelling are comparable to those which underlie the seismic structures in our working area. The experiments were carried out over a large scale range that corresponds to 10 m to 9000 m in nature. The chosen short time window and low displacement rate resulted in a very high spatial (9 pixel/mm) and temporal (1 image every 0.04 mm vertical displacement) resolution. Hence, it was possible for the first time to detect significant deformation processes such as small-scale deformation, initiation and propagation of tensile and shear fractures, vertical linkage of fault-segments, and alternation of fault activity between different faults through time.

In **chapter 6,** a new method for paleostress analysis is introduced. Numerous normal fault-surfaces have been interpreted from the 3D seismic data, and their undulations are analysed in 3D. The axes of corrugations are used as movement directions since they require least energy and therefore smallest strain. Paleostress analysis for the Permian results in a WSW-ENE extension direction, and indicates plain strain deformation. The here for the first time presented stress data derived from 3D seismic data for subsurface Permian strata within the North German Basin, are an important contribution not only methodologically, but also for paleostress analysis within the Southern Permian Basin in general.

In these sub-projects we started studying the heterogeneity in time and distribution in space of large-scale basin-wide structures (chapter 2), continued an order of magnitude lower and focused on the undulation of fault-surfaces (chapters 3, 4, and 6), reaching down to the heterogeneous fracture pattern of small-scale bore-hole data (chapter 4), and finally summing up with the heterogeneous strain evolution in space and time covering a broad scale range with analogue modelling (chapter 5).

At all scales we observed a similar heterogeneity of deformation patterns, but the reasons are different depending on processes relevant for the actual scale (Fig. 7.1). At the large 2D or 3D seismic scale (10^5 to 10^3 m-scale) inherited basement structures, reactivated faults, the position of detachment levels, as well as diapir structures and their growth through time, strongly influence further deformational events by stress field perturbations and subsequent strain partitioning. At a smaller scale (10^2 to 10^1 m-scale), extensional faults are observable as highly undulating surfaces rather than planar faults, which is mainly caused by the growth and finally linkage of numerous smaller fault-segments over time. Movement along these undulating surfaces and the associated

DOI: 10.2312/GFZ.b103-07087

displacement changes along fault-strike cause a strong fracturing within the surrounding rocks in a sub-seismic scale (10^1 to 10^{-2} m-scale). In well data this deformation (plus other parameters influencing fracture-generation like rock-anisotropy and fluid pressure) can be identified as apparently chaotic fracture orientation. Alternation of activity between different faults and the thereby occurring propagation of strain through the rock volume appears to be a process which affects all scales.

This high spatial and temporal complexity of deformation can only be understood by the interpretation and analysis of four-dimensional data. Without information about the third or fourth dimension, and without appropriate information about deformation throughout the scale limits, one has to be aware that the scale-range that is investigated is limiting the interpretive potential, and influences the interpreted results as they depend finally on the methodology.

The comparison and correlation of deformation over such a large scale range is a challenge we focused in this project. As far as it is studied in this thesis, deformation can have a similar pattern over large scale ranges, but it often underlies different spatiotemporal causes, and that rises the question of its real correlative nature.

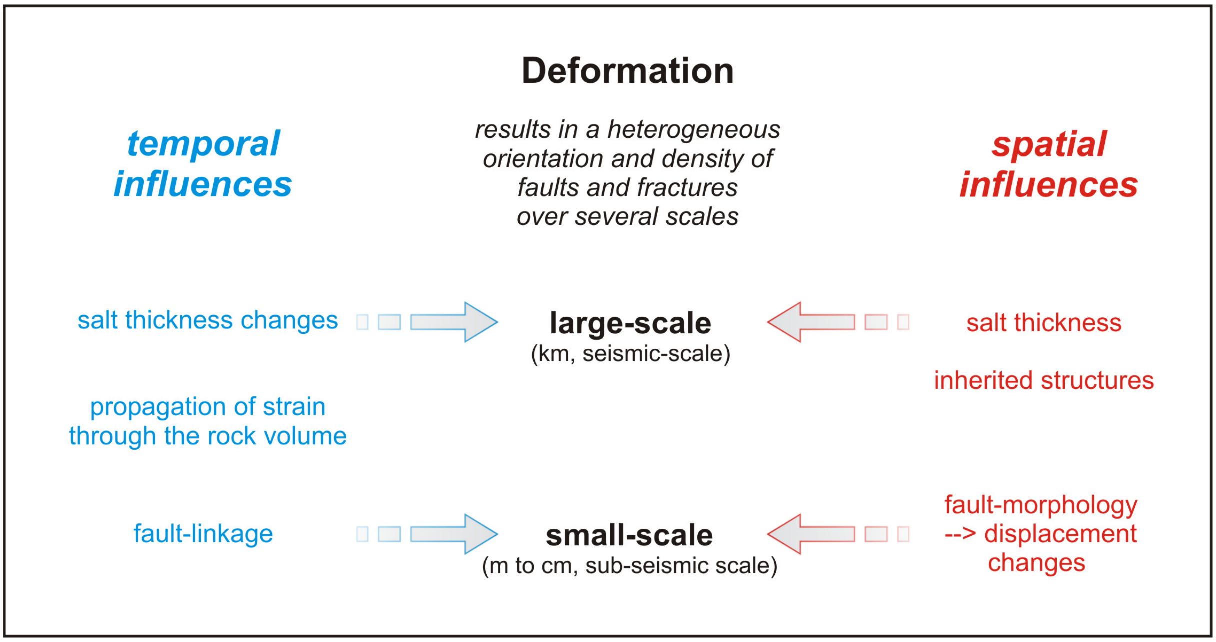

Figure 7.1: Schema illustrating possible tectonic causes for the heterogeneous strain distribution over different scales during one deformation event, as derived from the here presented study within the NW German Basin.

References

Ackermann, R. V. & Schlische, R. W. 1997. Anticlustering of small normal faults around larger faults. *Geology* **25**(12), 1127-1130.

Adam, J., Urai, J. L., Wieneke, B., Oncken, O., Pfeiffer, K., Kukowski, N., Lohrmann, J., Hoth, S., van der Zee, W. & Schmatz, J. 2005. Shear localisation and strain distribution during tectonic faulting - New insights from granular-flow experiments and high-resolution optical image correlation techniques. *Journal of Structural Geology* **27**(2), 299-301.

Arthaud, F. & Matte, P. 1977. Late Paleozoic strike-slip faulting in southern Europe and Northern Africa: results of right lateral shear zone between the Appalachians and the Urals. *Geological Society* **88**, 1305-1320.

Baldschuhn, R., Best, G. & Kockel, F. 1991. Inversion tectonics in the north-west German basin. In: *Generation, accumulation and production of Europe's hydrocarbons. Special Publication of the European Association of Petroleum Geoscientists* (edited by Spencer, A. M.). Oxford University Press, Oxford, 149-159.

Baldschuhn, R., Frisch, U. & Kockel, F. 1985. Inversionsstrukturen in NW-Deutschland und ihre Genese. *Zeitschrift der Deutschen Geologischen Gesellschaft* **136**(1), 129-139.

Baldschuhn, R., Frisch, U. & Kockel, F. 1996. *Geotektonischer Atlas von Nordwest-Deutschland, 1:300.000*. BGR, Hannover.

Barnett, J. A. M., Mortimer, J., Rippon, J. H., Walsh, J. J. & Watterson, J. 1987. Displacement geometry in the volume containing a single normal fault. *AAPG Bulletin* **71**(8), 925-937.

Best, G. 1996. Floßtektonik in Norddeutschland: Erste Ergebnisse reflexionsseismischer Untersuchungen an der Salzstruktur "Oberes Allertal". *Z. dt. geol. Ges.* **147**(4), 455-464.

Best, G., Kockel, F. & Schoeneich, H. 1983. Geological history of the southern Horn Graben. *Geologie en Mijnbouw* **62**(1), 25-33.

Betz, D., Führer, F., Greiner, G. & Plein, E. 1987. Evolution of the Lower Saxony Basin. *Tectonophysics* **137**, 127-170.

Blundell, D., Freemann, R. & Mueller, S. 1992. *A Continent Revealed-The European Geotraverse*. Cambridge University Press, Cambridge.

Bonnet, E., Bour, O., Odling, N. E., Davy, P., Main, I., Cowie, P. & Berkowitz, B. 2001. Scaling of fracture systems in geological media. *Reviews of Geophysics* **39**(3), 347-383.

Brink, H. J. 1986. Salzwirbel im Untergrund Norddeutschlands. *Geowissenschaften in Unserer Zeit* **4**(3), 81-86.

Brink, H. J., Dürschner, H., Trappe,H. 1992. Some aspects of the late and post-Variscan development of the Northwestern German Basin. *Tectonophysics* **207**, 65-95.

Bull, J. M., Barnes, P. M., Lamarche, G., Sanderson, D. J., Cowie, P. A., Taylor, S. K. & Dix, J. K. 2006. High-resolution record of displacement accumulation on an active normal fault; implications for models of slip accumulation during repeated earthquakes. *Journal of Structural Geology* **28**(7), 1146-1166.

Cartwright, J. A., Mansfield, C. & Trudgill, B. D. 1996. The growth of normal faults by segment linkage. In: *Modern developments in structural interpretation, validation and modelling* (edited by Buchanan, P. G. & Nieuwland, D. A.) **99**. Geological Society of London, London, United Kingdom, 163-177.

Cartwright, J. A., Trudgill, B. D. & Mansfield, C. S. 1995. Fault growth by segment linkage; an explanation for scatter in maximum displacement and trace length data from the Canyonlands Grabens of SE Utah. *Journal of Structural Geology* **17**(9), 1319-1326.

Cosgrove, J. W. 2001. Hydraulic fracturing during the formation and deformation of a basin; a factor in the dewatering of low-permeability sediments. *AAPG Bulletin* **85**(4), 737-748.

Crider, J. G. & Peacock, D. C. P. 2004. Initiation of brittle faults in the upper crust: A review of field observations. *Journal of Structural Geology* **26**(4), 691-707.

Dadlez, R., Jozwiak, W. & Mlynarski, S. 1997. Subsidence and inversion in the western part of Polish Basin; data from seismic velocities. *Kwartalnik Geologiczny* **41**(2), 197-208.

Davison, I., Alsop, G. I. & Blundell, D. J. 1996. Salt tectonics; some aspects of deformation mechanics. In: *Salt tectonics* (edited by Alsop, G. I., Blundell, D. J. & Davison, I.) **100**. Geological Society, London, United Kingdom, 1-10.

de Jager, J. 2003. Inverted basins in the Netherlands, similarities and differences. *Geologie en Mijnbouw/Netherlands Journal of Geosciences* **82**(4), 355-366.

Endres, H., Samiee, R., Lohr, T., Krawczyk, C. M., Tanner, D. C., Trappe, H., Thierer, P. O., Oncken, O. & Kukla, P. A. accepted. Quantitative fracture prediction from seismic data. *Petroleum Geoscience*.

Ferrill, D. A., Morris, A. P., Stamatakos, J. A. & Sims, D. W. 2000. Crossing conjugate normal faults. *AAPG Bulletin* **84**(10), 1543-1559.

Frisch, U. & Kockel, F. 2003. Der Bremen-Knoten im Strukturnetz Nordwest-Deutschlands. BGR Hannover, Hannover, 379.

Gast, R. 1991. The perennial Rotliegend Saline Lake in Northern Germany. *Geologisches Jahrbuch* **A119**, 25-59.

Gast, R. E. 1988. Rifting im Rotliegenden Niedersachsens. *Geowissenschaften* **4**, 115-122.

Gauthier, B. D. M. & Lake, S. D. 1993. Probabilistic modeling of faults below the limit of seismic resolution in Pelican Field, North Sea, offshore United Kingdom. *AAPG Bulletin* **77**(5), 761-777.

DOI: 10.2312/GFZ.b103-07087

Gibbs, A. D. 1983. Balanced cross-section construction from seismic sections in areas of extensional tectonics. In: *Balanced cross-sections and their geological significance; a memorial to David Elliott* **5; 2**. Pergamon, Oxford-New York, International, 153-160.

Glennie, K. W. 1998. Lower Permian, Rotliegend. In: *Petroleum geology of the North Sea; basic concepts and recent advances* (edited by Glennie, K. W.). Blackwell Science Geology & Petroleum Geology, Oxford, United Kingdom, 137-173.

Grasemann, B., Martel, S. & Passchier, C. 2005. Reverse and normal drag along a fault. *Journal of Structural Geology* **27**(6), 999-1010.

Groshong, R. H., Jr. 1990. Unique determination of normal fault shape from hanging-wall bed geometry in detached half grabens. *Eclogae Geologicae Helvetiae* **83**, 455-471.

Hancock, P. L. & Barka, A. A. 1987. Kinematic indicators on active normal faults in western Turkey. In: *Shear criteria in rocks* **9**. Pergamon, Oxford-New York, International, 573-584.

Hansen, M. B., Scheck-Wenderoth, M., Hübscher, C., Lykke-Andersen, H., Dehghani, A. & Gajewski, D. 2007. Basin evolution of the northern part of the Northeast German Basin - Insights from a 3D structural model. *Tectonophysics* **437**, 1-16.

Hoffmann, N., Joedicke, H. & Gerling, P. 2001. The distribution of pre-Westphalian source rocks in the North German Basin; evidence from magnetotelluric and geochemical data. *Geologie en Mijnbouw* **80**(1), 71-84.

Hoffmann, N., Joedicke, H. & Horejschi, L. 2005. Regional distribution of the Lower Carboniferous Culm and Carboniferous Limestone Facies in the North German Basin - Derived from magnetotelluric soundings. *Z. dt. Ges. Geowiss* **2**(156), 323-340.

Jackson, M. P. A. & Vendeville, B. C. 1994. Regional extension as a geologic trigger for diapirism. *Geological Society of America Bulletin* **106**(1), 57-73.

Jaritz, W. 1987. The origin and development of salt structures in Northwest Germany. In: *Dynamical geology of salt and related structures* (edited by Lerche, I. & O'Brien, J. J.). Acad Press, Orlando, FL, United States.

Kockel, F. 2002. Rifting processes in NW Germany and the german North Sea sector. *Netherlands Journal of Geosciences/Geologie en Mijnbouw* **81**, 149-158.

Kockel, F. 2003. Inversion structures in Central Europe - Expressions and reasons, an open discussion. *Geologie en Mijnbouw/Netherlands Journal of Geosciences* **82**(4), 367-382.

Kossow, D. 2001. Die kinematische Entwicklung des invertierten, intrakontinentalen Nordostdeutschen Beckens. Unpublished PhD thesis, University of Potsdam.

Kossow, D., Krawcyk, C., McCann, T., Strecker, M. & Negendank, J. F. W. 2000. Style and evolution of salt pillows and related structures in the northern part of the Northeast German Basin. *International Journal of Earth Sciences* **89**(3), 652-664.

Kossow, D. & Krawczyk, C. M. 2002. Structure and quantification of factors controlling the evolution of the inverted NE German Basin. *Marine and Petroleum Geology* **19**(5), 601-618.

Krawczyk, C. M., McCann, T., Cocks, L. R. M., England, R., McBride, J. & Wybraniez, S. 2007. Caledonian Tectonics. In: *The Geology of Central Europe* (edited by McCann, T.) **in press**. Geological Society, London.

Krawczyk, C. M., Eilts, F., Lassen, A. & Thybo, H. 2002. Seismic evidence of Caledonian deformed crust and uppermost mantle structures in the northern part of the Trans-European Suture Zone (TESZ), SW Baltic Sea. *Tectonophysics* **360**(1-4), 215-244.

Krawczyk, C. M., Lohr, T., Tanner, D. C., Endres, H., Samiee, R., Trappe, H., Oncken, O. & Kukla, P. A. 2006. Structural Architecture and Deformation Styles derived from 3-D Reflection Seismic Data in the North German Basin (abs.). *68th EAGE Conference and Exhibition Vienna, Austria, extended abstracts* **P104**, 5.

Krawczyk, C. M., Stiller, M. & DEKORP-BASIN_Research_Group. 1999. Reflection seismic constraints on Paleozoic crustal structure and Moho beneath the NE German Basin. *Tectonophysics* **314**(1-3), 241-253.

Lamarche, J., Bergerat, F., Lewandowski, M., Mansy, J. L., Swidrowska, J. & Wieczorek, J. 2002. Variscan to Alpine heterogeneous palaeo-stress field above a major Palaeozoic suture in the Carpathian Foreland (southeastern Poland). *Paleostresses and tectonics in the peri-Tethyan margins* **357; 1-4**, 55-80.

Lisle, R. J. 1994. Detection of zones of abnormal strains in structures using Gaussian curvature analysis. *AAPG Bulletin* **78**(12), 1811-1819.

Lockhorst, A. 1998. NW-European Gas Atlas. In: *BGR Hannover*, ISBN 90-72869-60-5.

Lohr, T., Krawczyk, C. M., Tanner, D. C., Samiee, R., Endres, H., Oncken, O., Trappe, H. & Kukla, P. A. 2007. Strain partitioning due to salt – insights from interpretation of a 3D seismic data set in the NW German Basin. *Basin Research* doi: 10.1111/j.1365-2117.2007.00329.x.

Manighetti, I., King, G. C. P., Gaudemer, Y., Scholz, C. H. & Doubre, C. 2001. Slip accumulation and lateral propagation of active normal faults in Afar. *Journal of Geophysical Research, B, Solid Earth and Planets* **106**(7), 13,667-13,696.

Mansfield, C. & Cartwright, J. 2001. Fault growth by linkage; observations and implications from analogue models. *Journal of Structural Geology* **23**(5), 745-763.

Manzocchi, T., Walsh, J. J. & Nicol, A. 2006. Displacement accumulation from earthquakes on isolated normal faults. *Journal of Structural Geology* **28**(9), 1685-1693.

Marchal, D., Guiraud, M. & Rives, T. 2003. Geometric and morphologic evolution of normal fault planes and traces from 2D to 4D data. *Journal of Structural Geology* **25**(1), 135-158.

Marrett, R. & Allmendinger, R. W. 1991. Estimates of strain due to brittle faulting; sampling of fault populations. *Journal of Structural Geology* **13**(6), 735-738.

Mauthe, G. 2003. Kompartmentbildende Verwerfungen infolge Kataklase (Rotliegend, NW-Deutschland). *Erdöl Erdgas Kohle* **119**(1), 12-17.

Maystrenko, Y., Bayer, U. & Scheck Wenderoth, M. 2005. The Glueckstadt Graben, a sedimentary record between the North and Baltic Sea in north Central Europe. *Tectonophysics* **397**(1-2 SPEC. ISS.), 113-126.

Mazur, S. & Scheck-Wenderoth, M. 2005. Constraints on the tectonic evolution of the Central European Basin System revealed by seismic reflection profiles from Northern Germany. *Geologie en Mijnbouw* **84**(4), 389-401.

McCann, T. 1998. The Rotliegend of the NE German Basin; background and prospectivity. *Petroleum Geoscience* **4**(1), 17-27.

McCann, T., Pascal, C., Timmerman, M. J., Krzywiec, P., Lopez, G. J., Wetzel, A., Krawczyk, C. M., Rieke, H. & Lamarche, J. 2006. Post-Variscan (end Carboniferous-Early Permian) basin evolution in Western and Central Europe. In: *European lithosphere dynamics* **32;**. Geological Society of London, London, United Kingdom, 355-388.

McLeod, A. E., Dawers, N. H. & Underhill, J. R. 2000. The propagation and linkage of normal faults; insights from the Strathspey-Brent-Statfjord fault array, northern North Sea. In: *Processes and controls in the stratigraphic development of extensional basins* **12**. Blackwell Science, Oxford, United Kingdom, 263-284.

Meissner, R. & Bortfeld, R. K. 1990. *DEKORP-Atlas, Results of Deutsches Kontinentales Reflexionsseismisches Programm.* Springer-Verlag, New York.

Meyer, V., Nicol, A., Childs, C., Walsh, J. J. & Watterson, J. 2002. Progressive localisation of strain during the evolution of a normal fault population. *Journal of Structural Geology* **24**(8), 1215-1231.

Mohr, M., Kukla, P. A., Urai, J. L. & Bresser, G. 2005. Multiphase salt tectonic evolution in NW Germany: seismic interpretation and retro-deformation. *International Journal of Earth Sciences* **94**, 917-940.

Needham, T., Yielding, G. & Freeman, R. 1996. Analysis of fault geometry and displacement patterns. In: *Modern Developments in Structural Interpretation, Validation and Modelling* (edited by Buchanan, P. G. & Nieuwland, D. A.). *Special Publications* **99**. Geological Society, London, 189-199.

Nicol, A., Walsh, J., Berryman, K. & Nodder, S. D. 2005. Growth of a normal fault by the accumulation of slip over millions of years. *Journal of Structural Geology* **27**(2), 327-342.

Nicol, A., Walsh, J., Berryman, K. & Villamor, P. 2006. Interdependence of fault displacement rates and paleoearthquakes in an active rift. *Geology (Boulder)* **34**(10), 865-868.

Nicol, A., Walsh, J. J., Watterson, J. & Gillespie, P. A. 1996. Fault size distributions; are they really power-law? In: *Special issue; Scaling laws for fault and fracture populations; analyses and applications* **18**. Pergamon, Oxford-New York, International, 191-197.

Packard, J. J., Al, A. I., Samson, I., Berger, Z. & Davies, J. 2001. A Devonian hydrothermal chert reservoir; the 225 bcf Parkland Field, British Columbia, Canada. In: *Chert reservoirs of North America* **85; 1**. AAPG Bulletin, Tulsa, OK, United States, 51-84.

Parnell, J., Watt, G. R., Middleton, D., Kelly, J. & Baron, M. 2004. Deformation band control on hydrocarbon migration. *Journal of Sedimentary Research* **74**(4), 552-560.

Peacock, D. C. P. & Sanderson, D. J. 1991. Displacements, segment linkage and relay ramps in normal fault zones. *Journal of Structural Geology* **13**(6), 721-733.

Pharaoh, T. C. 1999. Palaeozoic terranes and their lithospheric boundaries within the Trans-European Suture Zone (TESZ): a review. *Tectonophysics* **314**, 17-41.

Pickering, G., Bull, J. M. & Sanderson, D. J. 1996. Scaling of fault displacements and implications for the estimation of sub-seismic strain. In: *Modern developments in structural interpretation, validation and modelling* **99**. Geological Society of London, London, United Kingdom, 11-26.

Ramberg, H. 1981. *Gravity, deformation and the earths crust.* Academic Press, New York.

Rieke, H., Kossow, D., McCann, T. & Krawczyk, C. 2001. Tectono-sedimentary evolution of the northernmost margin of the NE German Basin between uppermost Carboniferous and Late Permian (Rotliegend). *Geological Journal* **36**(1), 19-38.

Rowan, M. G., Jackson, M. P. A. & Trudgill, B. D. 1999. Salt-related fault families and fault welds in the northern Gulf of Mexico. *AAPG Bulletin* **83**(9), 1454-1484.

Sagy, A., Brodsky, E. E. & Axen, G. J. 2007. Evolution of fault-surface roughness with slip. *Geology (Boulder)* **35**(3), 283-286.

Scheck, M. & Bayer, U. 1999. Evolution of the Northeast German Basin - inferences from a 3-D structural model and subsidence analysis. *Tectonophysics* **313**, 145-169.

Scheck, M., Bayer, U. & Lewerenz, B. 2003. Salt movements in the Northeast German Basin and its relation to major post-Permian tectonic phases; results from 3D structural modelling, backstripping and reflection seismic data. *Tectonophysics* **361**(3-4), 277-299.

Scheck-Wenderoth, M. & Lamarche, J. 2005. Crustal memory and basin evolution in the Central European Basin System - New insights from a 3D structural model. *Tectonophysics* **397**(1-2 SPEC. ISS.), 143-165.

DOI: 10.2312/GFZ.b103-07087

Scholz, C. H. 2002. *The Mechanics of Earthquakes and Faulting*. Cambridge University Press.

Scholz, C. H. & Cowie, P. A. 1990. Determination of the total strain from faulting using slip measurements. *Nature (London)* **346**(6287), 837-839.

Schulze, D. 1994. Entwicklung und Anwendung eines neuartigen Ringschergerätes. *Aufbereitungstechnik* **35**(10), 524-535.

Schwab, G., Benek, R., Jubitz, K. B. & Teschke, H. J. 1982. Intraplattentektonik und Bildungsprozess der Mitteleuropaeischen Senke. *Zeitschrift fuer Geologische Wissenschaften* **10**(3), 397-413.

Sobiesiak, M. 2005. Fault Plane Structure of the 1995 Antofagasta Earthquake Derived from Local Seismological Parameters. Unpublished PhD thesis, Potsdam University.

Spang, J. H. 1972. Numerical Method for Dynamic Analysis of Calcite Twin Lamellae. *Geological Society of America Bulletin* **83**(2), 467-471.

Sperner, B. & Ratschbacher, L. 1994. A Turbo Pascal program package for graphical representation and stress analysis of calcite deformation. *Zeitschrift deutsche geologische Gesellschaft* **145**, 414-423.

Stackebrandt, W. & Franzke, H. J. 1989. Alpidic reactivation of the Variscan consolidated lithosphere; the activity of some fracture zones in Central Europe. *Zeitschrift fuer Geologische Wissenschaften* **17**(7), 699-712.

Stewart, S. A. 2001. Displacement distributions on extensional faults; implications for fault stretch, linkage, and seal. *AAPG Bulletin* **85**(4), 587-599.

Stewart, S. A. & Coward, M. P. 1995. Synthesis of salt tectonics in the southern North Sea, UK. *Marine and Petroleum Geology* **12**(5), 457-475.

Suppe, J. 1983. Geometry and kinematics of fault-bend folding. *American Journal of Science* **283**(7), 684-721.

Tanner, D. C., Krawczyk, C. M., Oncken, O., Baunack, C., Gaupp, R., Littke, R., Schubarth-Engelschall, J., Schwarzer, D., Solms, M. & Trappe, H. submitted. 3D Retro-Deformation of the Rotliegend Strata of the 'Tight Gas' Area, North German Basin. *Tectonophysics*.

Thybo, H. 1997. Geophysical characteristics of the Tornquist fan area Northwest Trans-European suture zone; indication of Late Carboniferous to Early Permian dextral transtension. In: *Trans-European suture zone* **134; 5**. Cambridge University Press, London, United Kingdom, 597-606.

Trappe, H., Endres, H., Thierer, P., Lohr, T., Krawczyk, C. M., Oncken, O., Tanner, D. C. & Kukla, P. A. 2007. Fractal Behavior of Fractures Derived from Seismic and FMI Data (abs.). *69th EAGE Conference and Exhibition London, UK, extended abstracts*.

Trudgill, B. & Cartwright, J. 1994. Relay-ramp forms and normal-fault linkages, Canyonlands National Park, Utah. *Geological Society of America Bulletin* **106**(9), 1143-1157.

Twiss, R. J. & Moores, E. M. 1992. *Structural Geology*. Freeman and Company, New York, USA.

Van Wijhe, D. H. 1987. The structural evolution of the Broad Fourteens Basin. In: *Petroleum geology of north west Europe* (edited by Brooks, J. & Glennie, K. W.). Graham & Trotman, London, United Kingdom.

von Hartmann, H. 2003. Deformation of the Carboniferous on the Oldenburg High and the location of the Variscan Front in Northwest Germany. *Geologie en Mijnbouw* **82**(2), 169-176.

Walsh, J. J., Nicol, A. & Childs, C. 2002. An alternative model for the growth of faults. *Journal of Structural Geology* **24**(11), 1669-1675.

Walsh, J. J. & Watterson, J. 1989. Displacement gradients on fault surfaces. *Journal of Structural Geology* **11**(3), 307-316.

Walsh, J. J., Watterson, J., Bailey, W. R. & Childs, C. 1999. Fault relays, bends and branch-lines. *Journal of Structural Geology* **21**(8-9), 1019-1026.

Walsh, J. J., Watterson, J., Childs, C. & Nicol, A. 1996. Ductile strain effects in the analysis of seismic interpretations of normal fault systems. In: *Modern developments in structural interpretation, validation and modelling* (edited by Buchanan, P. G. & Nieuwland, D. A.) **99**. Geological Society London; Special Publication 27-40.

Walsh, J. J., Watterson, J., Heath, A., Gillespie, P. A. & Childs, C. 1998. Assessment of the effects of sub-seismic faults on bulk permeabilities of reservoir properties. In: *Structural geology in reservoir characterization* **127;**. Geological Society of London, London, United Kingdom, 99-114.

Willemse, E. J. M. 1997. Segmented normal faults; correspondence between three-dimensional mechanical models and field data. *Journal of Geophysical Research, Solid Earth and Planets* **102**(1), 675-692.

Withjack, M. O. & Peterson, E. T. 1993. Prediction of normal-fault geometries; a sensitivity analysis. *AAPG Bulletin* **77**(11), 1860-1873.

Wright, T. D. & Turner, J. P. 2006. Characterization of 3D fault curvature. In: *Geophysical Research Abstracts, 8, EGU*, Vienna.

Yegorova, T. P. & Starostenko, V. I. 1999. Large-scale three-dimensional gravity analysis of the lithosphere below the transition zone from Western Europe to the East European Platform. In: *Geophysical investigations of the Trans-European suture zone* **314; 1-3**. Elsevier, Amsterdam, Netherlands, 83-100.

Yielding, G., Needham, T. & Jones, H. 1996. Sampling of fault populations using sub-surface data: a review. *Journal of Structural Geology* **18**(2-3), 135-146.

Yielding, G., Walsh, J. & Watterson, J. 1992. The prediction of small-scale faulting in reservoirs. *First Break* **10**(12), 449-460.

Ziegler, P. A. 1987. Late Cretaceous and Cenozoic intra-plate compressional deformations in the Alpine foreland-a geodynamic model. *Tectonophysics* **137**, 389-420.

DOI: 10.2312/GFZ.b103-07087

Ziegler, P. A. 1990. Collision related intra-plate compression deformations in Western and Central Europe. *Journal of Geodynamics* **11**(4), 357-388.

Ziegler, P. A., Cloetingh, S., Guiraud, R. & Stampfli, G. M. 2001. Peri-Tethyan platforms; constraints on dynamics of rifting and basin inversion. In: *Peri-Tethys memoir 6; Peri-Tethyan rift/ wrench basins and passive margins* (edited by Ziegler, P. A., Cavazza, W., Robertson, A. F. H. & Crasquin-Soleau, S.) **186;**. Ed du Museum National d'Histoire Naturelle, Paris, France, 9-49.

Ziegler, P. A. & Dezes, P. 2006. Crustal evolution of Western and Central Europe. In: *European lithosphere dynamics* (edited by Gee, D. G. & Stephenson, R. A.) **32;**. Geological Society of London, London, United Kingdom, 43-56.

DOI: 10.2312/GFZ.b103-07087

Acknowledgements

Die hier vorliegende Arbeit wäre nicht möglich gewesen ohne die Unterstützung zahlreicher Personen. Die Wichtigsten möchte ich hier explizit erwähnen:

Zuerst möchte ich meiner Betreuerin **Charlotte Krawczyk** danken. Gründe dafür gibt es zahlreiche: Das hoch interessante Projekt, das viel Potential für spannende Themen lieferte - sei es methodischer oder auch geologischer Fragestellung. Sie ließ mir auch die Freiheit, diesen interessanten Themen nachzugehen und meine Ideen zu verwirklichen. Lotte hatte immer eine offene Tür und ein offenes Ohr für Probleme jeglicher Art. Durch sie lernte ich auch effektiv und selbstständig zu arbeiten, und sie motivierte mich an zahlreichen Tagungen teilzunehmen, Vorträge zu halten und Publikationen zu schreiben, wofür ich ihr sehr dankbar bin!

Mein besonderer Dank gilt **Onno Oncken**. Seine stete Bereitschaft zu Diskussionen, seine konstruktiven Kritiken, sowie sein stetes Lächeln während mancher meiner trüben Schreibphasen, halfen mir sehr beim Verfassen dieser Arbeit :)

Ganz besonders danke ich **Raik Bachmann** für seine kontinuierliche, unermüdliche und selbstlose Unterstützung in jeglicher Hinsicht – sei es fachlich, privat, oder in organisatorischen Dingen (für die ich noch nie die nötige Geduld aufbringen konnte)! DANKE Raik!!!

Ein großes Dankeschön gebührt **Sabine Thiem** vom Schlumberger technical support. Sie besaß große Geduld, jederzeit meine Fragen zu beantworten und Probleme in Bezug auf Geoframe zu lösen, von denen es nun wirklich genug gab… Auch auf die Hilfe von **Wilfried Herr** konnte ich stets bauen, wenn es darum ging, Probleme mit Unix, Linux oder Windows zu lösen.

Dave Tanner danke ich sehr für die Einführung in 3Dmove und GoCad, sowie für Korrekturlesen meines (am Anfang doch recht haarsträubenden) Englisch.

Mein großer Dank gilt auch **Ramin Samiee**. Die konstruktiven und angenehmen Diskussionen über Bohrungsdaten, Kohärenzanalyse, technische Methoden, und auch über nicht-wissenschaftliche Dinge haben mir immer sehr viel Spaß gemacht!

Magdalena Scheck-Wenderoth war immer für Diskussionen bereit, und half mir, den Roten Faden zu finden in dem scheinbar unüberschaubaren Literaturberg über das Zentraleuropäische Beckensystem…

Ich bedanke mich recht herzlich bei **RWE Dea AG** (Hamburg) für die freundliche Bereitstellung des 3D seismischen Datensatzes! Ebenso danke ich **TEEC** für die Kooperation während des gesamten Projektes.

Auch möchte ich mich bei der **DFG** für die dreijährige finanzielle Unterstützung bedanken, die nicht nur mein eigenes Projekt finanzierte, sondern darüber hinaus auch die zahlreichen Treffen innerhalb des SPP 1135 ermöglichte. In diesen Zusammenhang danke ich auch der gesamten **SPP 1135 Gruppe** für die anregenden Diskussionen (zwischen Beamer und Bier) während der zahlreichen Tagungen, Workshops und Exkursionen!

Für interessante Diskussionen bzw. konstruktive Reviews danke ich ebenso **Joe Cartwright, Michael Hudec, Bernhard Grasemann, Richard Groshong, Richard Jones, Reinhard Gaupp, Monika Sobiesiak, Richard Gloaguen, Lothar Ratschbacher, Georg Dresen, Yehuda Ben-Zion, Jürgen Adam** und **Janos Urai.**

DOI: 10.2312/GFZ.b103-07087

Ken McClay danke ich für die Möglichkeit, während meines Auslandsaufenthaltes an der Royal Holloway University of London mit verschiedenen Datensätzen und Softwares in unterschiedlichen Projekten zu arbeiten, was mir letztendlich sehr dabei geholfen hat, meine Dissertation objektiver und kritischer zu betrachten, neue Ideen zu entwickeln und anzuwenden, sowie effektiver und zielstrebiger zu arbeiten.

Für die fachlichen Diskussionen und das Lösen von großen und kleinen Problemen bedanke ich mich besonders bei **Heijn van Gent, Judith Sippel, Jorge Gines, Klaus Bauer, Maike Buddensiek, Silvan Hoth** und **Kerstin Schemmann.**

Die effektive Durchführung der Experimente im Analoglabor wäre nicht möglich gewesen ohne die große Unterstützung von: **Günter Tauscher** und **Frank Neumann** für die individuelle und super funktionierende Konstruktion der Analogbox, **Martin Soijka** und **Achim Reiprich** für die Durchführung der Ringscherexperimente, **Matthias Rosenau** für die Einführung in DaVis und seine ähm…Toleranz was die Staubbelastung im Labor betrifft…. Mein besonderer Dank gilt auch **Thomas Ziegenhagen**, der (trotz der mittäglichen Auseinandersetzungen über Fleischfresser und Kaffeesatztrinker) bei jedem Problem im Analoglabor stets zur Stelle war und sich intensiv bis zur Lösung damit auseinandergesetzt hat!

Außerdem bedanke ich mich ganz besonders bei **Stefan Stief**, der als studentische Hilfskraft schnell, unkompliziert, und mit super Qualität alle anfallenden Arbeiten durchgeführt hat, wie z.B. Kopierarbeiten, Digitalisierung von Abbildungen, Internetrecherche, und vor allem das Einsieben des Sand-Gips-Gemisches… für die eventuell spätere Staublunge entschuldige ich mich schon jetzt ;)

Letztendlich möchte ich mich noch bei **Christoph Heubeck**, **Claudio Rosenberg**, **Sebastian Garcia** und **Doreen Richter** für ihre Bereitschaft, als Mitglieder der Promotionskommission tätig zu sein, bedanken.

DOI: 10.2312/GFZ.b103-07087